Design Refinement and Modeling Methods for Highly-Integrated Hypersonic Vehicles

by

Sean Michael Torrez

A dissertation submitted in partial fulfillment
of the requirements for the degree of
Doctor of Philosophy
(Aerospace Engineering)
in the University of Michigan
2012

Doctoral Committee:

        Professor James F. Driscoll, Co-Chair
        Assistant Professor Matthias Ihme, Co-Chair
        Professor Panos Y. Papalambros
        Associate Professor Joachim R. R. A. Martins

H∞V
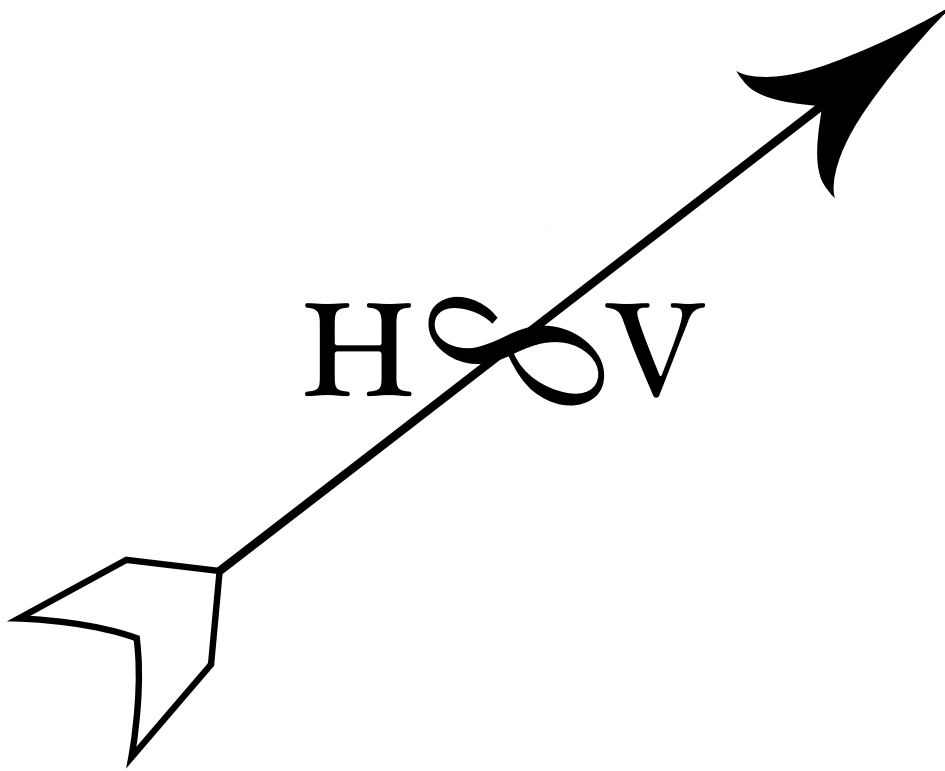
2012

Dedicated to my parents, Michael and Maureen,
for making this dissertation possible
Dedicated to my wife, Anne,
for making it happen

Acknowledgments

The person who has had the most influence on the work presented here is my advisor, Jim Driscoll. I would like to give him a great deal of credit for the good elements of this dissertation. He pointed me in the right direction at every turn and it was very easy to listen to because he respects each student's knowledge and expertise. More importantly, he trusts each of his students with the responsibility for the student's work. This is a dangerous sort of trust and not one that every professor is willing to risk. In my opinion, it creates the best type of collaboration because those wishing to make novel contributions must be given both the tools and the freedom to create new ideas. Jim allows his students this freedom, but he is willing to question them when their ideas may be wrong. He's also willing to accept the same questioning and defend his own ideas. I feel truly blessed to have experienced this type of working relationship, and I have to tell everyone that Jim is an excellent advisor.

Next, I must salute my workmate on the MASIV project, Derek Dalle. Most people know that Derek is a great source of information on all different types of information (be they geography, LaTeX, or aerospace-related), but they may not know that Derek is just about the hardest-working and most dedicated teammate one could ask for. Derek and I ended up working together basically the entirety of the last 4 years, and our team has been (in my humble opinion) extremely productive due to a lot of diligence and willing to learn new techniques together. I hope my partnership with Derek doesn't completely end just because I'm leaving the university.

I must also acknowledge our research sponsors. This research was supported by AFRL grant FA 8650-07-2-3744 for MACCCS (Michigan AFRL Collaborative Center for Control Science), monitored by Dr. David Doman and Dr. Michael Bolender. Support was also provided by NASA grant NNX08AB32A, administered by Donald Soloway, technical monitor. I have spoken to many other students about their research sponsorship, and it's very encouraging for me to be able to say that our research sponsors have been easy to work with. They have guided our research efforts while still letting us determine what was important in their problem of interest, and I think both groups have been able to learn a lot from the partnership. Various meetings

and trips have been a pleasure with the air vehicles group at Wright-Patterson AFB, and with the various NASA centers we have visited.

Matt Fotia and Danny Micka were invaluable to my work because I relied very heavily on their experimental results. Without their diligence and attention to detail, I know for a fact there would have been many more errors in my results. I learned a great deal by working so closely with an experiment in the same research topic as my computational results.

Thanks to the other two people who have been on MACCCS this whole time, Nate Falkiewicz, Torstens Skujins. Scott Frendreis, who now may have the task of integrating a bunch of seemingly disparate pieces of work, was always a great officemate, making humor out of every situation.

Thanks to the rest of the Driscoll group for all of the sharing of ideas that has gone on in various group meetings, celebratory lunches, and other venues. This includes Ethan Eagle, Jacob Temme, Patton Allison, and David Rosenberg. I also blabbed a lot with Nicolas LaMorte and Marco Ceze and Dan Zaide. I don't know how I convinced them all to listen to me go on and on and on, but believe me, you guys shaped my ideas from barely workable to showing some promise, so thanks.

I hope I didn't forget anybody. If I did, I also appreciate you and working with you. This department is good at rewarding collaboration and discussion.

Finally, although they didn't pore over equations with me, my family has been the main support (as families should be) in getting all this work done. Let's start with Anne, my wife, who has really patiently done a lot of listening and a lot of extra work to make sure that I finished everything on time to a level I can be proud of. She really wants me to succeed and showed it over the past several years. My parents, Michael and Maureen, have always been committed to education and creativity, so they deserve thanks for 22 years of commitment to learning, and for all the things they've taught me. I think a lot of those things are exhibited here, in subtle ways. Anne's parents, Tom and Marie, and the rest of her family welcomed me from the beginning, so I have a real extended family here in Michigan, and that's awesome. My brothers and sisters, Patrick, Eileen, Eli, Kathleen, and Rebecca, are ever interested in learning, even when they have to listen through my lectures on aerospace topics. They're all going in different directions, but it's inspiring to see that each one has an extreme level of dedication that I also aspire to. Everyone I mentioned above is very blessed, and a blessing, and for that I thank God.

TABLE OF CONTENTS

LIST OF FIGURES

LIST OF TABLES

LIST OF APPENDICES

LIST OF ACRONYMS

ATC air traffic control. 53

BFGS Broyden-Fletcher-Goldfarb-Shanno scheme. 95

CAC Center for Advanced Computing. 61

CFD computational fluid dynamics. 8, 10, 11, 65, 87

CL centerline. 115

FEM finite element method. 8

HSV hypersonic vehicle. 2, 6, 8, 13, 19, 51, 80, 87

ISS International Space Station. 49

MASIV Michigan/Air Force scramjet in vehicle code. 10, 13–16, 18, 21, 22, 26, 29, 47, 51, 96, 101–103

MASTrim Michigan/Air Force scramjet trim code. 18, 19, 21, 47, 101, 103

MAX-1 MACCCS HSV 1.0. 6, 52, 80, 87, 92, 95, 104

MDO multidisciplinary design optimization. 7

NASA National Aeronautics and Space Administration. 1, 2, 108

NASP national aero-space plane. 2

OTIS Optimal Trajectories by Implicit Simulation program. 10

ROM reduced-order model. 9

SAGE the System for assessing Aviation's Global Emissions. 52, 53

SAMURI supersonic aerodynamic method using Riemann interactions. 47

GLOSSARY

aerothermodynamic pertaining to the interaction between aerodyanmics and thermodynamics. 5

airbreathing a with an engine that uses oxygen from the air as its oxidizer. 2

combustor flameholding region in the flowpath where the fuel is injected; may be constant-area or diverging. 6, 7, 16, 17, 19–22, 24, 34, 35, 38, 41, 45, 52, 64–66, 72, 74–76, 79, 80, 87–89, 92–95, 102–104

control the list of state variables that are able to vary in flight and are also under direct (or nearly direct) control of the operator. 3–9, 11–13, 16, 18, 19, 21, 50–52, 54, 55, 57–61, 82, 91, 101–103, 106, 107

direct-connect windtunnel a directly integrated into the test section of a windtunnel, without an attached. 64

dual-mode a flowpath capable of operating either in the ram mode or the scram mode. 12, 13, 23, 35, 65, 66, 87, 92, 101, 103

flowpath the set of components that comprise the internal flow section through an engine. 2, 5–7, 9, 11, 17, 19–22, 35, 47, 87, 103, 104

hypersonic commonly accepted to mean traveling in excess of Mach 5. 1, 2, 4, 5, 7, 9, 11–13, 17, 35

inlet the forebody and front cowl sections of the that turn the freestream flow through a series of shocks into the internal flowpath. 2, 4, 6–8, 16, 19, 20, 34, 41, 45, 47, 52, 87–89, 92

isolator a section of empty flowpath, usually of constant area, that allows shocks and boundary-layer interactions to form and balance the pressure between inlet and combustor in ram-mode operation. 6, 19, 20, 34, 41, 43–47, 65, 66, 76, 88, 89, 92, 101, 104

low-order model a model that is constructed to have a small number of degrees of freedom. 14

ABSTRACT

Design Refinement and Modeling Methods for Highly-Integrated
Hypersonic Vehicles

by

Sean Michael Torrez

Co-Chairs: James F. Driscoll and Matthias Ihme

A method for early-stage design of high-speed airplanes is presented based on analysis of vehicle performance, including internal flow in the engine and external flows around the body. Several ways of evaluating vehicle performance are shown, including thrust maps, combustor mode stability concerns, combustor optimization and trajectory optimization.

The design performance analysis relies on a routine that computes the thrust of a dual-mode scramjet, which is a geometric-compression (ramjet) engine with a combustor that can operate both subsonically and supersonically. This strategy applies to any internal flow which is predominantly one-dimensional in character. A reduced-order model for mixing and combustion has been developed that is based on non-dimensional scaling of turbulent jets in crossflow and tabulated flamelet chemistry, and is used in conjunction with conventional conservation equations for quasi one-dimensional flow to compute flowpath performance. Thrust is computed by stream-tube momentum analysis. Vehicle lift and drag are computed using a supersonic panel method, developed separately.

Comparisons to computational fluid dynamics solutions and experimental data were conducted to determine the validity of the combustion modeling approach, and results of these simulations are shown. Computations for both ram-mode and scram-mode operation are compared to experimental results, and predictions are made for flight conditions of a hypersonic vehicle built around the given flowpath. Trajectory performance of the vehicle is estimated using a collocation method to find the required control inputs and fuel consumption. The combustor is optimized for minimum fuel consumption over a short scram trajectory, and the scram-mode trajectory is optimized for minimum fuel consumption over a space-access-type trajectory. A vehicle design and associated optimized trajectory are shown, and general design principles for steady and efficient operation of vehicles of this type are discussed.

CHAPTER 1

Introduction

One of the greatest promises made by the aerospace industry in the last 40 years has been that of reusable, repeatable, safe, reliable access to space. This goal has been exceedingly resilient. The flying car is dead. The jetpack is dead. But routine access to space lives on as a dream.

There are many possible ways to address this problem and probably several of them will be ultimately successful. There is nothing at all resembling general agreement on how best to get into space and back safely and cheaply. However, the recent tests of new X-planes (National Aeronautics and Space Administration (NASA)'s X-43 and Boeing/United States Air Force (USAF)'s X-51, specifically) as well as successful commercial space launches (Falcon 9's Dragon, the Virgin Galactic Space Ship Two) suggest that we are on the doorstep of commercial access to space. While all of these vehicles have elements in common, such as the use of rockets as one major element, the ones of interest in this dissertation are the airplanes. The promise of reduced fuel usage, a lifting body and therefore increased payload and fuel capacity, as well as a large fraction of reusable components and runway takeoff and landing make the hypersonic spaceplane a reasonable candidate for the space vehicle of the future. This concept will not exclude rocket propulsion, since all spaceplanes require rockets for the final journey out of the atmosphere, and may well require them for the initial boost to high speeds as well.

This work concerns itself with a few of the technical reasons hypersonic airplanes are still largely experimental. There are budgetary, political, and commercial reasons why hypersonics as a discipline is where it is right now, but there are also a couple of major technical hurdles yet to be solved adequately. I begin my analysis in the following section by pointing out what I believe to be the major remaining problem.

1.1 The Problem

Neglecting all the other possible ways to get to space, the problem is basically that although many of the technologies are already in place that would enable hypersonic vehicles, no such vehicles really exist. This suggests that the difficulties are not within each discipline but interdisciplinary in nature. Heiser and Pratt (the authoritative work on the fundamentals of hypersonic vehicles (HSVs)) [5] note that the history of hypersonic development is a long one, with the first supersonic airbreathing airplanes flying in the 1950s. The varied history of turbo-ramjets (combined cycle engines that begin flying on turbojet power and continue flying with a ramjet engine when they have reached sufficient speed) and rocket-ramjets (combined cycle engines that begin under rocket power) is a long one, and sufficiently well-established to be irrelevant here. Let us concentrate instead on recent efforts to operate scramjets. This short history begins with several paper-study and ground-test and air-experiment (as opposed to aerial vehicle test) efforts, the U. S. national aero-space plane (NASP) [6], a Russian test series [7], and the German Sänger spaceplane [8]. It ends with the X-plane [9, 10] and HiFire tests [11]. There are plenty of test planes and experiments, but none of them is a fully-functioning prototype. The longest flight on record is the X-51 flight of 2009, the duration of which was ~ 200s. This begs the question of what exactly is lacking that prevents us from flying such vehicles successfully for longer durations.

1.1.1 Three case studies

For motivation, let us consider some of the supersonic cruise flight test vehicles, the Lockheed Martin YF-12 [12], the NASA X-43 [9], and the USAF/Boeing X-51 [10]. All of these vehicles were designed for supersonic cruise. The YF-12 was designed to fly at a cruise Mach number of up to 3 and altitude up to 30km and used a turbo-ramjet engine. The X-43 was designed to fly at cruise Mach numbers of either 7 or 10 and altitudes of either 29km or 34km (with two different flowpath designs) and used a scramjet engine only. The X-51 was designed to fly at a cruise Mach numbers from 4.5 to 6 and used a scramjet engine only.

The YF-12 had many successful flights and relied on a translating cowl piece to place shocks in the engine intake in order to avoid unstart, a condition in which shocks move out of the inlet and cause a rapid decrease in the air mass flow rate through the flowpath. Since it relied on conventional turbojet technology augmented by an inlet spike for ram compression, it was able to smoothly transition between

Figure 1.1: Lockheed Martin YF-12A [1]

a full turbojet compression mode to a full ramjet compression mode by translating the inlet spike. Thus, it was usually possible to avoid engine unstart. When unstart did occur (one report said, "Helmets have hit the canopy hard at times" [12]), the situation was rectified by manipulating the spike. This is one of the few high-speed vehicles that has any real control information available in the literature, highlighting the importance of effective engine control systems for ramjet-powered flight.

Figure 1.2: NASA's X-43A [2]

The X-43 had two successful flights and did not have active control of the inlet properties. It had a static inlet whose performance appears to have been optimized for the flight Mach numbers involved. The X-43 was intended to operate steadily during the flights, with fixed Mach number. A control system modulated the fuel pressure and the elevon and rudder settings (and possibly other vehicle control mechanisms, although little is reported in the open literature) [9].
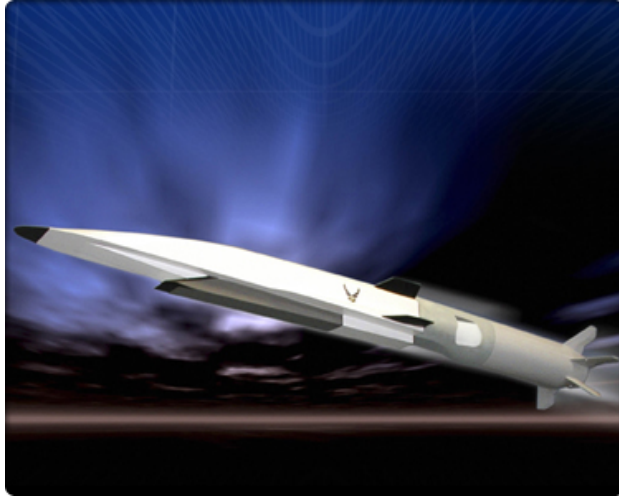
Figure 1.3: Boeing/USAF's X-51 [3]

The X-51 has had one successful flight and one unsuccessful flight to date. The first flight experienced an engine unstart, but the airplane was eventually able to recover. In the second flight the engine experienced an unstart event soon after launch, but the plane was unable to recover. Leaving behind the notable differences between the YF-12, the X-43 and the X-51, there are two basic concerns that at least partially explain the flight failures of the hypersonic vehicles, and they are highlighted by the X-51 failures.

The first thing to note is that the YF-12 was able to transition smoothly between turbojet and ramjet operation. This is important because it means that there was essentially no difference, from the airplane's point of view, between the two modes of operation (and in fact the engine was usually operated somewhere in between the two). The main danger was that of unstart, which was usually avoided and could be reversed if necessary, due to an effective system of engine control. Thus the principal danger in operating the vehicle was nullified by effective control.

The second thing to note is that the X-43 operated at very high Mach numbers. My results based on a similarly-shaped and sized vehicle indicate that flight Mach numbers as high as 7 and 10 leave plenty of margin before the onset of choking (the

usual cause of engine unstart), so the high flight Mach numbers of the tests place the vehicle firmly within the scram-mode-only regime of operation.

Finally, let us note that not only did the X-51 tests begin at lower flight Mach numbers (and hence closer to the choking boundary) than the X-43 test, but the airplane was also intended to accelerate (which implies larger fuel flow rates). These factors contribute to a much higher likelihood of inconvenient mode transition from supersonic combustion (scram mode) to subsonic combustion (ram mode), which then can cause an engine unstart; this is difficult to rectify without a very precise flowpath control system. Although it is impossible to say for certain without more information, it seems likely that the X-51 has a greater risk of failure because it operates closer to the edge of its feasibility envelope. Regardless of the exact cause of unstart, the lack of either sufficient margin before unstart and sufficient control authority during and after unstart resulted in the loss of the 2nd test of the vehicle.

1.1.2 Promising Developments

If no specific physical reason prevents the building of a hypersonic plane that can take off from a runway and land on a runway, then the problem must reside in the combination of components that makes up the plane and results in it being controllable or not sufficiently controllable in the operating region of interest. Either there is some required component that is insufficient for the needs of the airplane or there is a problem at the system level.

The vehicle tests above suggest that the problem with these vehicles is at the system level, and it manifests itself at the boundaries between different flight regimes. So far, probably because of the short duration of the tests and the small sizes of the vehicles, the experimenters have observed that the control problem is principally aerothermodynamic in nature (rather than structural or thermal), and the difficulty is in maintaining the flight regime of the vehicle. This difficulty is encountered even near the design point of the vehicle, so off-design effects that degrade the vehicles performance are significant and highly nonlinear.

Although there are certainly advances to be made in materials and structural design of the airplane before it can be expected to withstand the thermal loads imposed by flight Mach numbers between 4 and 12 (commonly believed to be a reasonable range of conditions for a hypersonic airbreather), the tests that have been completed so far indicate that short-duration tests, at least, would be possible if the systems-level control issues could be solved adequately. Thus, the biggest bottleneck at present is

the process of design including control analysis from an early stage using predictive analysis. The following section provides some background on previous attempts that have been made to optimize airplanes taking into account trajectory and control.

1.1.3 Vehicle description

As can be seen in Fig. 1.4, the general type of HSV considered here has a relatively simple shape that integrates the engine flowpath into the body of the vehicle. The vehicle shown in Fig. 1.4 is the vehicle referred to as MACCCS HSV 1.0 (MAX-1). It is depicted flying from right to left, so that the control surfaces are to the rear of the vehicle. Sections of the vehicle that are part of the flowpath are marked in red, such that the flowpath is embedded in the vehicle and takes up a significant portion of its width. The components of the flowpath are discussed in greater detail in section 2.1.1.

The external portion of the inlet can be seen on the bottom of Fig. 1.4; the internal portion is obscured by the cowl, which is visible on the very bottom of the vehicle and covers about the middle 20%. Beginning inside the tail end of the cowl, and extending behind it to the very rear of the vehicle are the internal and external nozzle sections. The isolator and combustor cannot be seen on the external view of the vehicle and are inside of the cowl. Cross sections of the flowpath will be shown in later sections.

There are four control surfaces visible in Fig. 1.4. These are two rudders that stand up vertically, and two elevons that stand out to the sides. This vehicle has no wings, because it is a "lifting body" concept; the inlet and the nozzle, which create significant vertical forces, along with the elevons, provide all the lift. Thrust of the flowpath is computed based on the streamtube shown in red triangles, and drag is computed using the rest of the external geometry, shown in white triangles. The different vehicle concepts discussed in section 1.2 all have slightly different configurations, but these component descriptions serve as a general orientation for the reader.

Station numbering for this class of vehicle is shown in Fig. 1.5. Going from left to right, ∞ refers to the free stream condition, $1a$, $1b$, etc. refer to the conditions after each panel in the inlet, $2a$, $2b$, etc. refer to the conditions after each panel inside the cowl, $3a$, $3b$, etc. refer to the conditions after the isolator, $4a$, $4b$, etc. refer to conditions after geometry changes in the combustor (injectors, diverging panels, etc.), and $5a$, $5b$, etc. refer to conditions after geometry changes in the internal and external parts of the nozzle. This station numbering is used because it is extensible if more injectors or panels are added, and it is consistent with the station numbering

typically used for other types of flowpath analysis.

1.2 Previous work

There have been numerous studies on the design of aircraft components using optimization. Rather than referring to this extensive literature, I discuss here a few studies that attempted full-vehicle design and trajectory/control simulation, in a few cases simultaneously. Since the majority of airplane optimization studies focus on airplane configurations that are basically well-understood, they analyze only modest departures from the existing designs on which they are based. for this reason, they successfully rely on tabular data, either from measured performance or from reduced-order models based on limited numbers of high-fidelity simulations done in the regime of validation for those vehicles. In contrast to that approach, a number of papers on design, control, and trajectory simulation of subsonic and hypersonic airplanes rely on what some have termed "fundamental models." These are usually algebraic in nature and provide performance information that is similarly easy to deal with in optimization to the tabular approach, since it is usually continuous and continuously differentiable.

Bowcutt [13] focused on multidisciplinary design optimization (MDO) for single-point performance optimization. This did include the effects of propulsion, aerodynamics, and trim, and in that respect represents a significant step forward–the notion that each of these considerations can, and should, be included even in very early-stage design investigations. This analysis used algebraic equations to compute vehicle performance, and elementary aerodynamics to compute lift and drag (assume drag and lift coefficients and dynamic pressure).

O'Neill and Lewis [14] also performed multidisciplinary design optimization (MDO) including the effects of propulsion and aerodynamics. They advanced the engine performance model by incorporating ignition delay and reaction time constants, using experimental results. This type of engine performance model is only valid for that combustor temperature and pressure condition, so all optimized configurations are constrained to deliver that condition. This in turn means that the actual flight condition of the vehicle varies as its design changes, so that the final combustor condition can be achieved with each geometry. Although not explicitly stated, they also seem to have used elementary analysis to design the waverider shape and elementary shock analysis to determine the effect of inlet ramps and cowl in deflecting the flow. Engine performance was determined using the method of Shapiro [15] with simplified

reaction information. The nozzle performance was determined using the method of characteristics.

Because the trim $(F = D, L = W)$ constraint is applied, the O'Neill and Lewis optimizer also has authority over the trim of the vehicle. However, since overall moment was not considered in their work and since there are no external control surfaces, their approach is necessarily limited to cases in which static trim is possible under the angle of attack and other flight parameters assumed in the analysis routines. Each design in this study is valid for a single, given operating point, and range is maximized at that operating condition using $L/D \cdot I_{sp}$ as a surrogate for total range. The decision variables in this case were the geometric parameters that determined the waverider geometry. These were various spline points that govern the wing shape and the engine inlet aperture, the position of the engine inlet aperture (cowl lip location), position of the end of the cowl in the nozzle section (cowl trailing edge location), and the loading edge radius of the cowl (which has an impact on the bow shock deflection). Their optimization problem is

$$\text{minimize} \quad (L/W)^a (F/D)^b (D/L \cdot I_{sp}) \tag{1.1}$$

$$\text{w.r.t.} \quad \begin{bmatrix} 10 \text{ spline parameters} & \text{cowl lip location} \\ \text{engine width} & \text{bow shock angle} \\ \text{cowl trailing edgelocation} & \text{cowl leading edge radius} \end{bmatrix}$$

$$\text{subject to} \quad \text{geometric constraints}$$

$$(L/W)^a \geq 1$$

$$(F/D)^b \geq 1 \tag{1.2}$$

which indicates that the trim condition is applied through a penalty method. O'Neill and Lewis found this approach to be successful in generating plausible waverider-type HSVs, both for acceleration and cruise.

The more recent and more detailed optimizations have typically resorted to tabulated results from computational fluid dynamics (CFD), finite element method (FEM), and engine performance analysis codes, as well as tabulated measurements from actual vehicles. This approach has many merits, not the least of which is that it provides accurate and precise information about performance of the vehicle while providing a structure that is easy to optimize with gradient-based optimizers. The drawback is that the number of variables used to design the airplanes and trajectories has typically been confined to be very small, since generation of appropriate surrogate models with large numbers of variables becomes very expensive due to the run times required

for the underlying fluid, structural, and propulsive models. Relatively few full-vehicle airplane design studies that use optimization are represented in the literature, so a detailed summary of a few notable ones follows.

Probably the most detailed preliminary design study of a hypersonic vehicle to use optimization was another study by Bowcutt [16]. In this more sophisticated investigation, the principle addition was trajectory analysis to compute an objective function (in this case range) that applies to the entire mission, rather than a single operating point. The vehicle considered in this paper was a Mach 6 to 7 cruise missile that begins flight at $M = 4.5$ and accelerates to the cruise condition. The optimization focused entirely on the exterior of the vehicle, including some aspects of configuration design, such as placement of the engine and size of ballast. However, the engine flowpath had been designed separately and was therefore excluded from the design study, except for its placement and angle with respect to the vehicle.

Bowcutt notes in this paper that the disciplines considered are aerodynamics, propulsion, stability, control, and mass. The objective was to maximize range, under constraints defined for each geometric variable based on physical concerns, and the constraint that the vehicle be trimmed in a $F = D$, $L = W$ sense throughout the trajectory. Five decision variables were considered: nose angle (on the top of the vehicle), engine axial location, engine cant (angle of the engine centerline with the body of the vehicle), cowl length (at the back of the engine), and chine length. The vehicle was parametrized based on these vehicles and was faceted for ease of computation. Various design rules translate the values of the 5 decision variables into a 3-D vehicle. Several low-order models were used to compute aerodynamic performance. A 2-D Navier-Stokes solver used in the inlet, a 1-D cycle analysis code used in the engine flowpath, and a method-of-characteristics solver used in the nozzle, and the resulting performance calculations were implemented as a response-surface reduced-order model (ROM).

Stability is included via an inner-loop optimization that attempts to converge to a "stable enough" solution by manipulating the ballast and tail sizes at 4 discrete points in the trajectory that are assumed to describe the most stringent requirements on the control system. Vehicle mass computation is provided using engineering analysis. Trajectory analysis was through a "direct transcription" method, in which the vehicle is trimmed to a specified condition at each point in the trajectory, and a single trajectory was prescribed in advance. This approach leads to the following

optimization problem

$$\text{minimize} \quad -\text{range} \tag{1.3}$$

$$\text{w.r.t.} \quad \begin{bmatrix} \text{nose angle} & \text{engine location} \\ \text{engine cant angle} & \text{cowl length} \\ \text{chine length} & \end{bmatrix}$$

$$\text{subject to} \quad \text{geometric constraints}$$

$$\text{given trajectory}$$

$$\text{4 stability constraints} \tag{1.4}$$

The optimization was performed using the nonlinear simplex method of Nelder and Mead[17]. It is not specified how points were added to the baseline cruise trajectory in order to change the range of the vehicle. Although their paper indicates that trajectory optimization was used after the vehicle geometry was optimized for the baseline trajectory, no details were provided about the manner in which the trajectory was improved. Their paper does indicate that trajectory optimization was performed on the optimized vehicle using Optimal Trajectories by Implicit Simulation program (OTIS) [18]. Bowcutt deemed the method successful for range extension of a family of vehicles.

Another highly detailed design example that optimized both vehicle parameters and trajectories is that of Koko [19]. This design example used both fundamental performance models based on algebraic equations and CFD results that had been reduced into performance tables. This gave vehicle engineering performance metrics at different points in the flight regime, which were integrated into a semi-empirical performance estimation routine similar to that of [20]. Koko did include aerostructural interactions in a co-optimization. Thrust performance, however, was included only using a linear model, which essentially makes the assumption that the engines can always deliver the desired thrust. Control performance is included in the sense that the vehicle is assumed to be trimmed based on the linear equations using the engineering performance metrics. This corresponds to a direct transcription trajectory simulation. There is much of value in this approach, and the work presented in this dissertation expands on [19] and [20] by using a collocation method for trajectory simulation and by including the full vehicle dynamics as predicted by Michigan/Air Force scramjet in vehicle code (MASIV), including engine performance.

1.3 Present work

Hypersonic airplanes are one of a class of vehicles that can be described as highly coupled. This means that it is difficult or impossible to separate the design of the different component of the vehicle from the systems-level design of the vehicle as a whole [21]. It is also difficult to design the vehicle in such a way as to give reasonable operability margins without pre-knowledge of the trajectory it will be assigned to follow. Conversely, the trajectory is not easy to specify unless it is known what maneuvers the vehicle is able to perform at each point in the flight regime, which is a function of the vehicle design. Therefore, my efforts have principally been focused on understanding the limitations on operability, thrust, and moment of engine flowpaths.

This coupled structure demands a model suitable for simultaneous design of each of these four major components: mission, vehicle, trajectory, and control. Although the glossary contains definitions of all discipline-specific terms, some terms are defined here to make the vehicle configuration clear.

This dissertation presents a modeling scheme for hypersonic vehicles operating in supersonic- and subsonic-combustion modes that is useful for control design and evaluation and vehicle design and optimization (Chapter 2). It also presents a trajectory optimization method for ensuring their adequate performance over plausible trajectories that is useful when initial configurations and trajectories are either unknown or not well understood (Chapter 3). This is useful when new designs are considered, since it is sometimes the case that the operational envelope and vehicle parameters are not predetermined (such as for test vehicles). Analysis of the accuracy of the vehicle performance model is presented in Chapter 4, showing agreement not significantly worse that presently available commercial CFD. Predictions made using the model and the trajectory optimization scheme are shown as the primary results of this research in Chapter 5. Finally, some general conclusions about hypersonic flowpath design for stability, optimization of vehicles including trajectory, and usage of non-surrogate-based optimization are offered in Chapter 6.

Although the motivation for development of the models and control strategy was to use the computer codes for control design and evaluation and early-phase design studies of vehicles, the dissertation begins by showing how the vehicle performance models were developed, because this directs the use of the model in control and trajectory studies.
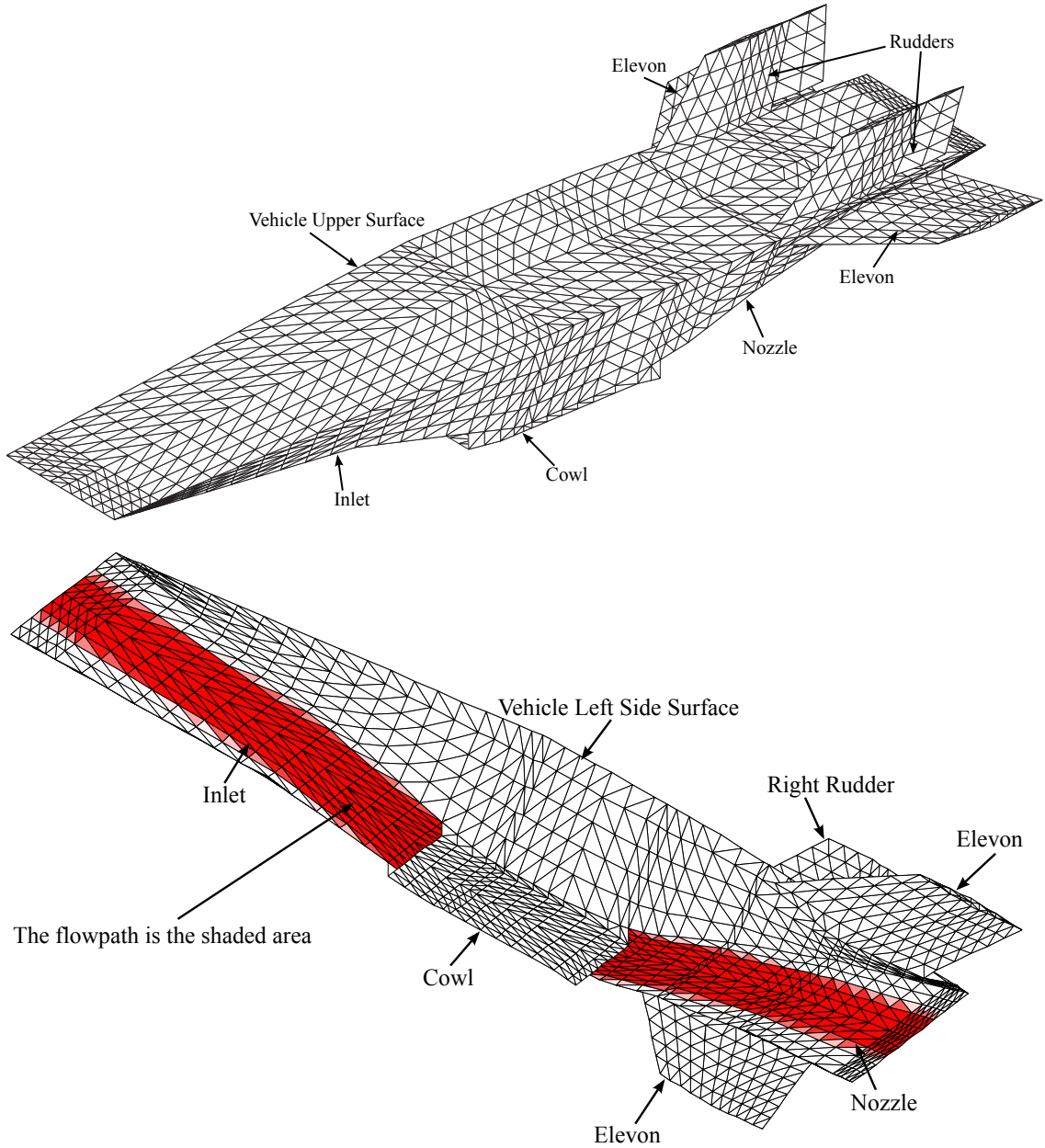
Figure 1.4: The MAX-1 vehicle.

1.3.1   Contributions

This thesis makes the following major contributions.

1. An aerothermodynamic model of a hypersonic airplane from tip to tail with enough fidelity to make control design possible, and with fast enough run times to facilitate the use of optimization methods.

2. Supersonic combustion simulations of a dual-mode ramjet/scramjet.
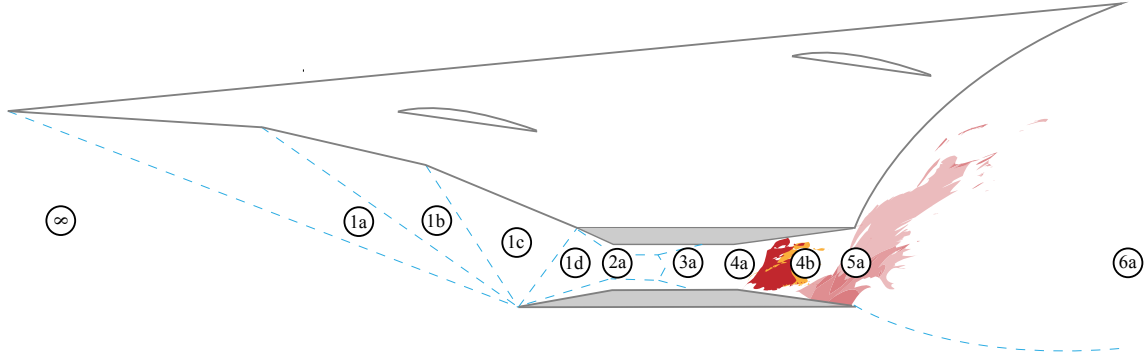
Figure 1.5: Flowpath station numbering in MASIV.

3. Subsonic combustion simulations of a dual-mode ramjet/scramjet with favorable comparison to experiment.

4. Simulation of trajectories and optimal control schemes over a wide range of conditions using the model and contemporary trajectory optimization techniques.

5. Several design principles that allow vehicles to be designed to operate over a range of conditions, rather than designed for a single operating point.

6. A vehicle design and associated trajectory and control requirements to complete a reasonable scramjet trajectory of interest for space access.

1.3.2 Modeling

A large portion of the effort on this thesis has been the development of a HSV analysis code suitable for vehicle design over the range of conditions of interest. This essentially required a method that could handle both ram-mode (subsonic combustion in the engine) operation and scram-mode (supersonic combustion in the engine) operation, as well as a range of flight conditions from a Mach number and altitude of about $M = 4.5$, $h = 18$km to about $M = 12$, $h = 30$km. As presented in [22] and [23], this objective has been achieved with the present version of the MASIV code developed by Derek Dalle and me. To my knowledge there is not another code that can compute hypersonic airplane performance from tip to tail considering both external and internal flows. Even though our model is simple in many ways, it predicts many of the observed properties of hypersonic vehicles. This has already allowed us to propose plausible explanations for some seemingly mysterious dynamics, such as thermal choking, jet wake flame stability limits, and unstart.

The guiding principle for developing MASIV has been to retain enough physics to be able to credibly predict engineering metrics like thrust and lift and operational phenomena like mode transition and unstart. We chose early on to use low-order models rather than a reduced-order model (ROM) such as proper orthogonal decomposition. Low-order models are used instead of high-fidelity ones only because of the constraint that the run time be on the order of seconds.

The objective of the modeling effort is of course to produce simulations that accurately reproduce the physical behaviors of the vehicle in flight. However, it is easily observed that few full-vehicle simulations at high fidelity have been attempted, to say nothing about the substantial debates that arise regarding their accuracy. In light of these difficulties, a high-fidelity approach is not necessarily to be preferred. The great expense of obtaining solutions that may ultimately be no more accurate than simpler methods prohibits this.

Any desired computational time is naturally arbitrary—a function of the time and computer power available. A general guideline given to us by research sponsors (and present main users of the code) is that solutions of single runs should require approximately 1 second, and that trajectory and control simulations should take no more than 24 hours. These are human-motivated numbers based on the amount of time designers are willing to wait before getting evaluations back.

There is not much room to parallelize analysis routines requiring seconds to run because overhead such as file transfer and memory use dominates parallel processing in those cases. Therefore, we assume that the base analysis (MASIV) will always run on single processors and this means runtime is the prime cost motivator.

The analysis routine is useless if it does not properly predict behaviors of the vehicle that are relevant for the control and trajectory simulation. Conversely, behaviors of the vehicle that have no bearing on control or trajectory performance can safely be ignored. Although it is difficult to determine which physical phenomena are "relevant" without the insight of numerous real-world design tests, the few successful and unsuccessful tests so far give some important cues.

First, variable performance as a function of al the control inputs is required, or control analysis cannot even begin. Second, the significant nonlinearities involved in the inlet due to shock and expansion wave interactions must be included. Third, the performance deficit due to incomplete combustion is observed in nearly every scramjet combustor experiment and must be included. Fourth, the effects of unstart, mode transition and flameout, which are evidently problematic enough to cause crashes, are paramount but dependent on the previous three requirements.

Thus, two competing desirable properties emerge. Most importantly, the 4 required behaviors must be predicted by the analysis code, no matter how much simulation time this implies. Once these things are included, the simulation time should be kept to 1 second or less for single runs and 24 hours or less for trajectory simulations. If both of these conditions are met, the fidelity should be increased until the time ceiling is reached. As will be discussed later, the time requirements dominate. Typically one call to MASIV requires 3 to 30 seconds on a 3.6 GHz processor, depending on the run conditions. Trajectory simulations require 24 to 72 hours with MATLAB. Compiled implementations may require 10 to 20× less computation time.

CHAPTER 2

Control-Oriented Models

This portion of the work addresses the need for an improved control-oriented model of a dual-mode ramjet-scramjet propulsion system. Improvements to existing models are needed to include more realistic estimates of the losses of the propulsion efficiency due to shock wave interactions in the inlet, as well as due to gas dissociation and incomplete combustion in the combustor section. One problem is that previous lower order propulsion models [24, 25, 26] do not include the losses due to multiple shock interactions, gas dissociation, and due to incomplete combustion caused by finite-rate chemistry. This is a serious problem because the main advantage of a scramjet engine over a ramjet is that the scramjet reduces losses due to internal shock waves and gas dissociation [5]. That is, the scramjet eliminates the need for strong internal shock waves to decelerate the gas to subsonic conditions and maintains lower static temperatures than a ramjet which reduces the dissociation losses. The present effort addresses previous shortcomings by including both of these types of losses into a code called MASIV. MASIV consists of several low-order models. One is an inlet and nozzle model that computes losses due to multiple shock/expansion wave interactions; this ROM is described elsewhere [27]. The other comprises a fuel-air mixing/combustion model that is the focus of section 2.2 and a operating mode model that is the focus of section 2.4.

Since CFD codes take many hours to reach solutions for reacting flows, they are difficult to apply to problems in which a large number of solutions are required. A tool that can solve these configurations in a short time to acceptable accuracy is highly desirable for control and design applications, such as control evaluation, and multidisciplinary design optimization (MDO). The proposed one-dimensional method [28, 29, 30, 31, 32] solves for the heat release distribution for both subsonic and supersonic internal flows.

Many control evaluation codes and some MDO routines use ROMs in some capacity in order to provide solutions in a reasonable amount of time. ROMs are

typically based on approaches employing dimensional reductions in which detailed or high-fidelity simulations are approximated through a set of basis functions or lookup tables [33]. ROMs usually do not compete with CFD, elementary combusion, finite element, or other high-fidelity simulations but instead use these tabulated high-fidelity solutions at runtime. While these types of ROMs provide a rapid way to generate solutions, they are confined to the fixed geometry and the limited range of validity for which the tabulated results were generated. The accuracy and range of validity of each ROM must be carefully quantified by making comparisons to high-fidelity CFD or experimental findings.

The present work treats the problem differently from the POD approach; it reduces the dimensionality of the physics retained in the problem so that the entire code can be run in a short time. This makes it possible to solve the entire flow field, rather than fully relying on pre-tabulated solutions, and it means that run conditions are not constrained to be between the bounds of pre-tabulated cases for the physics of the simulation to be accurate since the conservation laws are solved directly—they are not reduced into an interpolation or a regression scheme.

General 1-D flow solution for hypersonic flowpaths has been covered in the literature. O'Brien et.al. [34] use the basic conservation equations in one dimension, adding finite-rate chemistry, and Torrez et.al. [22] implement a jet-in-cross-flow turbulence and diffusion flame model (this paper forms the basis of section 2.2). However, since these results are obtained by solving a set of ordinary differential equations (ODEs) they do not admit wave-type solutions. This difficulty becomes important if we wish to consider subsonic combustion cases, since the stability of the flow relies on the propagation of information upstream from the choking location in the combustor up to end of the supersonic inflow portion of the duct. This physical process leads to the creation of a pre-combustion shock train (PCST), which in turn allows the dual-mode flowpath to operate both sub- and supersonically. Section 2.4 is a discussion of how steady, 1-D flows can be solved in a way that allows for choking conditions to be considered.

2.1 Model architecture

The overall objective of the vehicle model is to compute the parameters of interest for a performance-modeling code to sufficient accuracy to perform trim and trajectory studies, while keeping overall run times for such studies to within a few days on available computer systems. This means that all the components are represented

using low-order models, rather than typical disciplinary analyses such as CFD or FEM, which may take hours or days to complete. As described in section , this approach is favorable for purposes of initial vehicle and trajectory studies because it is not apparent what form the vehicle and trajectory will take before the design study begins, which means that creating a viable surrogate for an appropriate number of variables can be expensive.
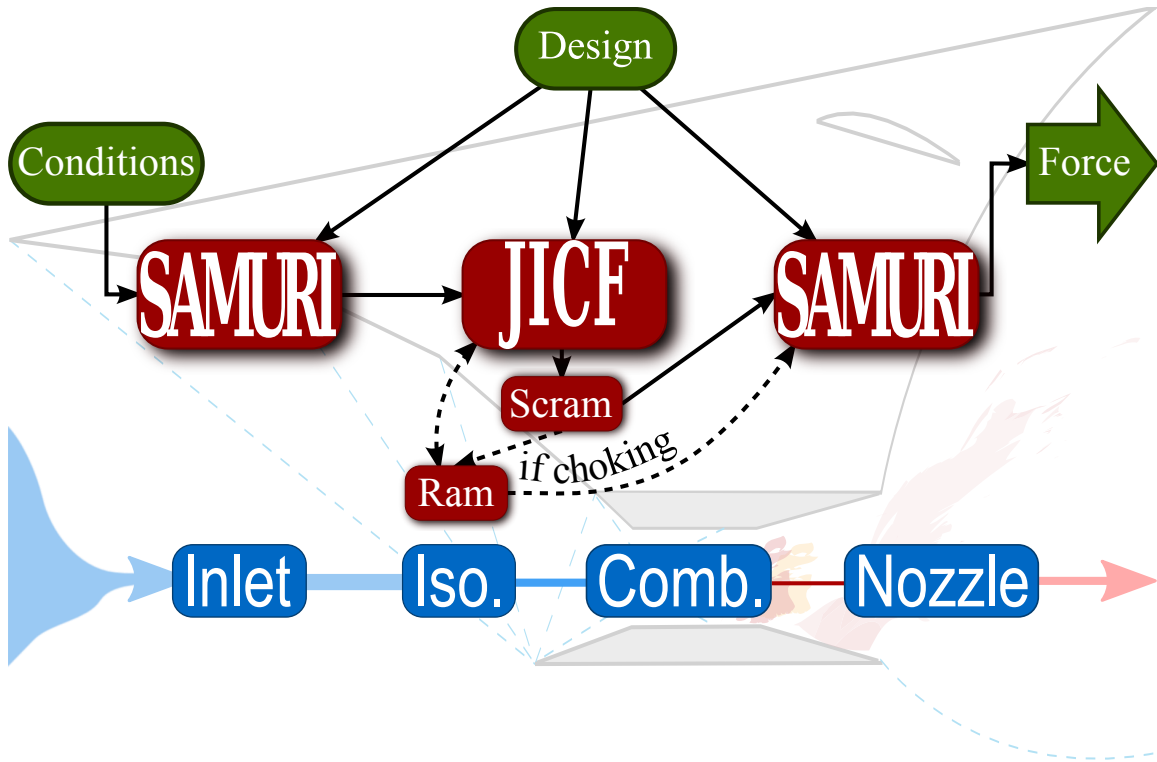
Figure 2.1: Information flow between the different analyses within MASIV.

The vehicle model consists of two main components, which are an external fluid dynamics solver and an internal fluid dynamics solver. The external fluid dynamics solver and trim routine is called Michigan/Air Force scramjet trim code (MASTrim), and will be given cursory treatment here (with references to publications that explain how it works in greater detail). The internal fluid dynamics solver is called MASIV, and is fully explained here, with references to the initial publications in which the methods were developed.

The MASIV package takes an operating point consisting of flight Mach number, altitude, and angle of attack,

$$\begin{bmatrix} M_\infty & h & \alpha \end{bmatrix}^T \tag{2.1}$$

and a control state that is simply the equivalence ratio, δ_{ER}.

The MASTrim package takes an operating point consisting of the latitude, longitude, altitude, flight Mach number, flight path angle, heading angle, angle of attack, sideslip angle, and roll angle. These variables uniquely define the position and velocity state of the vehicle.

$$\begin{bmatrix} L & \lambda & h & M & \gamma & \sigma & \alpha & \beta & \phi \end{bmatrix}^T \tag{2.2}$$

consisting of equivalence ratio, collective elevator, differential elevator, collective rudder, and differential rudder,

$$\begin{bmatrix} \delta_{ER} & \delta_{CE} & \delta_{DE} & \delta_{CR} & \delta_{DR} \end{bmatrix}^T \tag{2.3}$$

and returns net forces and moment in two dimensions, as well as the location of the moment axis,

$$\begin{bmatrix} F & M & r_M \end{bmatrix}^T \tag{2.4}$$

Mach number and altitude are defined in the usual ways. Angle of attack must be defined relative to some baseline, and here the vehicle baseline is along the centerline of the isolator and combustor section. Equivalence ratio is the mass of fuel injected relative to the stoichiometric fuel mass [35]. Common elevator is the average angular deflection of the elevators; differential elevator is the deflection angle of the right elevator minus the deflection angle of the left elevator [36]. Positive elevator deflections move the trailing edges down. The common rudder and differential rudder control variables are similarly defined, although not used for the trajectories shown here.

2.1.1 Flowpath components

MASIV itself consists of 4 component analysis sections. Although this division into components is somewhat arbitrary, it is an established practice in HSV analysis [5], and leads to appropriate simplifications in the modeling equations. The 4 components of the HSV flowpath are inlet, isolator, combustor, and nozzle. Figure 2.2 shows the baseline flowpath configuration. The internal portions are shown in a zoomed-in view in Fig. 2.3.

The performance of the inlet and nozzle is computed using a 2-D, gridless, Riemann interaction solver [27, 37]. This solver requires supersonic initial conditions because it relies on the hyperbolic nature of the supersonic flow equations in order to geometrically trace flow regions.

The supersonic inlet condition is provided by the gas properties at altitude given
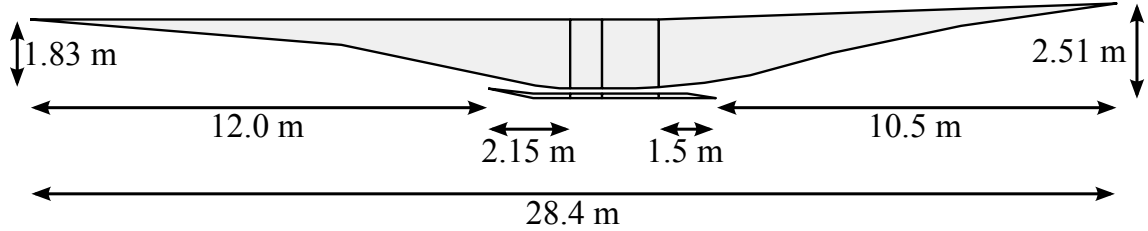
Figure 2.2: Generic flowpath for the baseline vehicle. From left to right are inlet, isolator, combustor, and nozzle [4].
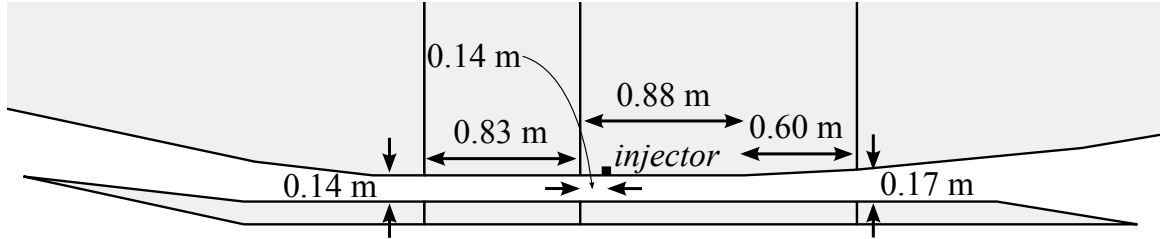
Figure 2.3: Generic flowpath for the baseline vehicle, close view. From left to right are (internal) inlet, isolator, combustor, and (internal) nozzle [4].

in the U.S. standard atmosphere [38] and the flight Mach number. This condition, the inlet geometry and the angle of attack are enough information to compute inlet performance and determine a homogeneous condition at ②ₐ. In the isolator and combustor components, the flow is assumed to be 1-D, although some quantities are computed using multidimensional sub-steps.

As shown in Fig. 2.1, the isolator condition may or may not depend on the downstream condition. As will be discussed in section 2.4, there may be a pre-combustion shock train (PCST) in the isolator that matches the condition at the front of the isolator to the condition in the combustor known as the thermal throat. A thermal throat is required, along with a PCST, when the operating point and fueling condition cause the Mach number in the combustor to drop below unity. In this case, the flowpath is said to operate in ram mode. If the flow is supersonic throughout the combustor, but a PCST is still required in the isolator to ensure a matched condition, the operating mode is termed "early scram." Early scram mode is discussed in section 2.5. If the flow is supersonic throughout the combustor and there is no matching requirement, the mode is termed "pure scram." Pure scram is the simplest case and is discussed in section 2.3.

Because of the possible need for a PCST in the isolator, the isolator and combustor must, in general, be solved simultaneously. In either case, the same solution method is used to compute the evolution of state quantities through the combustor, as described

in section 2.3. Thus, the basic flow solver that constitutes the building block of the isolator/combustor code is the same one that is used in pure scram mode.

Finally, the performance of the nozzle is computed using the condition at the end of the combustor. The overall thrust and moment of the whole flowpath is computed by elementary stream-tube momentum analysis, with a control volume fitted to the contours of the vehicle.

The external aerodynamics are computed by a shock/expansion method with boundary layer corrections [36, 39]. The vehicle geometry consists of panels, which allows easy computation of the deflection angle of each panel compared to the free stream. Control surfaces (rudders and elevons) are considered to be part of the vehicle geometry, so the forces created by these surfaces are accounted by the overall panel method. This model does not account for shock/boundary layer interactions.

The overall performance of the vehicle is computed establishing a width for the 2-D internal flowpath of MASIV, which gives propulsion information. Then, the external aerodynamics routine provides additional force components along the three body dimensions, as well as moments along the three body axes. The forces on outside of the vehicle and the inside of the vehicle are summed to give resultant six-degree-of-freedom forces and moments. This is the principal input to the trim and trajectory components of MASTrim, described in section 2.7.

2.1.2 Control-oriented modeling approach

In order to ensure that computation times remain short, it was considered advantageous to use ordinary differential equations (ODEs) rather than partial differential equations (PDEs) in time and space. Although this means that MASIV is not applicable to unsteady flows, it does allow simulations to be done in a matter of seconds on a $2 - 3.6\,$GHz processor. This type of low-order model is limited to quasi-one-dimensional applications and steady conditions. The fuel must be injected as a jet in cross flow and reaction rates must be computed in advance. Since the model only predicts steady-state operation, the transient process connecting ram-mode and scram-mode operation is not predicted.

The combustor code solves a set of differential and algebraic equations in space [34], marching axially through the combustion duct. Since combustion in most engines is mixing-limited rather than reaction rate-limited, 3-D jet mixing must be computed. However, since we only allow differential equations containing derivatives with respect to the axial distance coordinate, we use an algebraic jet spreading scaling relation [40].

This amounts to using a ROM for jet spreading characteristics, but the solution is based on flow field similarity rather than a lookup table, so it is valid for a wide range of flow conditions that have jet-wake-stabilized flames.

The combustion model considers finite-rate chemistry within the Steady Laminar Flamelet Model (SLFM) [41], which considers each point in the flame and maps to it the solution of a corresponding counter-flow flame. In order to account for the turbulence/chemistry interaction, this SLFM formulation employs a presumed probability distribution function (PDF) closure model. The SLFM includes the effects of strain rate, species diffusion, and momentum diffusion with changing duct velocity and fuel jet velocity. The PDF-closure accounts for the effect of turbulence. This allows us to generate a 3-dimensional reaction rate field, which we then spatially average over transverse planes to create a 1-dimensional reaction rate profile.

Although the transition process between ram and scram is governed by a complex fluid/flame interaction, it is possible to predict the mode of operation of a flowpath based on 1-D flow properties. Again, in order to avoid a time-stepping formulation, the steady-state combustor model is applied within an iterative root-finding scheme to determine conditions under which shocks are required in the isolator. This procedure speeds up computation of the combustor mode of operation, but it is not possible to compute transients or oscillatory behavior (going back and forth between two modes) in this way.

A similar effort was previously described by Merker [42], using the unsteady form of the same conservation equations. Although an unsteady simulation has the advantage of allowing transients and one-dimensional waves to be considered, its principal downside is increased simulation time. The method presented in this paper requires 5 to 30 steps to converge, while the scheme presented in [42] would require at least as many time steps as spatial steps in order to converge. Thus, it would take about 500 steps to reach steady state for the full-vehicle-length simulations shown here. Since the present effort seeks short run times, it was deemed appropriate to use only the steady conservation equations. Frequently in continuous-flow devices, the unsteady equations are used to consider the effect of perturbations to steady-state operation, extending the model. The method presented here is compatible with such an approach.

In the validation section, 4, I compare results of MASIV to CFD solutions from the commercially available Fluent[43] code, to profiles of wall pressure and heat release rates measured by Micka et.al.. [44], and to wall pressure and regime diagrams of Fotia [45, 46].

2.2   Combustor Model

The model is designed to simulate flow paths that have a general 1-D character but contain regions where 3-D mixing and combustion occur. For example, in a dual-mode ramjet/scramjet, most of the flow is nearly 1-D and can be realistically modeled by a set of ordinary differential equations that represent the conservation equations for a variable-area duct with friction and wall heat transfer. However, the region surrounding the fuel jet near each injector is best represented by the 3-D turbulent combustion of a jet in cross-flow. We developed a reduced-order modeling strategy that combines the known 3-D scaling relations for a jet in cross-flow with a set of flamelet lookup tables. An assumed PDF approach is used to include the appropriate 3-D turbulence properties in a statistical sense, and the local interaction of turbulence with finite-rate chemistry. We then spatially average the 3-D reaction rates over planes perpendicular to the main flow direction, which gives us a lookup table of the resulting 1-D reaction rates. These values are inserted into the source terms in the differential equations for species conservation in the solution of the ODEs describing the main flow. Using this approach, the main flow can be treated as a 1-D flow, but the local 3-D turbulent combustion and mixing around each fuel jet can be computed, and their influence on the overall heat release retained.

In order to develop a ROM-formulation for computationally efficient application in MDO, several modeling assumptions are introduced. The main assumption arises from presenting the fuel injection and flame structure through the self-similar solution of a jet in cross flow. Currently, we only consider the perpendicular injection of fuel in a cross-flow, and the self-similar modeling constants are determined from low-speed experiments. However, it is noted that this model can be improved as further results for scaling relations under high-speed flow conditions become available. Another potential model limitation arises from the flamelet assumption, in which a two-stream combustion process between fuel and oxidizer is considered. Multi-stream systems, that arise, for instance, by injecting different fuels or the successive mixing of different reactants currently are not considered. However, the flamelet-model can be extended to account for more complex information by considered multi-stream and non-adiabatic processes [47, 48]. In the present work, hydrogen/oxygen combustion is considered. More complex mechanisms and hydrocarbon combustion can be incorporated in a straightforward way without increase in computational complexity of the ROM-formulation.

2.2.1 Conservation Equations

For the description of a stationary turbulent reacting flow, a Reynolds-averaged approach is employed, in which an instantaneous flow field quantity $\phi = \phi(t, \mathbf{x})$, $\mathbf{x} = (x, y, z)$ is separated into mean and fluctuating contributions:

$$\phi = \overline{\phi} + \phi' \qquad \text{with} \qquad \overline{\phi}(\mathbf{x}) = \frac{1}{T} \int_t^{t+T} \phi(t, \mathbf{x}) \, dt \tag{2.5}$$

and a corresponding Favre-averaged quantity is evaluated as $\widetilde{\phi} = \overline{\rho\phi}/\overline{\rho}$ and $\phi = \widetilde{\phi} + \phi''$.

For the 1-D model, we assume that properties are homogeneous in each y-z plane so that for each variable the value on that plane is equal to the area-average of the variable. Note that in this model, x is in the downstream axial direction in the combustor, y is the upward transverse direction and z is span-wise direction. The spatial average is defined by the following equation.

$$\langle Q \rangle = \frac{1}{A} \iint_A Q \, dx dy \tag{2.6}$$

where A is the cross-sectional area. In general, however, we will refrain from writing the variables in angle brackets, $\langle \cdot \rangle$, to make equations easier to read. Unless otherwise specified, it should be assumed that variables are area-averaged.

MASIV solves for the 1-D evolutions of a set of ODEs for all flow field quantities describing the combustion process. The derivation of these equations proceeds from well-known principles [15, 34], but some finer points deserve attention so they are described in section A. First, we consider the spatial derivative of the equation of state

$$\frac{1}{p}\frac{dp}{dx} = \frac{1}{T}\frac{dT}{dx} + \frac{1}{\rho}\frac{d\rho}{dx} - \frac{1}{W}\frac{dW}{dx} \tag{2.7}$$

to compute the pressure derivative where p is the pressure, T is the temperature, ρ is the density and W is the molecular weight of the mixture. Next, we employ the mass conservation equation

$$\frac{1}{\rho}\frac{d\rho}{dx} = \frac{1}{\dot{m}}\frac{d\dot{m}}{dx} - \frac{1}{u}\frac{du}{dx} - \frac{1}{A}\frac{dA}{dx} \tag{2.8}$$

to find the density derivative where $\dot{m}$ is the total mass flow rate in the duct, and u

is the velocity. Next, we use the species conservation equation

$$\frac{dY_i}{dx} = \frac{\dot{\omega}_i}{\rho u} + \frac{1}{\dot{m}}\frac{d\dot{m}_i}{dx} - \frac{Y_i}{\dot{m}}\frac{d\dot{m}}{dx}$$

(2.9)

in order to account for mass addition to and reaction in the duct. In (2.9) Y_i is the mass fraction of each species, $\dot{\omega}_i$ is the volumetric mass generation rate of each species and $\frac{d\dot{m}_i}{dx}$ is the rate of mass addition through the walls for each species. Next, we use the momentum conservation equation

$$\frac{1}{u}\frac{du}{dx} = -\frac{1}{\rho u^2}\frac{dp}{dx} - \frac{C_f}{2A}\frac{dS_w}{dx} - \frac{(1-\varepsilon)}{\dot{m}}\frac{d\dot{m}}{dx}$$

(2.10)

to find the derivative of axial velocity. A source term accounts for momentum carried into the duct by mass added through the walls. Here C_f is the wall friction coefficient and $\frac{dS_w}{dx}$ is the rate of change of total wetted area with downstream distance. The direction parameter ε is $u_{inj,x}/u$ where $u_{inj,x}$ is the x-component of the injected gas. Values of 1 and 0 correspond to parallel and perpendicular injection, respectively. The second term on the right-hand side represents friction forces and the third term represents momentum added through the walls. Finally, we use the energy conservation equation

$$\frac{1}{h_0}\frac{dT}{dx}\sum_i c_{p,i}Y_i =$$
$$-\frac{u}{h_0}\frac{du}{dx} - \frac{1}{\dot{m}}\frac{d\dot{m}}{dx} + \frac{1}{h_0\dot{m}}\frac{\rho u C_f(h_{aw}-h_w)}{2\mathrm{Pr}^{2/3}}\frac{dS_w}{dx}$$
$$+\frac{1}{h_0\dot{m}}\frac{\rho u^3 C_f}{2}\frac{dS_w}{dx} - \frac{1}{h_0}\sum_i h_i\frac{dY_i}{dx} + \frac{1}{h_0\dot{m}}\sum_i h_i\frac{d\dot{m}_i}{dx}$$

(2.11)

to find the rate of change of temperature in the duct. In (2.11) h_0 is the stagnation enthalpy of the flow and $c_{p,i}$ is the specific heat at constant pressure of each species. Note that these equations consider all sources of enthalpy including sensible and chemical. As required by the Reynolds analogy, h_{aw} is the enthalpy of the gas at an adiabatic wall and h_w is the gas enthalpy at the wall temperature. Several source terms describe the addition of energy to the duct by friction, wall heat addition and chemical reaction. The left-hand side of the equation represents the energy-normalized rate of change of temperature. The third term on the right-hand side represents heat lost to the walls which is computed using the Reynolds analogy. The fourth term represents work done by wall friction. The fifth term represents heat

25

added by combustion and the sixth term represents energy added to the volume by mass addition through the walls.

Equations (2.7) through (2.11) represent $4+n$ equations for $4+n$ unknowns (p, ρ, Y_i, u, T), where n is the number of species considered. In the present implementation of the MASIV model, we have included 9 species, corresponding to H_2-air chemistry with no nitrogen products, although in principle any chemistry set can be used.

2.2.2 Turbulent mixing model

We developed a mixing ROM in order to compute the chemical reaction rates ($\dot{\omega}_i$) for each species, which are required in (2.9). The ROM simulates the 3-D mixing and 3-D turbulent combustion processes for a fuel jet that is injected perpendicular to an air cross-flow. Then it reduces the 3-D local reaction rates to 1-D reaction rate profiles by spatially-averaging the computed 3-D reaction rates over each y-z plane. This preserves the 3-D mixing/combustion information and is an improvement over previous studies [29, 28, 34, 15, 49] that have unrealistically simulated the chemical reactions and mixing to be 1-D processes. At each spatial ($\mathbf{x}$) location, the mean chemical reaction rate of each species is computed by combining the mixture fraction and fluctuation information with flamelet lookup tables.

In general there are two ways to represent combustion: either as a reaction-rate limited process (premixed), or as a mixing-limited process. Previous work [29, 28, 34, 15, 49] has assumed that scramjet combustion is a reaction-limited process; this assumption is only realistic if fuel is mixed far upstream of the combustion region, which often does not occur in practical devices. In reality the conditions in a scramjet are mixing-limited. That is, fuel and air are not homogeneously mixed but instead there is a stoichiometric contour that surrounds any 3-D fuel jet, and the combustion actually occurs near this stoichiometric contour.

In order to account for this mixing-limited condition, we assume that the flow around the injectors is well-approximated by a 3-D jet in crossflow. Turbulent mixing properties are generated using gradient information from the assumed jet profile, which then allows us to compute the local reaction rate for each species. We then spatially average the resulting reaction rate field to get $\langle \dot{\omega}_i \rangle$ once the local reaction rates (including turbulent effects) have been modeled.

The first step is to compute the jet mixing profiles. Rather than store CFD information directly in lookup tables or POD basis functions, we use physical self-similarity arguments to rapidly create a solution. These scaling relations are algebraic relations

that were determined experimentally by Hasselbrink and Mungal [50]. They represent the 3-D mean mixture fraction field as function of **x** and give scaling relations for the other variables as functions of the mean mixture fraction field. Note that although this scaling law is simple, it provides reasonable agreement for jet shape for a wide variety of conditions. The constants used in this study are from experiments on fully subsonic jets, but recent investigations [51] have examined transonic flows and found similar relations (although different values for some constants). Note that subsonic and supersonic mixing relations are similar because the jet centerline and mixing rate parameters are based on simple conservation arguments. However, we are ignoring certain dynamics such as "barrel shocks" in the injectant and shocks in the cross flow caused by injection, which some authors have identified [52].
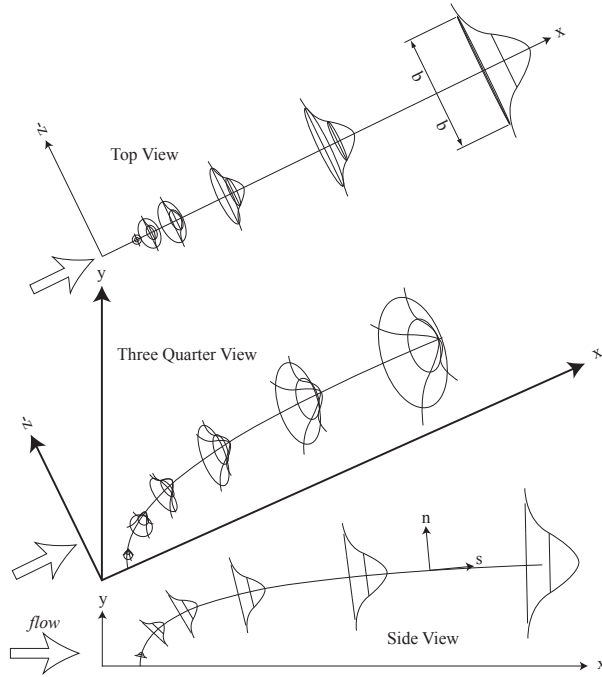
Figure 2.4: Schematic of the spreading profile for a jet in crossflow

The jet centerline penetration and spreading can be computed for each point using the jet scaling relationships [40]. This relationship is valid for momentum ratio $r_u \gg 1$, where r_u is defined as

$$r_u = \left[\frac{\rho_{inj}}{\rho} \left(\frac{u_{inj}}{u} \right)^2 \right]^{1/2} \tag{2.12}$$

and the injection density ρ_{inj} and velocity u_{inj} are known. The jet centerline path

27

relationship

$$\frac{y_{CL}}{d_{inj}} = c_1 \left(\frac{x_{CL}}{d_{inj}}\right)^{c_2} r_u^{2/3} \tag{2.13}$$

then traces the centerline path of the fuel jet. We assume that the fuel injector is choked so the stagnation pressure and temperature of the fuel line are sufficient to compute conditions at the injector. The coordinates x_{CL} and y_{CL} define the centerline of the jet and d_{inj} is the injector diameter.

The normalized concentration of injected fuel is given by another scaling relationship [50]:

$$\xi = c_3 \left[\frac{\rho_{inj}}{\rho} \left(\frac{u_{inj}}{u}\right)^{-1} \left(\frac{x_{CL}}{d_{inj}}\right)^{-2}\right]^{1/3} \tag{2.14}$$

where ξ is the ratio of the mole fractions of the streams. The mean mixture fraction $\tilde{f}_{CL}$ is assumed to be 1 in the injected gas stream (pure fuel) and 0 in the cross flow (pure oxidizer)

$$r_w = \frac{W_{inj}}{W} \tag{2.15}$$

$$\tilde{f}_{CL} = \frac{\xi r_w}{1 + (r_w - 1)\xi} \tag{2.16}$$

where r_w is the ratio of molecular weights of the injectant and cross-flow.

The mixture fraction at a given point is determined by the centerline mixture fraction corresponding to that point, the jet spreading distance (b), which is a function of distance from the injector along jet centerline (s), and the distance from the jet centerline (n)

$$\tilde{f}(s, n) = \tilde{f}_{CL} \exp\left(\frac{-n^2}{2b^2}\right) \tag{2.17}$$

Values of n and b are computed using the following equations.

$$n^2 = (x - x_{CL})^2 + (y - y_{CL})^2 + z^2 \tag{2.18}$$

$$\frac{b}{d_{inj}} = c_4 r_u^{2/3} \left(\frac{x_{CL}}{d_{inj}}\right)^{c_2} \tag{2.19}$$

Note that the orientation of the (s, n) frame compared to the (x, y, z) frame is shown in Fig. 2.4. Thus, by computing the shortest perpendicular distance from a given point to the jet centerline, the mixture fraction can be computed.

The mixture fraction variance $\widetilde{f'^2}$ is computed using the Prandtl mixing length

argument. Measurements indicate that mixture fraction variance is essentially a function of the gradient of the mean mixture fraction, so that

$$\sqrt{\widetilde{f'^2}} = \frac{c_5}{c_4} b |\nabla \widetilde{f}| \tag{2.20}$$

which is analogous to the mixing length concept for velocity fluctuations [53]

$$\sqrt{\widetilde{u'^2}} \sim b |\nabla \widetilde{u}| \tag{2.21}$$

The constants c_1-c_5 are experimentally determined. Their values in MASIV are given in Table 2.1. Note that we set c_3 in order to fit the experimental data as shown in section 4.1. This is because the data of Hasselbrink and Mungal were measured in low speed jets where diffusive effects are maximized, but the case in question is a high-speed ram case. In high-speed flows, especially transonic ones, some mixing is suppressed due to the speed and the shock pattern involved. Initial estimates based on more recent work on transonic (ram) cases [51] show values for c_3 that may be as high as 1.24.

Table 2.1: Experimental constants for jet mixing model.

Constant	Experimental Range	MASIV value
c_1	1.2 to 2.6 [50]	1.6
c_2	0.28 to 0.34 [50]	$\frac{1}{3}$
c_3	0.68-0.95 [54]	1.3
c_4	0.76 [50]	0.76
c_5	0.0084-0.0093 [54]	0.009

Finally, we determine the mean scalar dissipation rate, $\widetilde{\chi}$ using the formula

$$\widetilde{\chi} = 2D_T |\nabla \widetilde{f}|^2 \tag{2.22}$$

where D is the molecular diffusion coefficient and D_T is the turbulent scalar diffusion coefficient. In the following, we model D_T as [55]

$$D_T = \frac{\nu_T}{\text{Sc}_T} \tag{2.23}$$

where $u_{inj} d_{inj}/\nu_T = 45$. Here, the value of $u_{inj} d_{inj}/\nu_T$ is taken to be a tunable parameter, and the value 45 was found to give best agreement with the experimental results. Peters [55] suggests a value between 60 and 70 and Schlichting [56] a value

of 61, however both of these are for low-speed jets, so the lower value we have chosen represents some mixing suppression due to the high speed of the flow in question. The turbulent Schmidt number is $Sc_T = 0.7$.
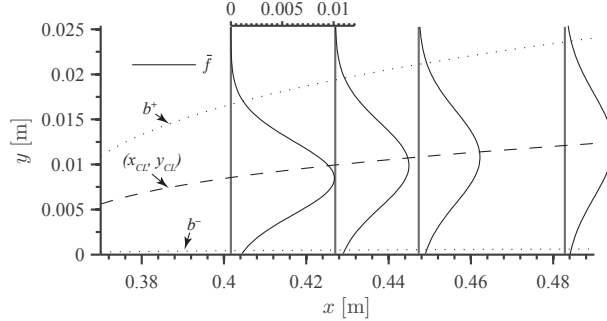
(a) Mean mixture fraction, $\widetilde{f}$ computed by MASIV
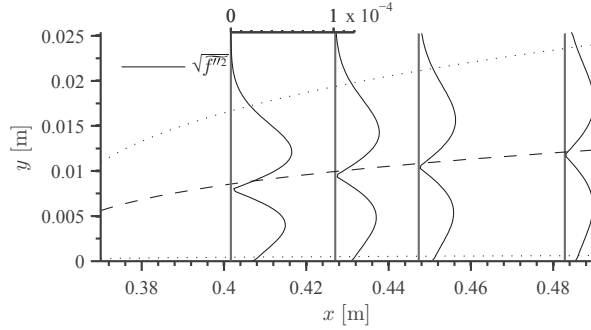
(b) Mixture fraction RMS fluctuation, $\sqrt{\widetilde{f''^2}}$ computed by MASIV
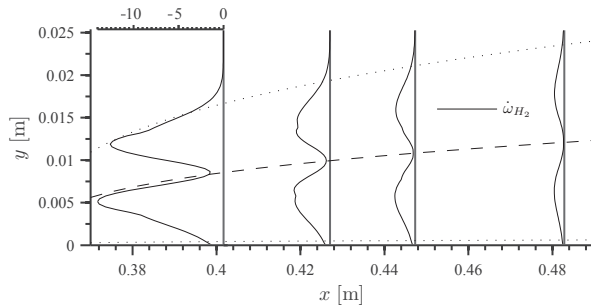
(c) Production rate H_2, $\dot{\omega}_{H_2}$, in $kg/m^3/s$

Figure 2.5: MASIV computed profiles of mean mixture fraction, mixture fraction fluctuation and local rate of generation of H_2 in the jet centerline x-y plane. The x-locations shown are those marked in Fig. 2.6

Fig. 2.5 illustrates some profiles of mean mixture fraction, mixture fraction variance and reaction rate for the experimental conditions examined in this work. Note that the reaction rate depends on both the mean mixture fraction and the variance, indicating the roles of both fuel concentration and turbulent mixing on the reaction

30
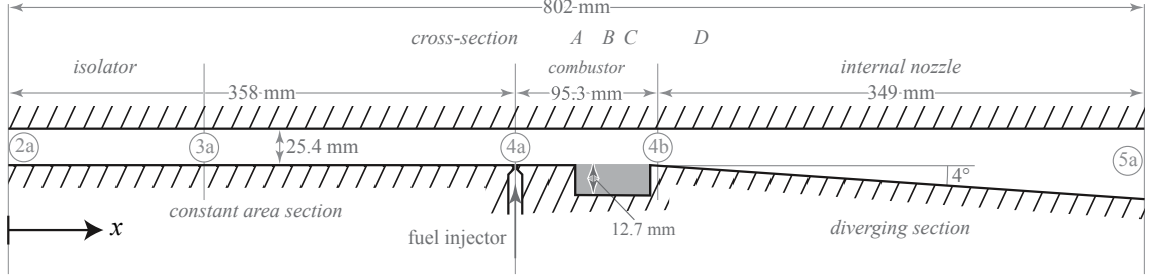
Figure 2.6: Duct geometry for simulation. Note that only the experiment and Fluent simulations include the cavity. MASIV simulations do not include cavity to avoid reversed-flow regions.

rate profile. Also, the mean mixture fraction and the mixture fraction variance are low because these planes are relatively far downstream from the injector.

2.2.3 Flamelet Combustion Model for Diffusion Flames

In the flamelet model, a turbulent diffusion flame is considered to be an ensemble of laminar flamelets [55, 41]. At sufficiently large Damköhler number or sufficiently high activation energy, chemical reactions and heat transfer occur in thin layers. If the characteristic length scale of these layers is smaller than that of the surrounding turbulence, the turbulent structures are unable to penetrate the reaction zone and are unable to destroy the flame structure. The effect of turbulence in this so-called flamelet regime results in a deformation and stretching of the flame sheet. With this notion, a flamelet can be considered as a thin reaction zone surrounded by a molecular transport layer, which, in turn, is embedded with a turbulent flow [57]. The structure of the flame in the flamelet regime can be described by the steady flamelet equations [41]

$$-\frac{\chi}{2}\frac{\partial^2 \boldsymbol{\psi}}{\partial f^2} = \dot{\boldsymbol{\omega}} \tag{2.24}$$

These equations can be derived from an asymptotic analysis of the conservation equations for species and energy, which are here denoted by the vector $\boldsymbol{\psi} = (\mathbf{Y}, h)^T$, and $\dot{\boldsymbol{\omega}}$ is the vector of the corresponding source terms. The scalar dissipation rate, appearing in Eqs. (2.24), is modeled from the solution of a counter-flow diffusion flame [58], and is expressed in terms of its value at stoichiometric mixture fraction and an analytical expression [58, 59]:

$$\chi = \chi_{st} F(f) \tag{2.25}$$

31

The solution of the steady flamelet equations can be represented by the so-called S-shaped curve [58], and all thermochemical quantities, collectively denoted by the vector $\boldsymbol{\phi} = (\nu, \dot{\boldsymbol{\omega}}, \ldots)^T$, can then be parameterized in terms of mixture fraction and scalar dissipation rate, *viz.*,

$$\boldsymbol{\phi} = \boldsymbol{\phi}(f, \chi_{st}) \tag{2.26}$$

This state-space parameterization represents the instantaneous thermochemical quantities, and does not account for turbulence/chemistry interaction. To account for the coupling between combustion and the turbulent flow field, a presumed PDF closure model is employed, which is described in the following section.

To account for the turbulence/chemistry interaction, the state relation (2.26) must be formulated for Favre-averaged quantities. These quantities are computed by employing a presumed joint PDF for mixture fraction and stoichiometric scalar dissipation rate:

$$\widetilde{\boldsymbol{\phi}} = \int_0^\infty \int_0^1 \boldsymbol{\phi}(f, \chi_{st}) \widetilde{P}(f) P(\chi_{st}) df \, d\chi_{st} \tag{2.27}$$

in which it is assumed that f and χ_{st} are statistically independent.

The marginal PDF of mixture fraction is modeled by a beta-distribution, [58] whose shape is fully characterized by the mean and variance of the mixture fraction. To model the distribution of the stoichiometric scalar dissipation rate, a log-normal distribution function is employed, which is presented as:

$$P(\chi_{st}) = \frac{1}{\chi_{st}\sigma\sqrt{2\pi}} \exp\left\{-\frac{1}{2\sigma^2}\left[\ln\left(\frac{\chi_{st}}{\widetilde{\chi}_{st}}\right) + \frac{\sigma^2}{2}\right]^2\right\} \tag{2.28}$$

in which σ is the standard deviation of the PDF and is set to unity [60], and σ is related to the stoichiometric scalar dissipation rate via

$$\sigma^2 = \ln\left(1 + \frac{\widetilde{\chi''^2_{st}}}{\widetilde{\chi}^2_{st}}\right) \tag{2.29}$$

With this, the Favre-averaged thermochemical state-space quantities can be expressed in terms of the first two moments of the mixture fraction and the mean stoichiometric scalar dissipation rate:

$$\widetilde{\boldsymbol{\phi}} = \widetilde{\boldsymbol{\phi}}(\widetilde{f}, \widetilde{f''^2}, \widetilde{\chi}_{st}) \tag{2.30}$$

This gives $\dot{\boldsymbol{\omega}}(\widetilde{f}, \widetilde{f''^2}, \widetilde{\chi}_{st})$, which is mapped to (x, y, z) space. Note that a minor inconsistency is introduced here and the values obtained for species mass fractions in

32

the 1-D integration will not necessarily correspond to the values obtained for local mass fractions in this step. In order to impose continuity and atom conservation on the flow, only the area-averaged reaction rates are used in the 1-D integration and not the local mass fractions as computed by the flamelet. Hence, the inconsistency is eliminated after the jet mixing and flamelet lookup step.

Next $\dot{\boldsymbol{\omega}}(x, y, z)$ is integrated to determine the 1-dimensional rate of reaction of each species (recall equation 2.6):

$$\langle \widetilde{\dot{\omega}}_i \rangle(x) = \frac{1}{A} \iint \widetilde{\dot{\omega}}_i(x, y, z) dy \, dz \tag{2.31}$$

These functions are tabulated for a given chemistry prior to the simulation.

2.2.4 Solution Procedure

Let us begin by considering the conservation equations and the equation of state (equations 2.7 to 2.11), solving them in the following manner. It is convenient to avoid formulating the problem in terms of c_p and directly use the enthalpy curve fits which are available from NASA CEA [61, 62], because if specific heats vary, using enthalpy instead results in a simpler formulation. NASA CEA is recommended because it uses many sources for its chemistry information, and has current and extensive information.

Similarly, the sound speed (a) for a reacting flow is defined as $a^2 = \left(\frac{\partial p}{\partial \rho}\right)_s$, which produces different results for equilibrium and frozen flows [63]. This is because the variation of species mass fractions provides multiple paths for the state variables to follow. This difficulty is avoided by formulating the problem in terms of velocity rather than Mach number. This is what Heiser and Pratt [5] call enthalpy-kinetic energy (H-K) space. It is more convenient than the typical temperature-Mach number (T-M) space (which would require both c_p and a to be computed at solution time), and results in a simpler set of equations. We compute a and M in post-processing after the solution has been found.

Other quantities indicated in Eq. (2.7) to (2.11) which are required to solve the system include the area profile ($A(x)$) and its derivative $\frac{dA}{dx}$. The mass addition profile $\frac{d\dot{m}_i}{dx}(x)$ must also be given and can be summed to give $\sum_i \frac{d\dot{m}_i}{dx} = \frac{d\dot{m}}{dx}(x)$, the total mass addition profile. For the integration step the reaction rates are pretabulated using the method described in section 2.2.3 to yield $\dot{\omega}(x)$. A Prandtl number Pr, a skin friction coefficient C_f, and a wall temperature T_w are all assumed.

Intermediate quantities are computed at each step:

$$\dot{m} = \rho u A \tag{2.32}$$

$$\frac{dW}{dx} = -W^2 \sum_i \left(\frac{1}{W_i} \frac{dY_i}{dx} \right) \tag{2.33}$$

$$\frac{dS_w}{dx} = \sqrt{16A + \left(\frac{dA}{dx} \right)^2} \tag{2.34}$$

$$\frac{d\dot{m}}{dx} = \sum_i \frac{d\dot{m}_i}{dx} \tag{2.35}$$

$$h_i = h_i(T) \tag{2.36}$$

$$h = \sum_i Y_i h_i \tag{2.37}$$

$$h_0 = h + \frac{u^2}{2} \tag{2.38}$$

$$h_w = h(T_w) \tag{2.39}$$

$$h_{aw} = h + \sqrt{\mathrm{Pr}} \frac{u^2}{2} \tag{2.40}$$

Once $\dot{\boldsymbol{\omega}}(x)$ has been determined, there is enough information to solve equations 2.7 through 2.11. A stiff solver is required due to the rapid reaction rates. We used MATLAB's `ode23tb` because it is capable of handling stiff equations.

2.3   Pure scram mode

"Pure scram mode" refers to the purely-supersonic-combustion mode of the engine, in which no shocks or separated boundary layers are generated in the isolator section of the duct. There is no need for a PCST because the minimum Mach number in the duct does not approach unity. In these cases, the condition at the beginning of the isolator is provided by the inlet code, and propagated backward with no change until fuel is injected. In the combustor section of the duct, the combustor model is applied as described in section 2.2. This provides the condition at the end of the combustor section of the duct.

The assumptions in the isolator that boundary layers are relatively thin, that there are no large separated regions, and that there are no shocks are possibly simplifications. It is not yet well understood from an experimental point of view if these conditions are met in real devices.

2.4 Ram mode

When the engine of a hypersonic vehicle changes from a supersonic combustion mode to a subsonic combustion mode, new physics are introduced in the flowpath which can cause changes in the thrust and moment produced by the engine. It has been experimentally observed [64, 65] that wall pressures in a scram profile are dramatically different from those of a ram profile and that components can have fundamentally different performance depending on the thermodynamic and chemical characteristics of the incoming flow [65]. Although it is important to compute thrust accurately in either mode, it is perhaps more important to understand the qualitative changes associated with mode transition. Abilities to predict in which mode the engine will operate and flow properties on either side of a transition event are useful in order to design stable combustors. Knowledge of when mode transition may occur is useful in order to design stabilizing controllers that are viable over the whole range of operation of the vehicle. Vehicle design studies also depend on understanding the various operating regimes the engine may encounter. Finally, transition between modes may cause problems such as flame blowout or insufficient thrust. The example thrust maps shown in this paper highlight the difficulty of designing a dual-mode combustor (that is, a combustor that must operate over a wide range of Mach numbers in both subsonic-combustion and supersonic-combustion mode), and point out the inherent problem in designing a flowpath without considering off-design performance.

The major contribution of this section is the development of an iterative shooting method to solve for the performance of transonic 1-D flows. To investigate the ram-scram transition, a new model was developed which is based on the one-dimensional analysis of Shapiro [15]. This new approach requires an internal solver for one-dimension flow equations, which the authors have previously developed ([22] and above) and which is part of the larger vehicle dynamics model.

2.4.1 Simple cases using Mach number forcing

Previous authors [5, 15] have proposed a method to solve the thermal choking problem using several limiting assumptions. Governing equations and boundary conditions were initially proposed by Shapiro, who considered the case of heat addition and friction in a single-component gas in a variable-area duct. We build upon Shapiro's simplified analysis by adding high-temperature gas properties, gases comprising multiple species, finite-rate chemistry, and turbulent mixing of a jet in cross flow. However, let us begin with Shapiro's analysis in order to explain the procedure.

Using elementary conservation equations, it is possible to solve for the evolution of the flow properties in any pseudo 1-D duct [22]. In order to compute the change in Mach number, Shapiro proposes a function called G. The G-function is simply the forcing term on the right-hand side of the Mach number equation for 1-D flow. For example, for 1-D flow with heat addition and area change (but no friction or mass addition), the Mach number equation is [15]

$$
\frac{1}{M^2}\frac{dM^2}{dx} = -\frac{2\left(1 + \frac{\gamma-1}{2}M^2\right)}{1 - M^2}\frac{1}{A}\frac{dA}{dx}
$$
$$
+ \frac{(1 + \gamma M^2)\left(1 + \frac{\gamma-1}{2}M^2\right)}{(1 - M^2)}\frac{1}{T_0}\frac{dT_0}{dx} \tag{2.41}
$$

In general, G represents all the terms in the right-hand side of (2.41), so Shapiro writes that (2.41) can be written more generally as

$$
\frac{1}{M^2}\frac{dM^2}{dx} = \frac{G(x)}{1 - M^2} \tag{2.42}
$$

and so in (2.41), G is

$$
G = \left(1 + \frac{\gamma - 1}{2}M^2\right)\left[-2\frac{1}{A}\frac{dA}{dx} + (1 + \gamma M^2)\frac{1}{T_0}\frac{dT_0}{dx}\right] \tag{2.43}
$$

Numerous authors show how (2.43) can be derived from the conservation equations. Here, x is the axial coordinate, M is Mach number, G is Shapiro's forcing function, $A(x)$ is the cross-sectional area distribution in the duct, T_0 is the stagnation temperature, and γ is the ratio of specific heats. The function G is more complex when other effects are added, such as mixtures of gases and finite-rate combustion chemistry.

To apply (2.42) Shapiro assumes that the mass flow rate is constant in the duct, and that the heat added per unit length and duct area profile $A(x)$ are known. Assuming constant specific heats, the stagnation temperature is only a function of rate of heat addition per unit length, $\mathrm{d}\dot{Q}/\mathrm{d}x = \dot{m}(c_p\mathrm{d}T_0/\mathrm{d}x)$, where $\dot{m}$ is the mass flow rate. In this case, (2.42) can be integrated directly as an initial value problem, giving $M(x)$. This approach is sufficient except when $M = 1$ somewhere in the domain, in which case there is a singularity in the right-hand side of the equation.

In order to solve the equations through the sonic point it is required that (2.42) be indeterminate at the singular point; the numerator must go to zero when the denominator goes to zero. This implies that $G = 0$ when $M = 1$. Using L'Hôpital's

rule

$$\left(\frac{1}{M^2}\frac{dM^2}{dx}\right)^* = \frac{(\mathrm{d}G/\mathrm{d}x)^*}{-(\mathrm{d}M^2/\mathrm{d}x)^*} \qquad (2.44)$$

where $(\cdot)^*$ indicates a quantity at the location where $M = 1$.

Now, consider a slightly rearranged version of (2.42),

$$\frac{M^3}{(M-1)^2}\frac{d(M-1)^2}{dx} = \frac{-G(x)}{(M-1)^2(M+1)} \qquad (2.45)$$

which indicates that $G > 0$ always forces the Mach number toward 1 and $G < 0$ always forces the Mach number away from 1. It is clear that in order for the flow to proceed through the sonic point, G must be initially positive, 0 when $M = 1$, and negative after that.

Usually, $A(x)$ is fixed, and in general $\mathrm{d}\dot{Q}/\mathrm{d}x$ cannot be arbitrarily specified, since it represents heat added by reaction (the rates of which are functions of the flow states) or by heat transfer from the walls (the rate of which is a function of the wall temperature and the flow temperature, among other parameters). When sufficient heat is added to cause thermal choking, an additional boundary condition (that $M = 1$ precisely where $G = 0$) is required. Downstream of the sonic point, the flow equations form a simple initial-value problem with initial condition corresponding to the sonic point.

In the simple case of no friction and no mass addition thermal choking occurs where $G = 0$ in (2.43) due to the correct combination of heat release and wall divergence [5]:

$$\frac{1}{A}\frac{dA}{dx} = \frac{1+\gamma}{2}\left(\frac{1}{T_0}\frac{dT_0}{dx}\right) \qquad (2.46)$$

Thus, Heiser and Pratt determine the location of thermal choking for simple cases by finding the minimum of the effective area distribution [5].

As Shapiro notes, however, since $G(x)$ depends on M^2, $\mathrm{d}G/\mathrm{d}x$ will depend on $\mathrm{d}M^2/\mathrm{d}x$, which means that it is usually impossible simply to solve the equations through the sonic point. There are at least two ways around this problem. The first is to solve the governing equations backward from M^-, which is a Mach number slightly below unity and from x^-, which is slightly upstream of the predicted sonic location, x_s. Downstream of the sonic point the equations are solved in the forward direction from x^+ and M^+, which are similarly defined. The second approach is to

use a shooting method to find solutions that approach $M = 1$ at x_s arbitrarily close to the sonic point and to estimate $\mathrm{d}G(x_s^-)/\mathrm{d}x$, which is then used to step through the singularity and proceed with the forward solution. Details of a shooting method approach are explained in Section 2.4.7.

2.4.2 Shooting method for reacting flows

In the present study we build upon Shapiro's simplified analysis by replacing the Mach number influence coefficient method, (2.43), with a set of differential equations in terms of velocity, u. The details of this method can be found in [22]. We have found that the frozen-flow Mach number, $M = u/\sqrt{\gamma p/\rho}$, where u is the flow velocity, p is the pressure, and ρ is the density, is appropriate for predicting the location of the singularity. This allows x_s to be estimated as the ODEs are solved, or (as here) a shooting method to be used for finding transonic solutions.

The conservation equations in section 2.2.1 contain temperature-dependent gas properties, multi-component gas mixtures, finite-rate chemistry, turbulent mixing of a jet in cross flow, and wall heat transfer and viscous drag. To solve transonic equations (2.42) the shooting method is preferred because the heat release rate profile, $\dot{Q}(x)$, is not specified *a priori*. Instead, it depends on the finite-rate chemistry, which is a function of $p(x)$ and $T(x)$. An example of the shooting method is shown in Fig. 2.10.

In order to perform the shooting method, it was necessary to define a residual function, y, which is used as a metric for the deviation between the present solution iteration and the correct solution. Values of y indicate the direction and distance from the current guess, $M_{3\mathrm{a}}^i$, to the correct solution, where $M_{3\mathrm{a}}$ is the Mach number at the entrance to the combustor. The need for such a function is evident if we consider what happens when the present guess, $M_{3\mathrm{a}}^i$, is too large. In this case, the Mach number will approach unity, but G will not cross zero, so this is not a valid solution. Figure 2.7 shows an example of this behavior. Note further that when the solution reaches a sonic condition without having the appropriate conditions on G it is impossible to continue solution of the ODEs in the duct. This becomes clear when considering (2.45), since for $G > 0$ at $M = 1$, the flow will never be able to depart from the sonic condition, and solution of the ODEs will fail.

When the present guess, $M_{3\mathrm{a}}^i$, is too small, the maximum Mach number on the interval will be less than unity, but we still require a way to estimate the distance away from the proper value of $M_{3\mathrm{a}}$. A function is required which is defined both when the maximum Mach number in the domain is less than unity and when the solution
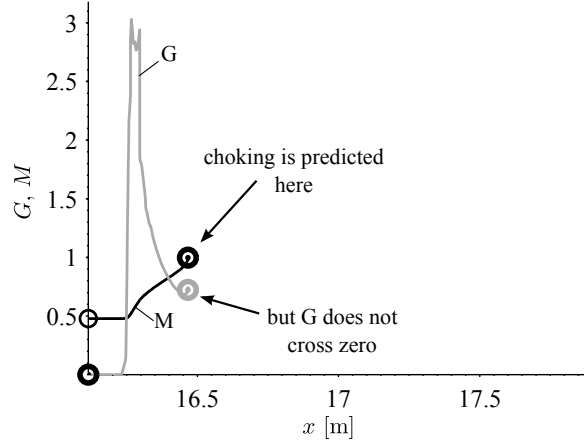
Figure 2.7: An iteration (same as Fig. 2.10a) in which $M = 1$ but solution of the ODEs fails due to inappropriate conditions on G.

fails due to a sonic condition occurring too early in the duct. Having testing different options extensively, we propose the function

$$y^i = \begin{cases} x_s^{i-1} - x_{M_{\max}}^i & \text{if choking occurs} \\ M_{\max}^i - 1 + \varepsilon & \text{otherwise} \end{cases} \qquad (2.47)$$

where $x_{M_{\max}}$ is the x-location of the maximum value of M in the duct, x_s^i is the best estimate at iteration i of the sonic location, $M_{\max}^i$ is the maximum Mach number achieved in a fully subsonic solution, and $\varepsilon > 0$ is some small number. The convergence tolerance of the iterative scheme (below, section 2.4.7) and the error tolerance of the ODE integrator must both be smaller than ε so that the error, y, can be driven to 0. The use of ε prevents the ODEs from having to be evaluated at the singular point, $M = 1$.

The sonic location can be found using G. As $M \to 1$, $x(G = 0) \to x_s$. Thus, if the location of choking is driven toward x_s (the point at which transonic solutions are allowed), the point at which $M = 1$ will be driven to the point at which $G = 0$ by selection of the appropriate upstream boundary condition, M_{3a}.

2.4.3 Thermal choking of a reacting flow

If heat is added to a flow such that $\mathrm{d}T_0/\mathrm{d}x$ is known *a priori* then the function G is known from (2.43). However, in a reacting flow the gas composition changes and G cannot be computed ahead of time. The principle is the same and G can be defined

in terms of primitive variables:

$$G = \left(1 - \frac{\rho u}{\gamma p}\right)\left(\frac{2}{u}\frac{du}{dx} + \frac{1}{\rho}\frac{d\rho}{dx} - \frac{1}{p}\frac{dp}{dx}\right) \tag{2.48}$$

To compute G, $\mathrm{d}u/\mathrm{d}x$, $\mathrm{d}\rho/\mathrm{d}x$, and $\mathrm{d}p/\mathrm{d}x$ are either found by (2.10), (2.8), and (2.7), respectively, or can be estimated using finite differences after the ODEs have been solved. We calculate G using finite differences. A second-order scheme was used to compute $G(\rho, u, p, \gamma)$ and $\mathrm{d}G/\mathrm{d}x$. The location of the zero crossing was then estimated by interpolation,

$$x_s^i = x^- - \frac{G^-}{\mathrm{d}G/\mathrm{d}x^-} \tag{2.49}$$

where again a point just to the upstream side of the sonic point is denoted by $-$. Figure 2.8 shows the estimation of the location where a sonic condition is allowed based on the location of the zero-crossing of the G-function. The discontinuity in G is caused by a discrete change in the rate of change of cross-sectional area $\left(\frac{dA}{dx}\right)$ due to a constant-area section connecting to a diverging section.
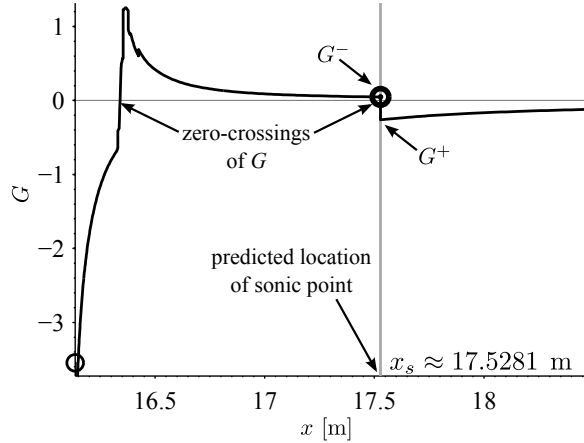
Figure 2.8: Solution for $G(x)$ at iteration 2 of the ram routine, showing that the estimate of the sonic location is already near the proper value of $x_s = 17.5281\,\mathrm{m}$

Note that although there are two locations where G crosses zero, at only one of them does G change from positive to negative. This location, x_s, is then identified as the current best estimate of the location where choking is allowed, and the other location, where G goes from negative to positive, is discarded.

2.4.4 Pre-combustion shock train

Section 2.4.3 provides a rapid way to compute the thermal choking location and the correct value of M_{3a} that allow transonic solutions in 1-D ducts. A process must still be identified that begins at a supersonic upstream condition, M_2, and delivers condition M_{3a} to the subsonic portion of the duct. The other state variables, ρ_{3a}, p_{3a}, and u_{3a}, must also be computed as upstream boundary conditions for the ODE solver.
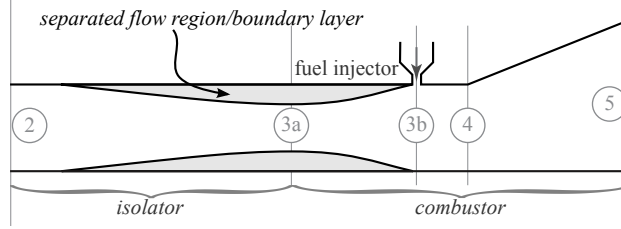
Figure 2.9: Separated region (area deficit) profile in generic scramjet duct.

A canonical scramjet is presented in Fig. 2.9, featuring a constant area isolator, fuel injection location, and diverging combustor. Flame stabilization components such as cavities or steps are omitted. Station ② is at the supersonic outflow of the inlet; station ③ₐ is at the beginning of the combustor; station ③ᵦ is at the fuel injectors; station ④ is at the beginning of the divergence in the combustor, and station ⑤ is at the beginning of the external nozzle.

Heiser and Pratt [5] write that the momentum of the flow will be carried by a core region with an area smaller than the physical area of the duct, while the rest of the duct area is filled with a boundary layer and separated flow having very little momentum. Conservation of momentum states that the total impulse is conserved,

$$I_{3a} = I_{\text{sep}} + I_{\text{core}} = I_2$$
$$= [p_{3a}(A_2 - A_{3a}) + 0] + (p_{3a}A_{3a} + \dot{m}u_{3a})$$
$$p_{3a}A_2 + \dot{m}u_{3a} = I_2 \tag{2.50}$$

which, when combined with the assumption that the isolator is adiabatic, yields [5]

$$\frac{p_{3a}}{p_2} = 1 + \gamma^2 M_2^2 - \gamma M_2 M_{3a}\sqrt{\frac{1 + \frac{\gamma-1}{2}M_2^2}{1 + \frac{\gamma-1}{2}M_{3a}^2}} \tag{2.51}$$

Here A_{3a} is the area of the core flow at station ③ₐ. The conditions at station ② (where the flow is supersonic) are computed separately by an inlet code [27] in the

case of vehicle simulations, or specified manually (as in the case of the experimental conditions shown below). The Mach number at the end of the PCST, M_{3a}, is computed by the analysis of section 2.4.2, so (2.51) predicts the pressure at station ③a. The temperature and velocity at station ③a are found by assuming that the stagnation temperature and gas properties do not vary in the isolator. Thus, the full state can be found at station ③a with knowledge of M_{3a}.

Heiser and Pratt also show how the core area may be computed based on conservation of mass and momentum, assuming an area deficit due to the separated region:

$$\frac{A_{3a}}{A_2} = \frac{1}{\gamma M_{3a}^2} \left[\frac{1}{p_{3a}/p_2} \left(1 + \gamma M_2^2\right) - 1 \right] \tag{2.52}$$

So the thickness of the separated flow region can be calculated as a function of the Mach number, M_{3a} at the end of the isolator. Note that (2.50), (2.51), (2.52) are valid at all points in the PCST.

Since $A_{3a} < A_2$ at all points in the PCST, (2.52) gives constraints on M_{3a}. As the area ratio goes to unity, the PCST solution tends to a supersonic case (nothing happens) or to a normal-shock solution (maximum entropy generation). The actual solution is expected both to be subsonic and to generate less entropy than a normal shock, so

$$\sqrt{\frac{1 + \frac{\gamma-1}{2} M_2^2}{\gamma M_2^2 - \frac{\gamma-1}{2}}} < M_{3a} < 1 \tag{2.53}$$

In order to account for the thickness of the separated region downstream of the PCST, a simple linear interpolation was used. The core area was assumed to be A_{3a} at $x = x_{3a}$ and $A_{3b} = A_2$ at $x = x_{3b}$, which is simply an approximation that boundary layers become very thin near the fuel injector.

2.4.5 PCST length scaling

In order to use (2.51) to find the distribution of $p(x)/p_2$ in the isolator, a distribution of Mach number, $M(x)$, is required in the PCST. Ikui [66] proposes a method for estimating the pressure rise as a function of x in the isolator. We used this method, but replaced Ikui's "fully mixed" boundary condition with the requirement that $\frac{dp}{dx} = 0$ at the end of the PCST, implying that the PCST must reach equilibrium. This assumption differs from Ikui's because instead of assuming that the PCST is associated

with a viscous mixing profile that goes from no boundary layer to fully developed pipe flow, we assume that the separated region described above effectively carries no momentum. This assumption is more consistent with the observation that pressure reaches a maximum at the end of the PCST [45].

Ikui uses the Crocco number,

$$w^2 = \frac{\frac{\gamma-1}{2}M^2}{1 + \frac{\gamma-1}{2}M^2} \tag{2.54}$$

along with the following differential equation, derived from conservation of mass, assuming that only the core flow carries any mass [66].

$$\frac{d^2w}{dx^2} - c^2w = 0 \tag{2.55}$$

$$w(0) = w_2, w(\ell) = w_3, \frac{dw(\ell)}{dx} = 0 \tag{2.56}$$

The solution of this differential equation is

$$w(x) = w_3 \cosh\{b(\ell - x)\} \tag{2.57}$$

$$\frac{p(x) - p_2}{p_3 - p_2} = \frac{w_2 - w(x)}{w_2 - w_3} \tag{2.58}$$

where $w(x)$ is the Crocco number between station ② and station ③ and $p(x)$ is the static pressure in the isolator between p_2 and p_3. The ratio of specific heats γ is assumed not to vary in the isolator. The estimated length of the PCST, ℓ, is determined by using Ikui's experimental correlation, $\ell = \frac{1}{c}\ln(w_2/w_3)$, where c is experimentally determined. Ikui reports $c = 0.114$, which is the value used here. Note that this value is for a normal shock train.

Note that (2.58) differs slightly from Ikui's result because of the assumption of different boundary conditions above. This also means that the constant changes to

$$b = c\frac{\cosh^{-1}(w_2/w_3)}{\ln(w_2/w_3)} \tag{2.59}$$

2.4.6 Expansion shock at $M = 1$

Once the location of the sonic point has been found and the associated strength of PCST has been computed, the last task is to compute conditions on either side of the sonic point. Using the shooting method, the conditions just upstream of the sonic

point are known to an acceptable degree of accuracy. Let us call the state at this point $\begin{bmatrix} \rho^- & p^- & T^- & u^- \end{bmatrix}^T$.

In order to compute a step that proceeds through the singularity using the method described by Shapiro, it is required that a step be taken precisely at x_s, and that $\mathrm{d}G/\mathrm{d}x$ be used at this location to compute $\mathrm{d}M^2/\mathrm{d}x$. Shapiro's approach was attempted using (2.7) to (2.11), but it was found to be needlessly complicated for several reasons. It requires placing points very close to the singularity to obtain accurate values for $\mathrm{d}G/\mathrm{d}x$, requires a custom Runge-Kutta solver that allows placing a point at x_s, and uses a different governing equation at this point, (2.44) instead of (2.43). Another undesirable property is that the value obtained for $\mathrm{d}G/\mathrm{d}x$ depends on the exact placement of x^-, since in any discretized implementation x^- is a finite distance from x_s and not a true limit. The most damaging requirement, however, is that of expressing (2.7) through (2.11) in a way that is consistent with (2.44). The equations involved are significantly more complex than those of the non-reacting case, but solving them exactly does not provide any real advantage since they are only to be used to obtain a supersonic condition.

A much simpler approach is to jump across the singularity using the shock-jump relations. Although this process, often known as an "expansion shock" destroys entropy, the error introduced can be rendered arbitrarily small by making x^- sufficiently close to x_s. In our experience, good accuracy of the scheme is maintained using relatively coarse tolerances, $\varepsilon = 0.005$ from (2.47).

Once the error, y, from section 2.4.2 has been reduced to an acceptable level, the subsonic integration is discontinued at x^-. Then, the shock-jump equation is applied using this subsonic condition and a new supersonic condition, $\begin{bmatrix} \rho^+ & p^+ & T^+ & u^+ \end{bmatrix}^T$, is obtained. Finally, since this supersonic condition only applies downstream of x_s, a new starting point is chosen, x^+, slightly downstream of x_s, and the integration is re-started.

2.4.7 Iterative procedure

This section describes the practical implementation of the procedure outlined in 2.4.1 to 2.4.6. In the shooting method outlined above, one simply searches for an initial condition, M_{3a}, that causes the Mach number to equal unity precisely when $G = 0$. The solution that meets this requirement is the allowed ram solution for the given boundary conditions at the beginning of the isolator (which must be supersonic). A detailed procedure for implementing this method follows.

1. The inlet solution (either from the inlet code [27] or manually specified) provides a supersonic upstream boundary condition for the isolator, (p_2, T_2, u_2).

2. Assume that the flow will remain supersonic throughout the isolator and combustor. Attempt to compute a scram solution. If the solution succeeds, then the engine operates in scram mode. No pre-combustion shock train is required; stop.

3. If the sonic point was approached (from above) at any x-location then this flow does not have a stable supersonic solution. Determine the ram-mode solution.

4. Assume that there is a PCST in the isolator which sets conditions at the beginning of the combustor. The PCST is of unknown strength. Bracket the condition which allows a transonic solution with $M_{3a}^{(1)}$ set by (2.53) and $M_{3a}^{(2)} = 1-10\varepsilon$. We have used $\varepsilon = 0.005$ with success.

5. Perform a search for the root of the error metric, y, as a function of M_{3a}. Terminate when $|M_{3a}^{i+1} - M_{3a}^i|/M_{3a}^i < \varepsilon/2$. Let $x_s = x_s^i$, which is the best prediction of the location of choking.

6. Estimate the new state at x_s^+ by using the shock-jump relations for M, p, and T at x_s^-. When the initial Mach number in the jump equation is less than unity, entropy is destroyed. However, the error incurred in this step can be made as small as required by selecting an appropriate tolerance, ε.

7. Re-start combustor solution at x_s^+, with the supersonic condition as computed above.

Figure 2.10 shows a typical ram-mode solution, showing only distinctive iterations. First, the solution is bracketed from below (step 1 in the iterative procedure) by guessing a value of $M_{3a}^{(1)} \approx 0.46$, which is the circled value shown in Fig. 2.10a. The solution is also bracketed from above in iteration 2 by guessing a value of $M_{3a}^{(2)} \approx 0.95$. Iterations 3 to 12 correspond to step 5 of the iterative procedure above. By iteration 2, the x-location of the sonic point can be predicted accurately, but the maximum Mach number is still less than unity, as shown in Fig. 2.10b. By iteration 7, as shown in Fig. 2.10d, M_{3a} is well-bounded from above, since the maximum Mach number of this iteration approaches 1. However, as iteration 5 (Fig. 2.10c) demonstrates, there is still uncertainty in the predicted choking location. By iteration 12, the uncertainties in the maximum Mach number and the location of choking have both been reduced

to an acceptable level (Fig. 2.10e), both converge to the same M_{3a} value, and choking occurs near the sonic location as predicted using the G-function. Figure 2.10f shows the final solution after completing steps 6 and 7 of the iterative procedure. The final value of M_{3a} is $0.7301 \pm \varepsilon$, and $x_s = 17.5281\,\mathrm{m}$. The actual search procedure used is a combination of bisection, Newton's method, and Müller methods. Best results were obtained after significant tuning of the convergence parameters involved.

2.5   Early scram

Between the ram-mode operation (subsonic combustion) and scram-mode operation (supersonic combustion), it has been experimentally observed that there exists a mode of operation in which a PCST is present, but the Mach number in the duct does not drop below unity across the duct [67, 68, 69]. This mode is called "early scram." The reason this mode can exist is that it is possible for the heat addition and other effects in (2.43) to lead to choking when attempting to compute the pure-supersonic-combustion scram ("pure scram") mode performance, but any PCST that is strong enough to reduce the Mach number below unity (ram mode) adds too much entropy to the flow to allow it to reach a suitable transonic solution as described above, in section 2.4.3. In other words, it is not possible to find a ram-mode solution that satisfies the required conditions on M and G. However, it is possible to find a solution if it is assumed that $M_{3a} > 1$.

It is impossible to ignore this situation, because the early scram mode exists *between* pure scram mode and ram mode. This is due to the fact that no entropy is generated in the isolator in pure scram mode (no PCST) and too much entropy is generated in the isolator in ram mode (strong PCST), for the given conditions to match properly such that $M = 1$ where $G = 0$. Fortunately, since the PCST equation (2.51) is based only on conservation and not on anything specific to ram mode, it is equally applicable for any Mach number between M_2 and the normal shock limit of (2.53).

However, a Mach number must be selected in order to compute the pressure. The matching condition of section 2.4.1 no longer applies, since the flow in the early scram mode will be supersonic throughout. At the mode transition boundaries, the following conditions are required:

1. From pure scram to early scram mode, performance is expected to be continuous. In the early scram mode solution, the minimum-entropy solution is

selected to achieve this requirement. This corresponds to the weakest isolator that guarantees the solution is supersonic throughout.

2. From early scram mode to ram mode, performance is expected to be discontinuous, because the ram mode solution generates more entropy than the limit early scram mode solution, which causes a difference in the pressure profile and a difference in the thrust. This difference has been recorded by several experimenters [45, 67].

Thus, the same iterative procedure as in section 2.4.7 can be used (including the same root-finding scheme), except that

$$
y^i = \begin{cases} x_s^{i-1} - x_{M_{\max}}^i & \text{if choking occurs} \\ -(M_{\max}^i - 1 - \varepsilon) & \text{otherwise} \end{cases} \tag{2.60}
$$

is used for the heuristic function.

2.6   Inlets and Nozzles

To compute the performance of inlets and nozzles, MASIV calls on the supersonic aerodynamic method using Riemann interactions (SAMURI) model, which computes the properties of the inlet and nozzle. SAMURI computes multiple shock and expansion wave interactions and was developed primarily by Derek Dalle [27, 37].

2.7   Vehicle Dynamics

The MASIV code computes flowpath performance from one end of the vehicle to the other. It accounts for all the air that moves through the engine in a stream tube, meaning that this air is accounted from before it interacts with the leading bow shock attached to the vehicle until it exits from the nozzle at the rear of the vehicle. All the air that interacts with the vehicle but that does not enter the engine flowpath is accounted inside of MASTrim, which is the external aerodynamics and trim code. This code was developed primarily by Dalle as well [4].

(a) Iteration 1, lower bound, $M_3^{(1)} = 0.4671$ (same as Fig. 2.7)

(b) Iteration 2, upper bound, $M_3^{(2)} = 0.9500$ (same as Fig. 2.8)

(c) Iteration 5, $M_3^{(5)} = 0.7138 \pm 0.0884$

(d) Iteration 7, $M_3^{(7)} = 0.7306 \pm 0.0168$

(e) Iteration 12, $M_3^{(12)} = 0.7301 \pm 0.0005$

(f) Final solution
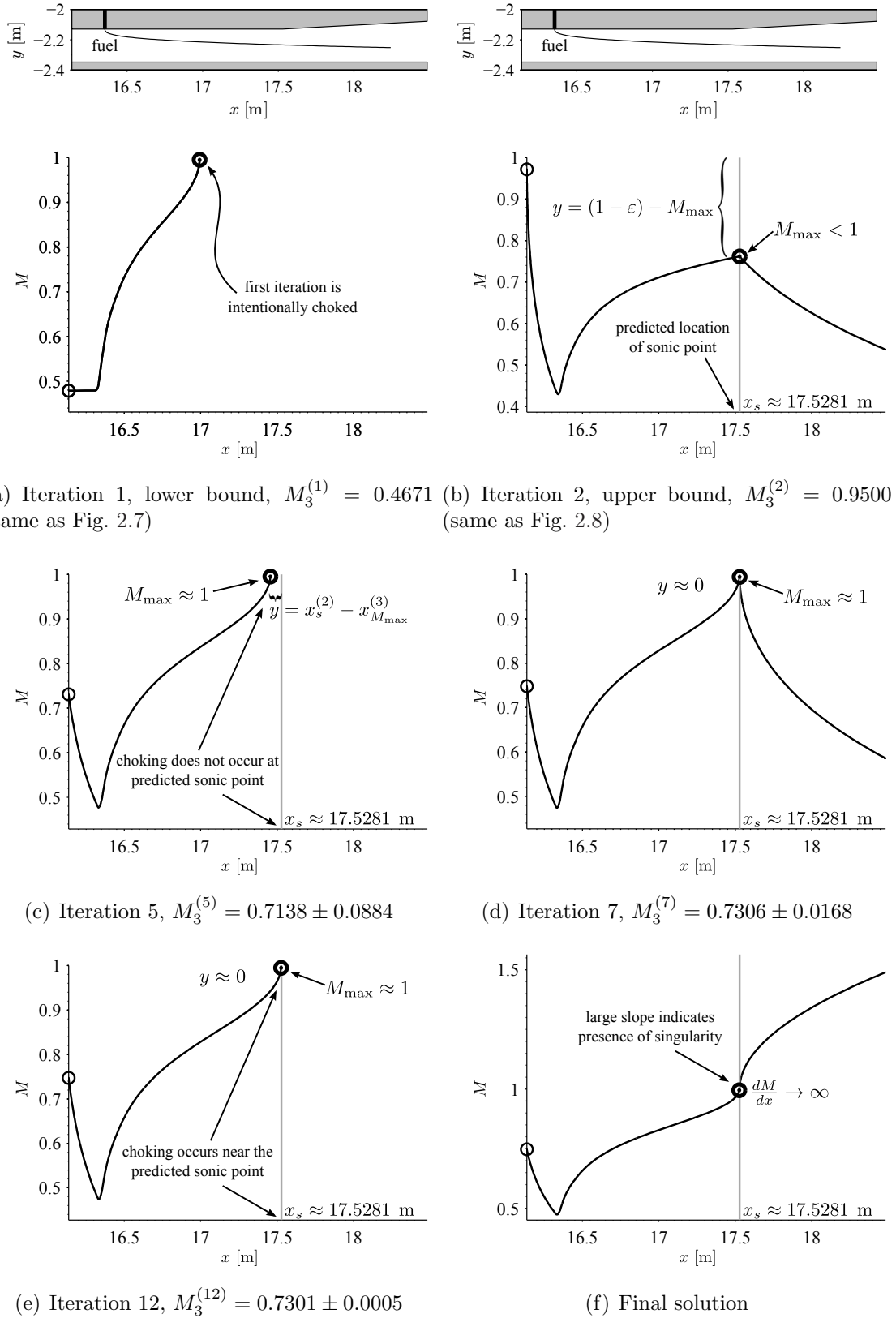
Figure 2.10: Mach number profiles computed during iterations of the shooting method. Circles at the left-hand boundaries of the plots show initial guesses of M_{3a}. Note that the x-coordinate begins at the nose of the vehicle.

CHAPTER 3

Design and Optimization

Different authors use slightly different terminologies when speaking of the components of a vehicle co-optimization problem. As defined by Peters [21], a co-design problem is one in which both a controlled system and a controller are to be optimized. The principle goal of this section of the work has been to develop a method to easily allow optimization of vehicle or trajectory separately, or co-optimization of vehicle and trajectory simultaneously. For the sake of clarity, the terminology used here divides the general vehicle co-design problem into 4 components: *mission*, *vehicle*, *trajectory*, and *control*.

In this work, "mission" means the vehicle states that are required to be satisfied for the vehicle to be considered a success. For example, starting at Detroit (DTW) and ending at Phoenix (PHX) less than 12 hours later would be a mission definition. Another example of a mission would be to deliver a payload of a given mass to a 51.6° orbital inclination at an altitude of 330km (to the International Space Station (ISS)). A vehicle is always designed for a specific set of missions. The mission considered in this section is to travel from $M = 7$ to $M = 13$. Details of this mission are given in section 3.1.1.

The "vehicle" or "vehicle design" represents a list of parameters describing the design states that are fixed throughout the duration of the mission. In other words, the vehicle represents the design variables that are not actively controlled and do not morph as the vehicle flies. This is what people sometimes refer to as the design or the artifact.

The "trajectory" represents a list of states of the vehicle, specified at points in time, that the vehicle achieves while in flight. These states are often fixed ahead of time in order to constrain the vehicle to follow some given trajectory [19, 20, 16] but could in principle vary in flight, for example if the equations of motion were directly integrated in order to confirm performance of a stabilizing controller. Trajectory

states are any states of the vehicle which are capable of varying during flight (such as flight Mach number, M_∞ and altitude, h). It is often convenient, however, to neglect states that are not of interest to a particular trajectory, although in practice these states must be either open-loop stable or stabilized using control if they have any effect on the overall stability of the vehicle. As will be seen below, it is convenient to assign certain states of the vehicle (such as angle of attack) to be "floating" in order to give full authority to the trim routine.

The "control" is the list of state variables that are able to vary in flight and are also under direct (or nearly direct) control of the operator. Usually control is used to ensure that the specified trajectory states are indeed satisfied at certain points in time. Although it is possible to specify certain control states in the trajectory, this is often an unnecessary and restrictive constraint. An example of this would be the specification of when in the trajectory landing gear must be extended or retracted, since this (despite being a control variable) has an effect on the performance of the airplane, and should be left to the control of the optimization routine if at all possible.

These distinctions can appear arbitrary, but in practice they provide useful distinctions between the myriad variables of a large-scale analysis and a way to divide up different parts of the optimization.

Design for airplanes in general and hypersonic vehicles in particular has typically focused on what could be called "multi-point" methods. This means that the design is analyzed at a few points that have been determined to be key points, and off-design performance, which is performance between the design points that were originally considered, is essentially unknown until the design has been fleshed-out and high-fidelity simulation tools can be brought to bear. Trajectory-based optimization, in contrast, allows for rigorous calculation of performance across the range of conditions the vehicle may be expected to encounter in flight. However, most previous efforts have followed upon the work of Bryson, for example, Hedrick and Bryson [70] and Bowcutt [13]. These approaches give good insight into the governing requirements of the vehicle in terms of engineering parameters, but the they are necessarily limited in their ability to predict physical behaviors that lead to most control problems, since in many cases it is precisely the existence of strong nonlinearities that causes failure, and simple performance models do not respect these nonlinearities. Examples of methods that do examine nonlinear performance are Bowcutt [16] and Koko [19]. These methods have promise because they have the potential to capture effects such as engine failure if the underlying models predict those effects. The approach used here is similar to that of [16] and [19], except that I have used the underlying model

(MASIV) directly, and not used a response-surface or other type of surrogate. This adds difficulty to the optimization procedure and to the control performance evaluation, but it does allow for all engine behaviors predicted by the model to be involved in the trajectory and control simulations.

The method used in this section is a collocation method that uses Hermite interpolation and Simpson quadrature. Although this type of method has been used on many problems, it has rarely, if ever, been applied to HSVs. Aerospace literature on the subject of optimal trajectory methods with realistic component analysis routines that have accuracy limitations is scarce. Most authors either use models that are unrealistic, but easy to use with an optimizer, or high-fidelity methods that generate performance table. Trajectory optimization with the MASIV model is subject to accuracy limitations, but offers the benefit of being less expensive than surrogate models for large numbers of variables. It allows the trim conditions to be appropriately applied at each point in the trajectory (instead of just at the table points), as shown in section 3.1.4, and allows for exploration of the neighborhood of the solution to identify possible problems, as will be seen later in section 4.3.

3.1 Trajectory optimization

The space-access trajectory presented here represents the 2nd stage of a three-stage to orbit vehicle. For this concept, the first stage would be a rocket-propelled vehicle capable of lifting the HSV to the required speed and altitude. The second stage would be the scramjet, and the third stage would be another rocket. This implies a certain starting point (basically a lower limit for operability of the scram-mode) and stopping point (basically an upper limit for operability of the scram-mode). This study ignores the various other components required to actually achieve this trajectory (such as lifting the vehicle to the initial Mach number and altitude) and concentrates on how a trajectory may be optimized for a fixed vehicle.

A trajectory defined by initial and final Mach numbers and constant dynamic pressure was chosen for convenience of parametrization. A similar trajectory has been used previously [71] because control surface effectiveness and overall lift are assumed to be well-behaved on a constant dynamic pressure trajectory. This trajectory was optimized to give minimum fuel consumption for the vehicle described above, in section 1.1.

To optimize the trajectory, first the vehicle had to be defined. Recent air and ground tests have concentrated on fixed flowpaths, [10, 11], so the possible impli-

cations of internal flowpath control systems and other types of variable geometry (such as variable inlets, cowls or nozzles) are ignored. Of course, range of operability and overall engine performance can likely be improved by using variable geometry so there is some tradeoff between complexity, weight, and development cost of an actuated engine and a static one [72].

The combustor geometry chosen was based on a scaled-up version of previous laboratory-scale designs available in the literature [7, 44, 51, 73]. It is important to note that the combustors used as a starting point for this optimization are laboratory combustors that were not specifically designed to produce high thrust or efficient operation. However, they do provide a reasonable place to start, since they are known to be operable, and Micka's [44] has provided data used validate the model before using it in the optimization study.

The flowpath and vehicle used in the optimization (with similar properties to X-43) are shown in Fig. 3.1 and Fig. 3.2 for reference. The list of parameters that defines this vehicle is shown in section B. This vehicle is known as the MAX-1.
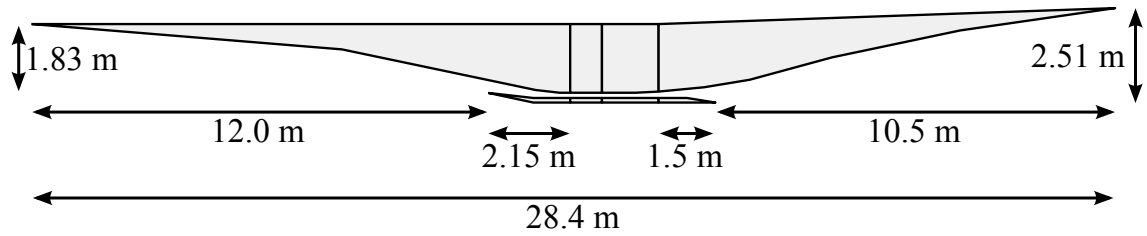
Figure 3.1: The MAX-1 flowpath design.
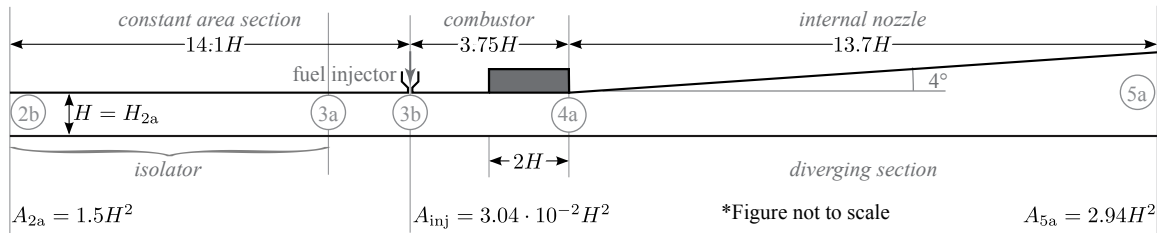
Figure 3.2: The MAX-1 combustor configuration, based on 2.6.

Several previous attempts have been made to define useful trajectories for design of airplanes. Although the literature on trajectory simulation and optimization is large, only those methods of interest for co-optimization and design of vehicles are discussed here.

One of the most complete systems for analyzing vehicle performance over ranges of conditions for jet airplanes is the System for assessing Aviation's Global Emissions

(SAGE) [20]. This report has some significant details regarding practical considerations of simulating airplane flights. They represented flights as a series of nodes, and indicated that flight nodes are considered redundant if they satisfy all of the following criteria (p.23):

1. No change in air traffic control (ATC) center

2. No change in altitude type

3. No horizontal deviation of more than 2 nm

4. No altitude deviation of more than 1000 ft (305 m)

5. No speed deviation of more than 20 kts ($10.3 \frac{m}{s}$).

They also model takeoff gross weight (TOGW) using weights associated with stage lengths (empirical). Aircraft performance data were tabulated using information from an extremely large number of records of actual flights. So, this could be described as a semi-empirical approach. This study did simulate vehicle trajectories using tabular information, but it is not suitable for predictive algorithms based on new geometries, since actual performance of existing geometries must be known for a tabular approach to work. The tabular approach is also not appropriate for analyzing trajectories of hypothetical vehicles because many of the segments of the trajectories considered in SAGE, as well as requirements on the airplanes involved, are due to Federal Aviation Administration (FAA) regulations. Also, the SAGE approach relied on assumed trajectories, without any notion of control; this is acceptable for known platforms that are well-characterized.

For the case of co-optimization and design of a vehicle and trajectory simultaneously, it is necessary to select an approach that allows more freedom in the trajectory selection. However, the guidelines above do give some indication of how closely trajectory points might be spaced in realistic simulations. For an accelerating trajectory, it would not be appropriate to require such a small speed deviation as used in SAGE study. The step sizes used below (section 3.1.7) represent deviations of 286 m to 504 m between successive points, only a slightly larger range of altitude steps than SAGE used. However, due to the large acceleration, the velocity varies by $80 - 86 m/s$ between nodes over the trajectory. Due to the large velocity, the position changes by $44 - 109 km$ between nodes over the trajectory.

3.1.1 Trajectory Definition

A trajectory will be defined as a series of node points at which time, state variables, and control variables are prescribed [74, 75]. In general, the vehicle state, $\mathbf{x}$, consists of position and velocity vectors and vehicle orientation:

$$\mathbf{x} = \begin{bmatrix} L & \lambda & h & M & \gamma & \sigma & \alpha & \beta & \phi & P & Q & R \end{bmatrix}^T \tag{3.1}$$

The position state, $\mathbf{r}$, is defined by longitude, L, latitude, λ, and altitude, h and the velocity state, $\mathbf{v}$, is defined by Mach number, M, flight path angle, γ, and heading angle, σ. The vehicle orientation is defined by angle of attack, α, sideslip angle, β and roll angle, ϕ, and the corresponding angular velocities, P, Q, and R. The choice of longitude, latitude, and altitude is convenient for very high speed airplanes where Coriolis effects and the curvature of the earth are significant. Also, this selection is consistent with space access trajectory analysis.

For trajectory purposes, we are not particularly interested in the vehicle orientation, only the vehicle's position and velocity. The vehicle orientation states are left as free parameters, which supplies extra degrees of freedom during computation of the trim state. The "trajectory state" consists of those states of the vehicle which are of interest:

$$\boldsymbol{\xi} = \begin{bmatrix} L & \lambda & h & M & \gamma & \sigma \end{bmatrix}^T \tag{3.2}$$

For general trajectories, it is also possible to eliminate latitude by specifying that the vehicle flies directly east from the equator. Then, longitude is equivalent to distance east from the starting point. This leaves only

$$\boldsymbol{\xi} = \begin{bmatrix} L & h & M & \gamma \end{bmatrix}^T \tag{3.3}$$

however, for a constant dynamic pressure trajectory, $L = L(M, t)$ and $\gamma = \gamma(\frac{dh}{dt}, M)$, leaving trajectories defined by only altitude and Mach number in the simplest cases. Of course, for trajectories not beginning at the equator or including variations in latitude, it is necessary to retain all variables of (3.2). It is also possible to specify other desired vehicle states of (3.1) at each node, but these added constraints add to the difficulty encountered in trimming the vehicle at each step.

Each node of the trajectory also has an associated control state:

$$\mathbf{u} = \begin{bmatrix} \delta_{ER} & \delta_{CE} & \delta_{DE} & \delta_{CR} \end{bmatrix}^T \tag{3.4}$$

The control state variables are fuel equivalence ratio δ_{ER}, common elevator deflection δ_{CE}, defined as the average of the left and right elevator deflection angles, differential elevator deflection δ_{DE}, defined as the deflection angle of the right elevator minus the deflection angle of the left elevator, and common rudder deflection δ_{CR}. The rudders are not allowed to be deflected differentially. If only longitudinal dynamics are considered (and not turning performance), this simplifies to

$$\mathbf{u} = \begin{bmatrix} \delta_{ER} & \delta_{CE} \end{bmatrix}^T \tag{3.5}$$

The trajectory and control consist of N arcs, and time t is the independent variable in each leg, $t_{0,i} \leq t \leq t_{f,i}$ for nodes $i = 0, \ldots, N$ such that the trajectory state and control state are, [74]

$$\boldsymbol{\xi} = \boldsymbol{\xi}(t) \qquad \mathbf{u} = \mathbf{u}(t) \tag{3.6}$$

Of course, the vehicle parameters $\mathbf{p}$ are also incorporated into the dynamics, so the final equations of motion for the nonlinear vehicle system are [36]

$$\mathbf{y} = \begin{bmatrix} \dot{M} & \dot{\gamma} & \dot{\sigma} & \dot{P} & \dot{Q} & \dot{R} \end{bmatrix} = \mathbf{F}(\mathbf{x}, \mathbf{u}, \mathbf{p}) \tag{3.7}$$

where the black-box function for the vehicle dynamics, $\mathbf{F}$, is given by the vehicle analysis code (MASTrim, in our case).

It is of interest to note that although most of the vehicle parameters are not functions of time, some of them (e.g., mass or mass distribution, material temperature and properties) may be, and this model allows for such possibilities [19].

Equation (3.7) is the nonlinear equation of motion for the vehicle. The quantities in (3.7) that make up the given state derivative, $\mathbf{y}$, are not the only quantities that could be selected [36]. However, representing the state in terms of Mach number, flight path angle and heading angle makes sense from a navigation point of view.

3.1.2 Trajectory Generation

Although the trajectory state derivatives ($\dot{\mathbf{x}}$) can be included as decision variables in the optimization, this approach requires two decision variables for each trajectory

state. Instead, we used the trajectory state values at the nodes to approximate the required derivative for each trajectory state using the second-order finite difference equation for nonuniform step sizes [76]:

$$\Delta t_i = t_i - t_{i-1} \tag{3.8}$$

$$\frac{d\boldsymbol{\xi}_i}{dt} = \frac{1}{\Delta t_i + \Delta t_{i+1}} \left(\frac{\Delta t_i}{\Delta t_{i+1}} \Delta \boldsymbol{\xi}_{i+1} + \frac{\Delta t_{i+1}}{\Delta t_i} \Delta \boldsymbol{\xi}_i \right) \tag{3.9}$$

Although this approximation adds a constraint, it reduces the number of decision variables by one per node, since the constraint is identically satisfied due to the collocation procedure. This equation limits the change in acceleration that can be applied at each node, but in practice this seems to be consistent with physical restrictions on the accelerations in adjacent legs of the trajectory.

Trajectories were constrained to have constant dynamic pressure, which implies that $h_i = h(M_{\infty,i})$. The 1976 standard atmosphere [38] was used to perform this lookup. This additional constraint again reduces the number of variables involved in the problem so that general principles governing trajectories for this vehicle may be explored. This trajectory study is therefore confined to a single trajectory family. Using the trajectory nomenclature of Dalle et.al., [36], a trajectory was computed which traverses Mach numbers along constant dynamic pressure lines by selecting appropriate altitudes and flight path angles:

$$W^n = \frac{dh}{dt} \tag{3.10}$$

$$\frac{dL}{dt} = U^n \tag{3.11}$$

$$U^n = U \cos \gamma - W \sin \gamma \tag{3.12}$$

$$\tan \gamma = \frac{W^n}{U^n} \tag{3.13}$$

Here, $\mathbf{v}^n = \begin{bmatrix} U^n & V^n & W^n \end{bmatrix}$ are the velocity components in the navigation frame and $\mathbf{v}^b = \begin{bmatrix} U & V & W \end{bmatrix}$ are the velocity components in the body frame. In order to completely define the trajectory, at each node some reasonable acceleration of the vehicle is required. This links the rate of change of altitude, $\frac{dh}{dt}$ to the acceleration, $\frac{d\mathbf{v}^b}{dt} = \dot{\mathbf{v}}$.

A simple manipulation yields

$$\frac{U \cos \gamma \sin \gamma - W \sin^2 \gamma}{U \cos \gamma} = \frac{\dot{\mathbf{v}}}{a\|\mathbf{v}\|}\frac{dh}{dM} \tag{3.14}$$

the first approximation of which is

$$\sin \gamma = \frac{\dot{\mathbf{v}}}{a\|\mathbf{v}\|}\frac{dh}{dM} \tag{3.15}$$

This calculation allows a trajectory to be parametrized by starting and ending Mach numbers, M_0 and M_f, a constant dynamic pressure, q, and desired total acceleration, $\dot{\mathbf{v}}_i$. The example above describes a very simple case. For a more detailed description of the procedure see [4].

Finally, the trajectory is implemented as a static list of nodes in (M, h). Although the total acceleration could be specified directly at each node in terms of $\dot{M}$ and $\dot{h}$, this produces a somewhat awkward implementation in terms of the independent variable, t_i. To avoid these consistency issues it is more convenient to define the decision variables to be $t_i, i = 1, \ldots, N$. Then, the length of each interval, Δt_i, uniquely determines $\dot{\mathbf{v}}_i$, which specifies the rates of change of the trajectory states, $(\dot{M}, \dot{h})$, as above. The next section describes how to determine the required control states at each node that satisfy the given trajectory states and trajectory state derivatives.

Perhaps the most important requirement, however, is that of parallelization to multiple processors. This formulation gives a constant number of trajectory nodes, which results in a very efficient use of processors. In the formulation described here, it is possible to assign each trim sub-problem to a separate processor, meaning that the time required to simulate the trajectory is always the time required to solve the trim problem that takes the longest to complete [77]. Since all the trim cases are similar, this means that with a large number of processors, a large number of trajectory nodes may be considered.

3.1.3 Performance Estimation

For each optimization step, the fuel cost to traverse the trajectory must be computed. In order to compute the performance of the vehicle along each trajectory arc, the Hermite-cubic interpolation with Simpson quadrature method was employed [18].

In order to exclude controller design and performance from the simulations only quasi-steady solutions to the equations of motion are considered. This means that at each node point the vehicle must be trimmed, that is, $\mathbf{u}$ is chosen such that $\mathbf{y}$ takes on

the specified value. This allows the remaining, unspecified vehicle and control states to be determined.

3.1.4 Trim procedure

The trim procedure solves a sub-problem of optimizing the control settings to achieve the desired states derivatives at each node and control point. In the generic case, the problem to be solved is

$$
\begin{aligned}
\text{minimize} \quad & \mathbf{F}(\mathbf{x}, \mathbf{u}, \mathbf{p}) && (3.16) \\
\text{w.r.t.} \quad & \mathbf{u} && \\
\text{subject to} \quad & \mathbf{x}, \mathbf{p} && (3.17)
\end{aligned}
$$

such that the vehicle undergoes no acceleration. However, for a non-cruise (accelerating) trajectory, the trim condition is

$$
\mathbf{y}_i = \begin{bmatrix} \dot{M}_i & \dot{\gamma}_i & \dot{\sigma}_i & \dot{P}_i & \dot{Q}_i & \dot{R}_i \end{bmatrix} \tag{3.18}
$$

with $\mathbf{y}_i \neq \mathbf{0}$. In this case, since turning performance is not considered, $\dot{\sigma}_i = \dot{P}_i = \dot{R}_i = 0$. Given some target values, the trim routine uses Broyden's method to reduce the difference from the desired value to below 10^{-5} for angular accelerations and below $5 \cdot 10^{-5}$ for linear accelerations. Thus the required trajectory state and state derivative can be met at each node. It should be pointed out here that the truncation error in this step has an effect on the overall error accumulated in computing the trajectory cost.

3.1.5 Collocation method

The trajectory simulation method used here was originally described by Hargraves and Paris [18]. They present a collocation method based on the work of Dickmanns and Well [78], called the "Hermite-Simpson" method. They suggest the (well-known) Hermite-cubic interpolation for the evolution of the vehicle states on each interval $t_{i-1} \leq t \leq t_i$:

$$
\boldsymbol{\xi}_{i-\frac{1}{2}} = \frac{1}{2}(\boldsymbol{\xi}_{i-1} + \boldsymbol{\xi}_i) + \frac{\Delta t_i}{8} \left[\mathbf{F}(\boldsymbol{\xi}_{i-1}, \mathbf{u}_{i-1}) - \mathbf{F}(\boldsymbol{\xi}_i, \mathbf{u}_i) \right] \tag{3.19}
$$

Equation (3.19) approximates the trajectory state $\boldsymbol{\xi}_{i-\frac{1}{2}}$ between two known tra-

jectory states ($\boldsymbol{\xi}_{i-1}$ and $\boldsymbol{\xi}_i$), using the known acceleration resultants $\dot{\boldsymbol{\xi}} = \mathbf{y} = \mathbf{F}$ at those states.

Next, Simpson's quadrature is employed to obtain an equation linking states $i-1$ and i through the approximated state $i - \frac{1}{2}$:

$$\Delta\boldsymbol{\xi} = \boldsymbol{\xi}_{i-1} - \boldsymbol{\xi}_i + \frac{\Delta t_i}{6}\left[\mathbf{F}(\boldsymbol{\xi}_{i-1}, \mathbf{u}_{i-1}) + 4\mathbf{F}(\boldsymbol{\xi}_{i-\frac{1}{2}}, \mathbf{u}_{i-\frac{1}{2}}) + \mathbf{F}(\boldsymbol{\xi}_i, \mathbf{u}_i)\right] \qquad (3.20)$$

The defect, $\Delta\boldsymbol{\xi}$, between states $i-1$ and i is constrained to be $\mathbf{0}$. Thus, (3.20) can be re-written to give an equation for the required state derivative at the midpoint of the arc between nodes $i-1$ and i:

$$\mathbf{y}_{i-\frac{1}{2}} = \frac{3}{2\Delta t_i}\left(\boldsymbol{\xi}_i - \boldsymbol{\xi}_{i-1}\right) - \frac{1}{4}\left[\mathbf{F}(\boldsymbol{\xi}_i, \mathbf{u}_i) + \mathbf{F}(\boldsymbol{\xi}_{i-1}, \mathbf{u}_{i-1})\right] \qquad (3.21)$$

The computed state derivative $\mathbf{y}_{i-\frac{1}{2}}$ is then used as an input to the trim calculation, which in turn gives the necessary control input $\mathbf{u}_{i-\frac{1}{2}}$ required for the vehicle to achieve the next trajectory point, $\boldsymbol{\xi}_i$

$$\mathbf{F}(\boldsymbol{\xi}_{i-\frac{1}{2}}, \mathbf{u}_{i-\frac{1}{2}}) = \mathbf{y}_{i-\frac{1}{2}} \qquad (3.22)$$

and $\mathbf{u}_{i-\frac{1}{2}}$ is found using (3.16).

The quadrature method is used to assure that the control input chosen at the middle of the interval $(i - \frac{1}{2})$ is such that it will cause the trajectory state boundary condition at the left- and right-hand conditions to be met (known as a two-point boundary-value problem (TPBVP) [79]), ensuring that the trajectory is followed at each given node point. Not integrating the dynamic equations directly frees us from considering the dynamic control problem, but nevertheless allows us to construct and follow trajectories given the assumption that the vehicle performance is relatively well-behaved on each interval and that it is possible to generate a controller to achieve closed-loop dynamic stability everywhere.

Finally, the fuel consumption over the entire trajectory is found by integrating the fuel mass flow rate, $\dot{m}_{\text{fuel}}$, which is known at each node and half-node because it is a function of δ_{ER}, a component of the vehicle control state $\mathbf{u}$. A trapezoidal method is adequate if the values at nodes and half-nodes are used.

This method requires that the trajectory be defined in advance, as described above in section 3.1.2. In principle the trajectory need not be defined continuously; it could simply be a series of nodes. Of course, the interpolation procedure used on each interval still determines the basis function that joins the starting and ending point of

each leg of the trajectory, but the piecewise continuous nature of this model allows for multiple-phase trajectories involving discontinuities at collocation points to be computed [74]. One reason this is advantageous is that the trajectory itself can be optimized external to the performance calculation routine, with the result being a sequence of nodes.

The general procedure for computing vehicle performance along a given quasi-steady trajectory is the following:

1. Begin with given trajectory $\boldsymbol{\xi} \in [\boldsymbol{\xi}_0, \ldots \boldsymbol{\xi}_i, \ldots, \boldsymbol{\xi}_n]$, $n = $ number of trajectory arcs.

2. Compute required trim condition at each trajectory node, $\mathbf{y}_i = \mathbf{F}(\boldsymbol{\xi}_i, \mathbf{u}_i)$, giving $\mathbf{u}_i$

3. Interpolate to find midpoint states $(\boldsymbol{\xi}_{i-\frac{1}{2}})$ using (3.19)

4. Use Simpson quadrature (3.21) to determine required acceleration at midpoints, $\mathbf{y}_{i-\frac{1}{2}}$

5. Compute trim condition at midpoints to determine required control input $\mathbf{u}_{i-\frac{1}{2}}$ to achieve $\boldsymbol{\xi}_i$ beginning from $\boldsymbol{\xi}_{i-1}$ by satisfying $\mathbf{y}_{i-\frac{1}{2}} = \mathbf{F}(\boldsymbol{\xi}_{i-\frac{1}{2}}, \mathbf{u}_{i-\frac{1}{2}})$

6. Approximate vehicle performance metric Δm_{fuel} by integrating $\dot{m}_{\text{fuel}}(\delta_{ER})$

3.1.6   Parametrization

The selection of number of decision variables in the trajectory is influenced by the type of trajectory simulation chosen. This is especially important in our case, because it is very computationally expensive to compute the fuel cost along the trajectory, compared to the computational cost of the simple models often used in trajectory simulation [16, 18, 78]. In our present implementation, the trajectory state and trajectory state derivative constraints are satisfied at each point by identically specifying the state variables as a flight condition, and then using the trajectory state derivatives as target values for the trim procedure. The trim procedure, as described above in section 3.1.4, is an optimization subproblem within the overall optimal control problem. This adds a sub-step to the optimization, since in principle the control state at each node and at control point could be included in the optimal control problem. Instead, we use the trajectory state derivatives as control variables, and trim the vehicle using those state derivatives as targets for each node and control point.

3.1.7 Optimization

The actual trajectory optimization problem solved was

$$\text{minimize} \qquad \Delta m_{\text{fuel}} = \int_{t_0}^{t_f} \dot{m}_{\text{fuel}}(\tau, x)\, d\tau \qquad\qquad (3.23)$$

$$\text{w.r.t.} \qquad \begin{bmatrix} \Delta t_1 & \dots & \Delta t_{11} \end{bmatrix}$$

$$\text{subject to} \qquad 0.1\,\text{m/s}^2 < \dot{\mathbf{v}}(\Delta t_i) < 4\,\text{m/s}^2 \qquad\qquad (3.24)$$

which allows parallelization to 12 processors, since 12 trajectory nodes are used. This gives 22 total acceleration intervals, since there is one control node at the center of each interval, and the final trajectory comprises 23 nodes (including control points). The outer optimizer directly controls the sizes of the 11 Δt_i intervals, and the trim optimization sub-problem implies 3 control variables at each trajectory node and control node,

$$\text{minimize} \qquad \left| \dot{\boldsymbol{\xi}}_i - \mathbf{y}_i \right| = \mathbf{F}(\mathbf{x}, \mathbf{u}, \mathbf{p}) \qquad\qquad (3.25)$$

$$\text{w.r.t.} \qquad \mathbf{u} \qquad\qquad\qquad = \begin{bmatrix} \delta_{ER} & \delta_{CE} & \alpha \end{bmatrix}^T$$

$$\text{subject to} \qquad \mathbf{x}, \mathbf{p} \qquad\qquad\qquad (3.26)$$

where the angle of attack, α is used as a dependent variable for the purposes of determining control. This results in 69 decision variables to account for all the trim points (both trajectory nodes and control nodes) and 11 decision variables to account for the trajectory nodes, for 80 total variables in the optimization. At each evaluation point the optimizer chooses, the vehicle is "flown" through a trajectory defined as in section 3.1.3, using the current trajectory design parameters.

The cases were run on the "Flux" cluster at the Center for Advanced Computing (CAC) at the College of Engineering of the University of Michigan. The computers used have Intel Xeon processors running at 2.67 GHz, and 3 GB of memory was used for each processor. Details of run times and initial conditions are discussed below, under section 5.3. MATLAB's `fmincon` routine was employed.

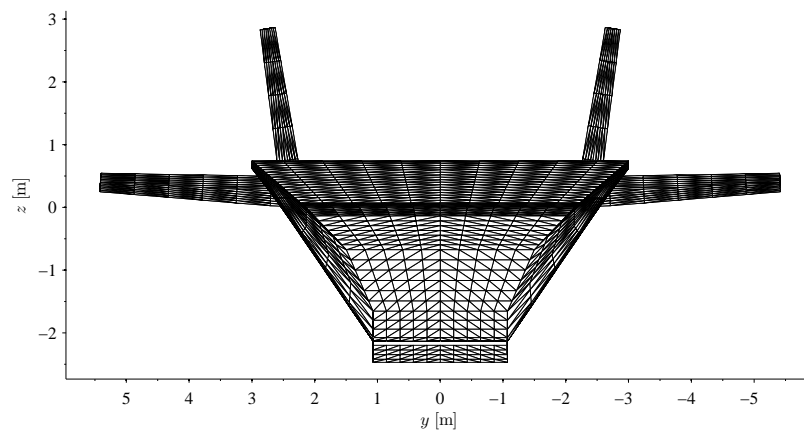The scram-only section of the trajectory was defined from $7 < M < 13$, $24.0\text{km} < h < 32.3\text{km}$, with $q = 101325\,\text{Pa}$. The path of the vehicle on this trajectory is shown in Fig 3.4. Note that the axes are Mach number and altitude, so angles should not be interpreted as flight path angle or angle of attack.
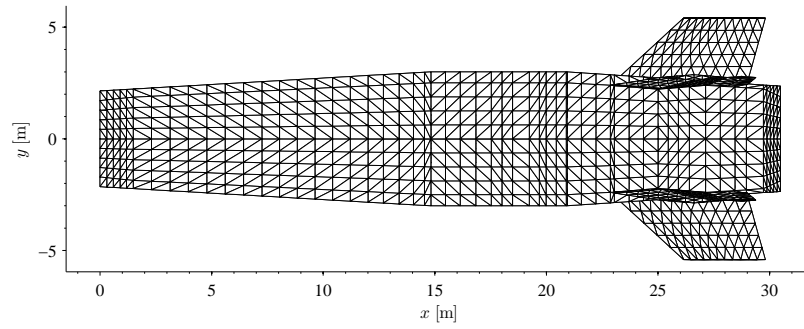
(a) top view
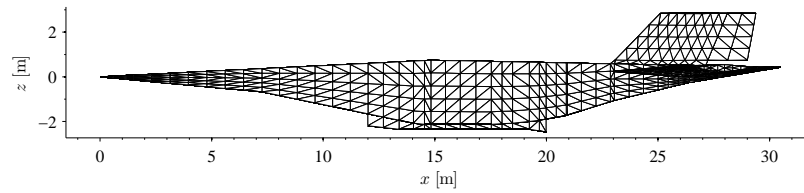
(b) side view

(c) front view

Figure 3.3: The MAX-1 exterior views.

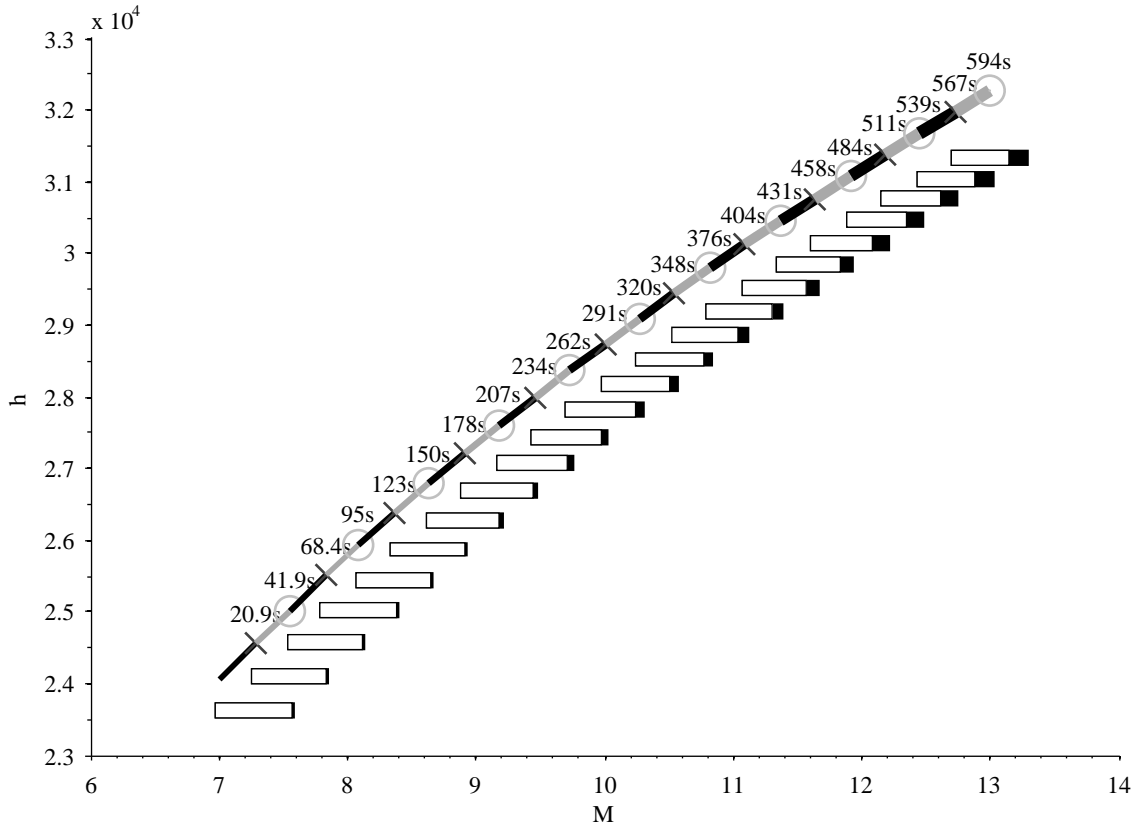Figure 3.4: Scram-mode-only trajectory path through $M - h$ space, with h in m. The rectangular bars show fuel consumed compared to overall fuel (22700kg in this case) and the elapsed time is printed above each node. Points marked with circles are trajectory nodes, (i); points marked with x's are trajectory arc midpoints, $(i - \frac{1}{2})$. The line thickness is proportional to the fuel flow rate.

CHAPTER 4

Validation

One main problem that is frequently encountered when validating hypersonic vehicle models is that there have been exceedingly few vehicle flight tests. Therefore, the models used here were validated against ground-test experiments of a direct-connect windtunnel combustor at the University of Michigan [80]. Quantitative flight test data for the X-43A and X-51 have not yet been released, so although those vehicles would provide extremely valuable data with which to compare our models, such a comparison may not yet be made.

Compounding the issue is the fact that experiments that otherwise might be suitable comparisons for our code very frequently do not have sufficient information to allow a true comparison to be made. For example, many experiments that measure thrust of an engine do not have detailed enough information about run conditions and geometry to be of any use [7, 65, 81]. Experiments that do have detailed information about thermodynamic variables often do not have measurements of thrust [44, 45, 82]. Finally, there are numerous experiments that measure small-scale flow properties, but not whole-flowpath engineering performance metrics. These are only useful to verify the performance of the sub-scale models in section 2.2, and not for general comparison because we do not compute detailed flowpath properties such as vorticity at injectors and other 3-D flow patterns.

Part of this difference can be chalked up to industrially-biased versus academically biased tests. However, the lack of serious standards in experimental and computational results reporting is a known issue [83], and I would like to call attention to the point that results, even those of well-designed experiments, are almost useless if insufficient information is provided with which to reproduce the test. It was possible to obtain a great deal of information about the University of Michigan Dual-Mode Ramjet [45] experiment, because this facility operates side-by-side with our computational group. Therefore, this is the experiment used for the validation cases presented below (an approach suggested by Oberkampf and Trucano [83]).

4.1 Combustor

Two separate tests were conducted to validate the MASIV combustor model. We compared the code's performance for prediction of mixing and combustion in the duct to the experimental measurements made with optical techniques and to high-fidelity CFD solutions of the same configuration. In these tests, the figures of merit were the location, size, and shape of the predicted reacting region of the duct, as well as the total predicted heat release. We chose this approach because the three different results offer different insights and different levels of accuracy into the different parts of the flow. Not all quantities can be measured in the experiment, so although it is treated as the truth model not all variables of interest can be surveyed.

The commercial code Fluent [84] was used for CFD comparison, both to compare two completely different computational methods and to gain some insight into the internal thermodynamic flow states, not all of which are available from experimental measurements. The CFD model provides detailed information about all flow variables at all locations in the flow, but because modeling of turbulence and chemistry is required, it does not agree perfectly with the measurements. Finally, the 1-D model can provide the most basic types of insights into conservation, jet mixing, and chemistry results in the duct, but it does not agree perfectly with the measurements and does not provide any information at very fine scales. Differences between the methods are discussed below. We have attempted to match the simulations to the experimental results without tuning the models to the extent that their applicability to other problems is compromised.

4.1.1 Experiment

Supersonic combustion experiments were performed in a dual-mode ramjet/scramjet combustor [44]. This facility supplies 21% O_2 mole fraction vitiated air at stagnation temperatures (T_0) up to 1500 K. The test section is made of stainless steel and is shown in Figure 1. A two-dimensional Mach 2.2 nozzle exits into a constant area isolator with a cross section of 25.4 mm by 38.1 mm. The constant-area isolator is followed by a wall cavity flameholder and a nozzle section with a 4 degree divergence angle. Room temperature gaseous fuel was injected sonically through a single 2.49 mm diameter port located on the test section centerline 44.5 mm upstream of the cavity leading edge. Additional details on the facility and test section are available from Micka and Driscoll [64].

There are wall static pressure ports at 16 locations throughout the combustor and
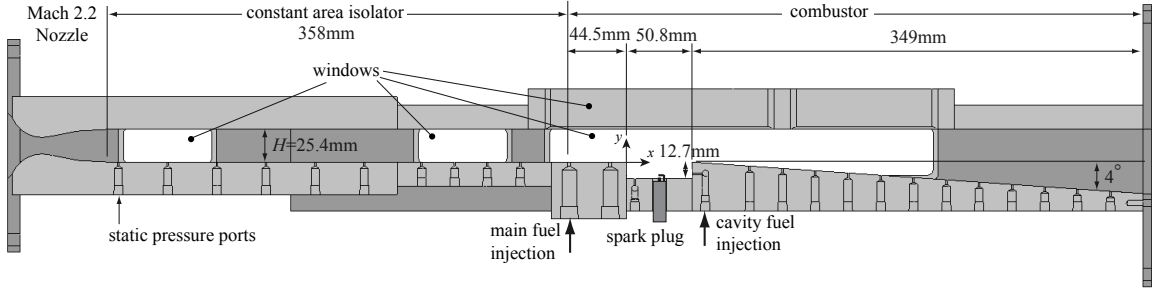
Figure 4.1: Dual-mode combustor.

isolator. Estimates of the heat release distribution in the combustor were acquired using images of the OH* luminosity [64]. Chemiluminescence is often used as a marker of the heat release in flames, and OH* is proportional to the heat release rate in many cases [85]. The luminosity from OH* was imaged using a Andor Istar intensified camera with a 310 ± 10 nm bandpass interference filter.

Table 4.1: Conditions at station 2a for experiment, Fluent and MASIV, with overall equivalence ratio $\phi = 0.27$.

	T_0	p_0	T	p	u	composition
vitiated air cross-flow	1370K	333kPa	1280K	261kPa	458m/s	$Y_{O_2} = 0.251$ $Y_{N_2} = 0.611$ $Y_{H_2O} = 0.138$
fuel jet	298K	829kPa	248K	438kPa	1200m/s	$Y_{H_2} = 1$

4.1.2 CFD Simulations

The Fluent boundary conditions are based on stagnation conditions in the air and fuel streams. Because of this, there is a discrepancy between the boundary conditions for Fluent and MASIV, which corresponds to the difference between Fluent's predictions of friction (and hence isolator performance) in the duct and the 1-D estimate of conditions from the experiment based on Heiser and Pratt's [5] isolator performance relationships.

The Fluent CFD geometry is identical to that of the dual-mode combustor experiment described in the previous section. The meshed region includes the combustion and diverging-area sections of the experimental apparatus only, including only as much of the isolator section as required to contain the flow stagnation point upstream of the fuel injection port, and to allow for fuel diffusion upstream of the injector. The mesh is more densely clustered near the fuel injector to capture the physics of the

fuel-air mixing as accurately as possible. The mesh also is denser near the leading and trailing edges of the stabilization cavity to capture their influence on the down-stream thermal choke point created by heat addition to the subsonic flow. Symmetry about the vertical center plane allows us to reduce the computational requirement so that there are approximately 400,000 tetrahedral finite elements for half the combustor.

The pressure-based solver in Fluent was used, which solves the steady second-order upstream equations including viscosity and the energy equation; turbulence is modeled using the realizable k-ϵ model with standard wall functions. The mixture fraction and scalar dissipation rate are assumed to be statistically independent in the Fluent implementation, so the joint PDF $\tilde{P}(f, \chi_{\mathrm{st}})$ is set equal to $\tilde{P}(f)P(\chi_{\mathrm{st}})$. The PDF of the mixture fraction is assumed to be a beta-function. Fluctuations in the scalar dissipation rate are ignored so the PDF of χ becomes a delta function: $P = \delta(\chi_{st} - \widetilde{\chi_{st}})$. The mean scalar dissipation rate is modeled as $\widetilde{\chi}_{\mathrm{st}} = 2\frac{\varepsilon}{k}\widetilde{f'^2}$ where $\overline{f'^2}$ is the mean mixture fraction variance [43]. Real-gas models are included to describe the compressible behavior of each of the species contained in the mixture. We used the non-premixed, diabatic steady flamelet model including compressibility effects. A standard CHEMKIN [86] mechanism for H_2-Air combustion dictates the chemistry and H, O, OH, H_2O, H_2O_2, HO_2 are the product species. The software normalized residuals of the simulations were allowed to converge to values below 10^{-4} to ensure that the simulation has reached steady-state.

4.1.3 One-Dimensional Run Details

The MASIV simulations use the same duct geometry and initial conditions as were estimated from the experiment, except that the MASIV geometry uses a modified area profile which does not include the cavity, since a 1-D formulation cannot include regions of reversed flow.
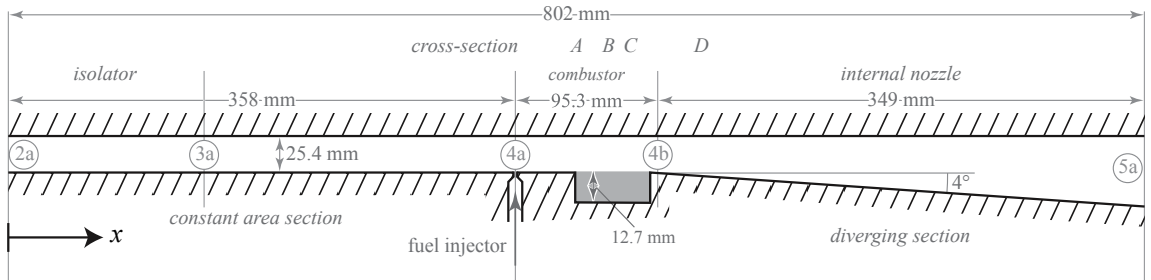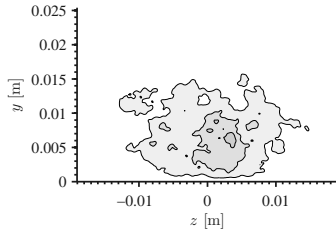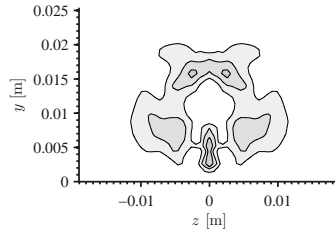

Figure 4.2: Duct geometry for simulation. Note that only the experiment and Fluent simulations include the cavity. MASIV simulations do not include cavity to avoid reversed-flow regions.

67

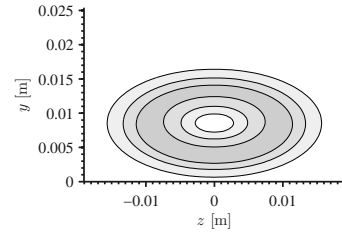Table 4.2: Constant parameters used in the simulation.

Parameter	Value
Pr	0.71
T_w	1100 K
C_f	0.003
r_u	1.96
d_{inj}	2.49 mm

(a) Cross-section A, experiment

(b) Cross-section A, Fluent

(c) Cross-section A, MASIV ROM
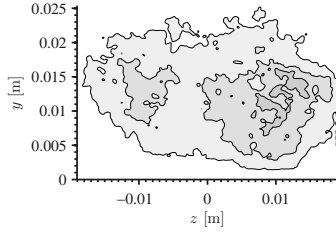
(d) Cross-section B, experiment
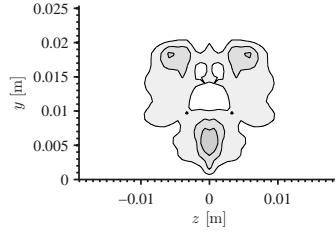
(e) Cross-section B, Fluent
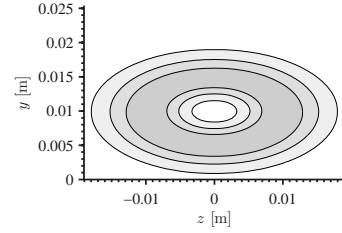
(f) Cross-section B, MASIV ROM
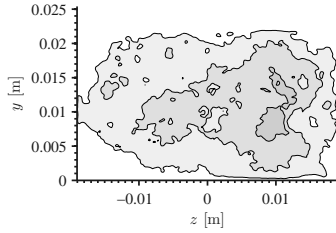
(g) Cross-section C, experiment
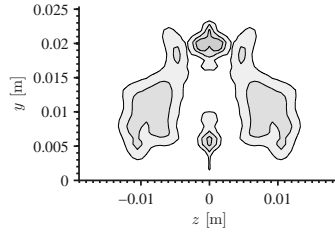
(h) Cross-section C, Fluent
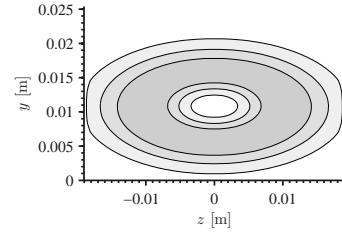
(i) Cross-section C, MASIV ROM

Figure 4.3: Contours of heat release rate in y-z cross-sections at various x-locations. Each image is normalized by its own maximum value. Contours correspond to 25%, 50% and 75% of the maximum value in each image. Cross-section locations are marked in 4.2. The fuel injector is at $x = 0.358$ m, and the x-locations are as follows. (a, b, c): $x = 0.402$ m; (d, e, f): $x = 0.427$ m; (g, h, i): $x = 0.448$ m.
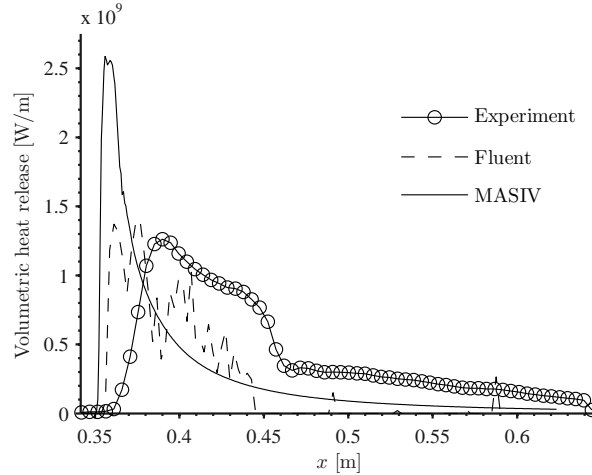
Figure 4.4: Volumetric heat release rate for Experiment, Fluent and MASIV.
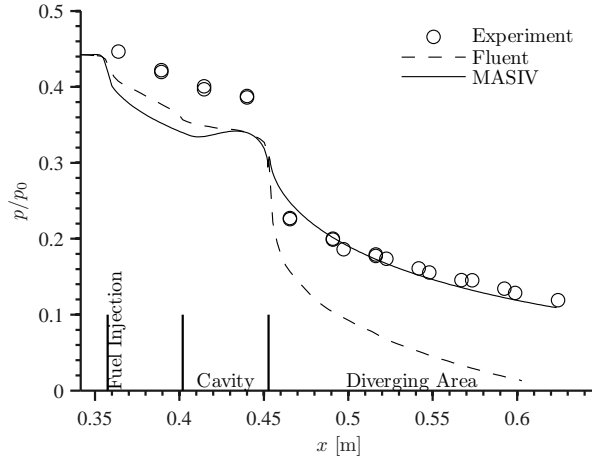
Figure 4.5: Normalized pressure versus distance for Experiment, Fluent and MASIV. Circles shown for the experiment represent measurements at individual pressure taps.

4.1.4   Comparison of methods

Figures 4.3 to 4.10 provide a comparison of results from MASIV, Fluent CFD and experimental data. We used three different metrics to tune the model. First, we analyzed the jet spreading, which can be determined by examining cross-sectional (y-z) planes, and compared the spreading characteristics of each of the three sources qualitatively. Second, we looked at the flame length in the axial plane by comparing luminosity images from experiment to heat release images from the two numerical routines to ensure that the MASIV prediction is realistic. In these images we compared the shapes of the flame boundaries and total flame length. Third, we compared the axial 1-D luminosity from experiment to the 1-D heat release distributions pre-
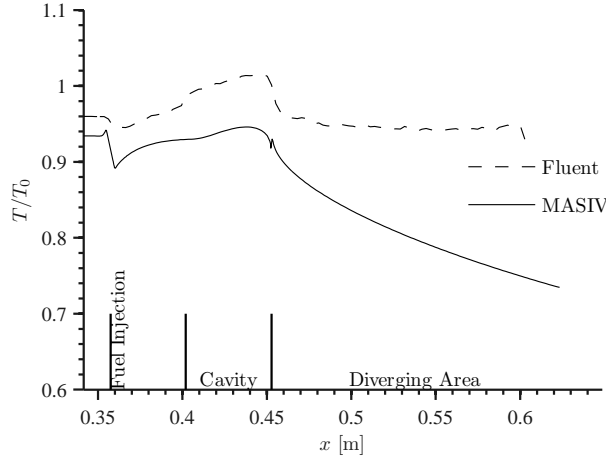
Figure 4.6: Normalized temperature versus distance for Fluent and MASIV.
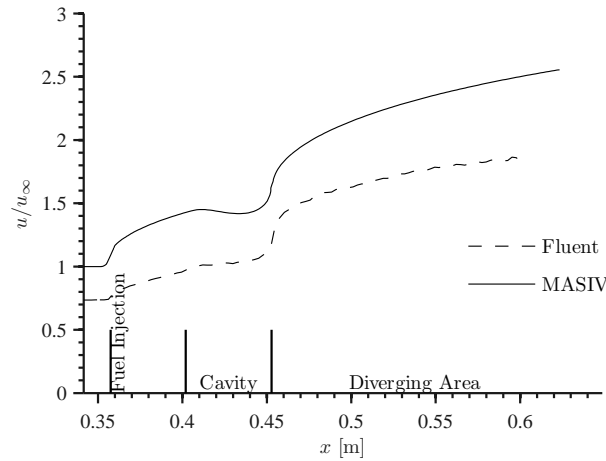
Figure 4.7: Normalized velocity versus distance for Fluent and MASIV.

dicted by the two codes. The total heat release (area under the curve) is expected to be similar among all three.

Contours of the heat release rate in various y-z planes are shown in Fig. 4.3. It is possible that differences between Fluent and MASIV are due to the simplified nature of the scaling relations, (2.12) to (2.20) and (2.22). However, there are some important considerations to make in evaluating the results. First, we note that the Fluent results cannot necessarily be interpreted as a truth model because they do not represent all aspects of the experimental flow field accurately. Results of Fluent and MASIV are compared because they offer different insights into the problem, and they are expected to converge as modeling techniques used in each are improved.

Second, we note that each of the images is normalized to its own maximum, so they are only comparable to each other in a qualitative sense. The figure of merit for these
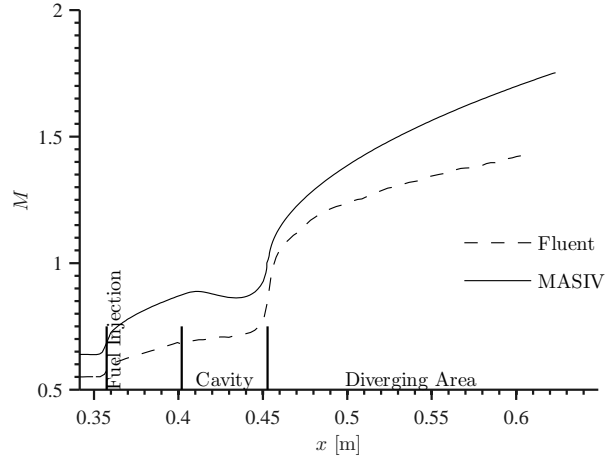
Figure 4.8: Mach number versus distance for Fluent and MASIV.
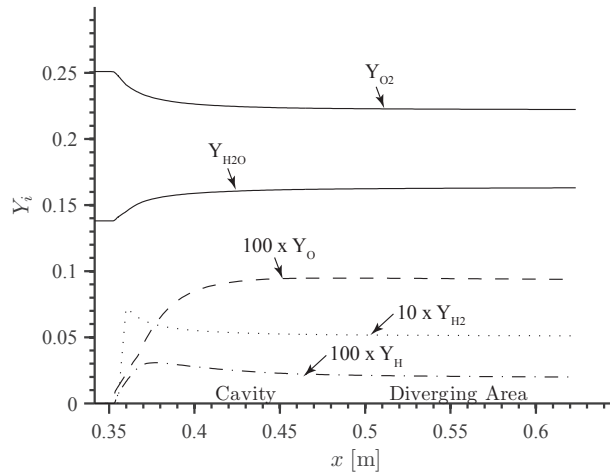
Figure 4.9: Mass fraction versus distance for MASIV.

images is that the loci of maximum reaction rate occur at approximately the same radial distances from the jet centerlines. This means that jet spreading computed by MASIV bears qualitative resemblance to the experiment and CFD cases, although the reaction rate it predicts is necessarily "smeared" annularly around the jet centerline due to the simplified and averaged formulation. Confinement may have an effect on the centerline penetration and spreading of the jet, but is not included in the scaling relations of Hasselbrink and Mungal. Experimental results suggest that the walls may prevent the jet from penetrating as far into the flow as it would otherwise.

The cross-sectional views are important because they give us a qualitative way to evaluate the model. MASIV is not expected to reproduce the detailed structures seen in the experimental results, but reaction contours are expected to contain approxi-

mately the same area (and they do appear to have the same trend here) between the different models and regions of strongest reaction should be concentrated at the same distance away from the jet centerline. The Fluent results at downstream locations are smaller in area than those of the experiment or MASIV because Fluent predicts some small regions of very high reaction rate toward the end of the duct. Although there are significant differences between the different heat release images, the area tests are qualitatively satisfied.

Figure 4.4 shows that the MASIV model predicts stronger heat release very near the injector than does Fluent. This is because of the simplicity of the mixing model used in MASIV, which cannot truly predict the compressive effects of a high-speed crossflow impinging on a jet. This changes the mixing flow field on the front side of the jet, and the resulting compression of the flame causes smaller heat release values.

Figure 4.5 shows that the pressure plots of numerical results differ from the experiment in the combustor region. They show that the computed pressure drops more rapidly than observed in reality. This could be due to heat being lost to the walls of the duct, or to momentum losses due to wall friction. The agreement between MASIV and experiment is probably somewhat coincidental, given that both Fluent and MASIV overpredict the pressure drop due to combustion from $x = 0.35$ to $x = 0.44$. One possible reason for the agreement of MASIV with experimental results in the aft section of the duct is that MASIV predicts that almost all of the reaction will occur inside the longest contour shown in Fig. 4.10c. The extra blobs of reaction predicted by Fluent are accompanied by heat release, which will then drive down the pressure in that section. There are also be heat loss effects in this section of the combustor, but these are difficult to quantify without detailed measurements. Here MASIV has a advantage over Fluent, because the spreading model precludes any of these spurious "hot spots" from arising.

No experimental data were available for the temperature of the duct walls or wall friction, which has a strong effect on the result. Cold walls can remove a great deal of enthalpy from the flow, as can friction work. Experience suggests that the walls of the experiment will be slightly cooler than the vitiated air stagnation temperature, since they will not have enough time to reach equilibrium with the flow, for the short runtimes seen here. This means that the extra drop in pressure predicted by both codes is probably related to the fact that the heat loss to the walls is under-predicted.

Figure 4.6 shows the predicted temperature in the flow for Fluent and MASIV. Again, heat loss to the walls can have a large effect on the flow temperature. A small difference in predicted reaction rate can cause extra heat to be released due to

additional burning of fuel or to recombination of radicals. Also, the more radicals in the flow (and the lower the molecular weight), the lower the temperature will be for a given enthalpy.

Figure 4.7 shows the velocity evolutions for Fluent and MASIV. It is important to note that almost exactly the same trend is predicted by each model. However, the Fluent code predicts a lower velocity than MASIV because it predicts that heavier species make up a greater mass fraction than MASIV does. This, in turn, requires a greater velocity to satisfy continuity. Similarly, the Mach numbers in Fig. 4.8 follows the same trend, although the difference in predicted sound speed (again due to differences in predicted flow composition) brings the plots closer together than in Fig. 4.7. The predicted thermal throat location is almost identical for the two models. As will be seen in section 4.2, the anchoring requirement for transonic flows shows that there is a good reason for this.

Figure 4.9 shows the MASIV-predicted mass fraction of several species of interest. It may be noted that the code predicts that much of the fuel will remain dissociated (which ties up combustion enthalpy) through the end of the duct. At these relatively low speeds this effect cannot be replicated with a finite-rate-limited solver, and a mixing-limited solver like the one shown here is required.

The heat release distributions shown in Fig. 4.10 show strong similarity between the flame shapes predicted by both codes. Since MASIV only includes turbulent effects in a statistical sense, none of the "blobs" of high combustion rate seen in the Fluent result are present (Fig. 4.10b and c). However, the lengths of the various contours are similar in shape and length between the two models. Differences between simulation and experiment are most likely due to larger unsteady effects in the experiment, short experimental run time, and possibly due to diffusion and persistence of luminosity, as well as the high gains necessary to register the image.

Note that the MASIV model underpredicts the flame length, since the large reaction rates near the injector cause the fuel to be consumed quickly, in a short distance. This is because the only way for the flame to be extinguished in the diffusion flame model is for the strain rate to be excessively large and, as noted above, the strain on the front side of the jet is difficult to predict. In the experiment, the fuel not consumed on the front side of the jet convects downstream and burns there, contributing to the longer flame length. Figure 4.11 shows the influence of scalar dissipation rate on the flame. Since the fuel only has a high probability of burning at or very near to the stoichiometric contour, the strain rate at the stoichiometric contour is of primary importance. Note that the top front of the stoichiometric contour has very large
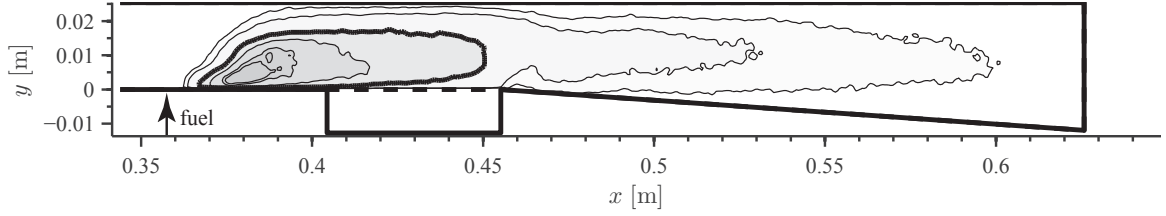
(a) 2-D Side View—Experiment. An OH fluorescence image that shows the estimated intensity of heat release.
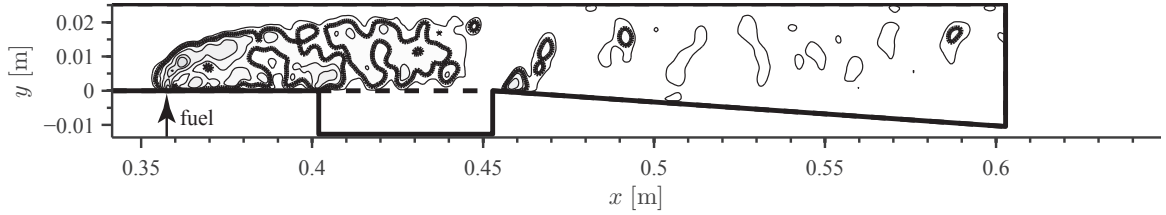
(b) 2-D Side View—Fluent. Heat release calculated as the positive part of the rate of change of sensible enthalpy not due to convection or diffusion.
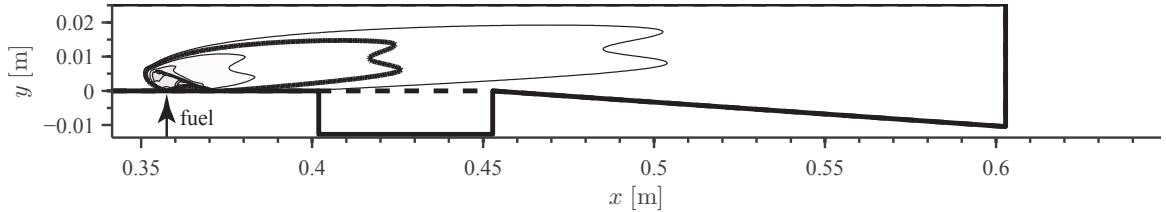
(c) 2-D Side View—MASIV ROM. Heat release calculated as sensible enthalpy change due to reaction only.

Figure 4.10: Heat Release Results. The contours show isoclines containing 90%, 75%, 50%, 25%, 10%, and 5% of the total heat release due to reaction in the duct. Comparison of corresponding isoclines of the three images shows predicted flame length from each. **Bold contours show equivalent amounts of heat release, which are expected to have nearly the same length.**

strain rates, which correspond to incomplete combustion of the fuel.

The effect of scalar dissipation rate on the flamelet can be seen clearly in Fig. 4.12. This figure indicates that a large number of points in the flame react at conditions close to those of the $\chi = 10\text{s}^{-1}$ flamelet, which explains why not all the fuel is consumed.

4.2 Ram validation

The other set of comparisons performed to validate the combustor simulation were done across the two modes in which the combustor operates, ram mode and scram mode. Although the geometry for these tests is the same as that used previously, the

74
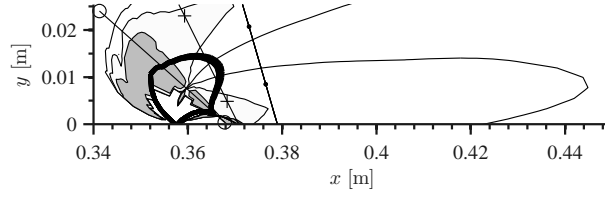
Figure 4.11: Scalar dissipation rate influence on stoichiometric contour ($f_{st} = 0.0316$). The contours of scalar dissipation rate represent $\chi = [1\text{s}^{-1}, 10\text{s}^{-1}, 100\text{s}^{-1}]$ from lightest to darkest. Note that $\chi = 100\text{s}^{-1}$ is the maximum scalar dissipation rate before quenching occurs. The mass fractions along lines marked with symbols $\circ$, $+$ and $\cdot$ are shown in Fig. 4.12.
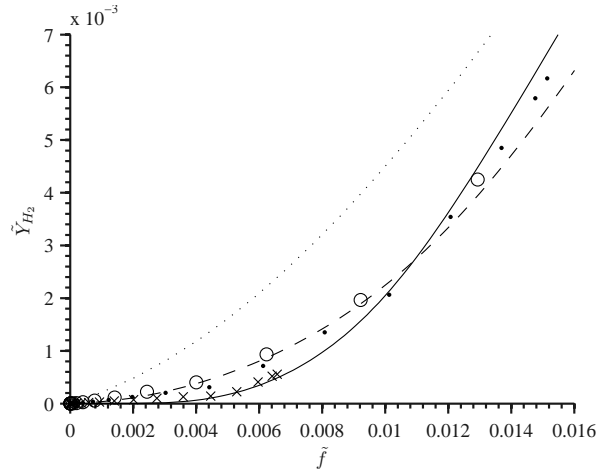
Figure 4.12: Flamelets with $\chi = [1\text{s}^{-1}, 10\text{s}^{-1}, 100\text{s}^{-1}]$. The symbols shown indicate the local mass fractions and mean mixture fractions around locations marked in Fig. 4.11.

run conditions were chosen to vary in equivalence ratio in order to find the point at which the combustor goes from supersonic combustion to subsonic combustion with increasing equivalence ratio.

The cases shown in Figs. 4.13, 4.14, 4.15, and 4.16 correspond to the geometry and run conditions of Fotia and Driscoll [45]. This experiment is a laboratory-scale combustor with flow rates in the range of 200 g/s to 350 g/s of vitiated air. In order to compare accurately to the experiment, a chemistry set representing vitiated air at the required temperature and pressure was used. The solid lines represent computations made by the method proposed here, and the circles represent experimentally measured data. The uncertainty in the measured pressures is about 0.9 kPa [45]. The nominal run conditions are shown in Table 4.3.

Table 4.3: Isolator entrance conditions, station ②

Variable		Value
ρ	=	$0.28\,\frac{\text{kg}}{\text{m}^3}$
p	=	$46.7\,\text{kPa}$
T	=	$521\,\text{K}$
u	=	$977\,\frac{\text{m}}{\text{s}}$
M	=	2.12
γ	=	1.33
ϕ	=	0.198 to 0.313
Y_{N_2}	=	0.64
Y_{O_2}	=	0.22
$Y_{\text{H}_2\text{O}}$	=	0.13
Y_{Ar}	=	0.01

The fuel in the experiment and simulation was hydrogen, and although the experiment used both jet and cavity fueling, the simulation only considers the main jet fuel source since the cavity fueling was only used to ignite the flow at the beginning of the run. Equivalence ratios ranged from 0.198 to 0.313, which spans the ram-scram transition, and provides a resolution of about 0.01 in equivalence ratio. The uncertainty in equivalence ratio was about ± 0.005. This corresponds to fuel mass addition rates of 1.6g/s to 2.1g/s.

Boundary layers internal to the duct were accounted by using the initial value of the displacement thickness, δ^*, as reported in the experiment. Although this treatment is relatively simple, it provides reasonable agreement in terms of qualitative prediction of pressure rise in the combustor as a function of equivalence ratio.

Figures 4.13, 4.14, and 4.15 show the computed flow profiles in which the combustor operated in ram mode. Note that as the equivalence ratio decreases, the pressure rise in the combustor also decreases. The location of choking can be estimated in the experimental results by the presence of a rapid drop in pressure just before $x/H = 5$ in the ram-mode plots.

The constants of the MASIV model used for the ram tests [22] are shown in Table 4.4. These constants were optimized to match the pressure rise of the $\phi = 0.313$ (highest ram equivalence ratio) case and the $\phi = 0.215$ (highest scram equivalence ratio) case in a least-squares sense for all the measurement points from the experiment. The constants used here differ slightly from those used previously [22], but this provided relatively good agreement in all cases where the routine converged (convergence was not achieved for $\phi = 0.234$). Note that this set of parameters provides a good prediction of the maximum pressure rise in the isolator (just before the fuel injector)
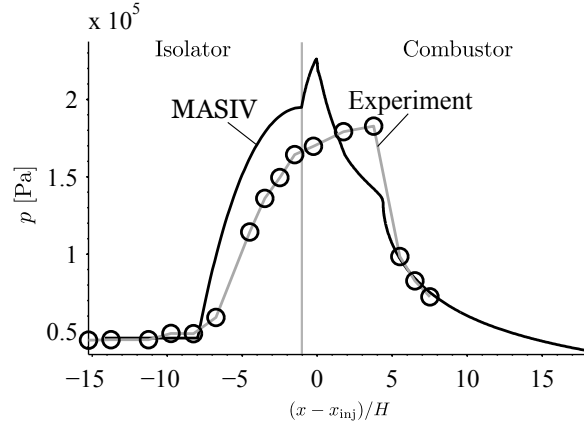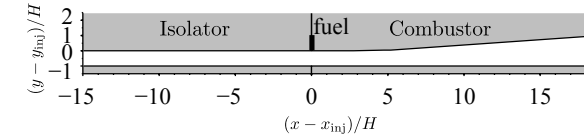
(a) $\phi = 0.313$
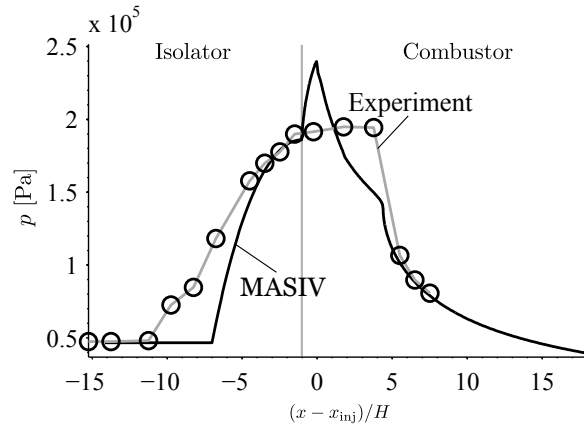
(b) $\phi = 0.301$

Figure 4.13: Ram cases. Pressure profiles through the isolator and combustor for a range of equivalence ratios corresponding to ram-mode operation. Distance from the injector, $x - x_{inj}$ is normalized by the duct height, H.

for most cases and good agreement of the location of choking for all cases. The maximum pressure rise prediction is within the experimental error for cases 4.13b, 4.14a, 4.16a, and 4.16b, within a factor of $2\times$ the experimental error for cases 4.13a and 4.14b, and within a factor of $3\times$ the error for case 4.15a. The mode is predicted to be early scram mode in case 4.15b, although this case appears to operate in ram mode in the experiment. It is not possible to tell from pressure information alone where early

(a) $\phi = 0.290$

(b) $\phi = 0.278$

Figure 4.14: Ram cases, continued. Pressure profiles through the isolator and combustor for a range of equivalence ratios corresponding to ram-mode operation. Distance from the injector, $x - x_{\mathrm{inj}}$ is normalized by the duct height, H.

scram begins in the experiment, but the model is able to predict the mode correctly to within $\Delta\phi \approx \pm 0.02$, the difference between the equivalence ratio of case 4.15b and cases 4.15a and 4.16a Note as well that the length of the pressure rise, based on the equation of Ikui [66] is fairly accurate for all cases except case 4.13b, and 4.15b.

The small peak in pressure in each of the simulation results around $x/D = 0$ is due to the simplistic assumption that the boundary layer thickness goes from a
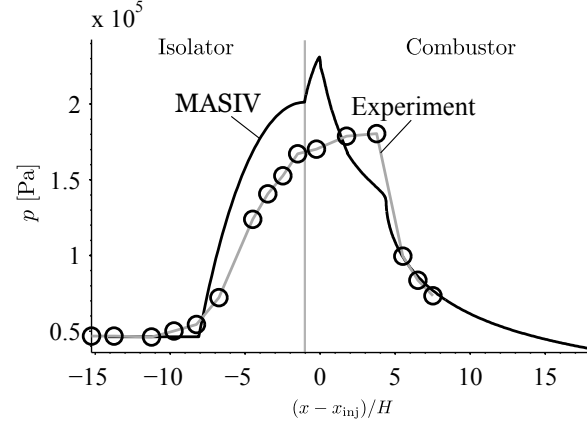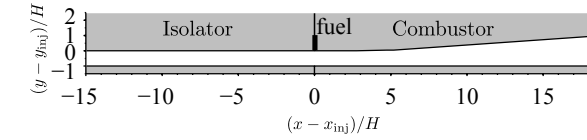
(a) $\phi = 0.267$
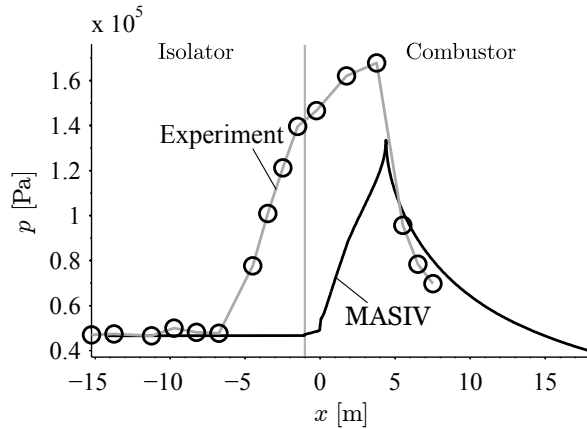
(b) $\phi = 0.234$

Figure 4.15: Ram cases, continued. Pressure profiles through the isolator and combustor for a range of equivalence ratios corresponding to ram-mode operation. Distance from the injector, $x - x_{\mathrm{inj}}$ is normalized by the duct height, H.

large value at the end of the PCST, computed using (2.52), to an assumed value of zero near the injector. Also, the artificial division of the combustor into components (isolator and combustor) means that the PCST is not allowed to overlap with the fuel injection, which adds a small displacement in the upstream direction to the pressure-rise predictions. In the experiment it is observed that the end of the PCST sometimes, but not always, overlaps the injector. Hence, the prediction of the location

Table 4.4: Experimental constants for jet mixing model.

Constant	Experimental Range	MASIV value
c_1	1.2 to 2.6 [50]	2.0
c_2	0.28 to 0.34 [50]	$\frac{1}{3}$
c_3	0.68-0.95 [54]	1.3
c_4	0.76 [50]	0.86
c_5	0.0084-0.0093 [54]	0.009
$\frac{u_{inj} d_{inj}}{\nu_T}$	60-70 [55]	26

of maximum pressure rise is not very good. It is known that 2-D and 3-D effects influence the location of maximum pressure rise [45], but the results shown here indicate that a 1-D model is sufficient to predict the pressure distribution and values up to a displacement in the x-direction.

Figures 4.16a-b show the series of cases in which the combustor operated in scram mode. Note that as the equivalence ratio decreases, the pressure rise in the combustor also decreases, although less dramatically than in ram mode. These plots can be used directly to asses the heat release model, since in a fully supersonic flow there is no PCST to affect the modeling of pressure rise and all pressure rise is due to heat addition or geometric divergence. The agreement between computations and experiment in both plots here is good. The main discrepancy is due to the effect of facility shocks in the experiment, present in both plots, between $(x - x_{\text{inj}})/H = -10$ and $(x - x_{\text{inj}})/H = 0$ (apparent as oscillatory behavior).

4.3 Trajectory optimization

As previously discussed, measured in-flight trajectory information is not available for HSVs. This makes it impossible to validate the predictions of the overall vehicle dynamics of the MAX-1 against experimental measurements. However, it was possible to compare the results of two different optimization methods in order to verify that the trajectory simulations and optimizations were indeed solving the problems they were intended to solve. This verification raised some concerns that required attention.

The two types of optimization methods that were considered were a surrogate method and the collocation method. With the surrogate method, a set of performance maps are first computed, using the independent dimensions of Mach number and acceleration. The optimum trajectory is determined by interpolating between points in the table to find the set of accelerations that yield minimum fuel for a given range
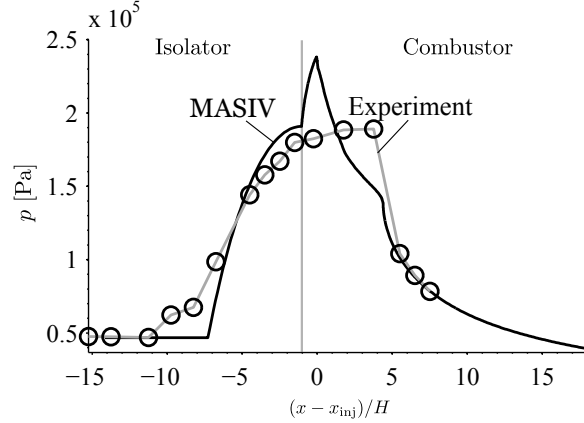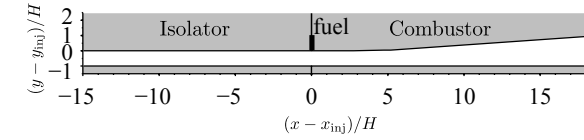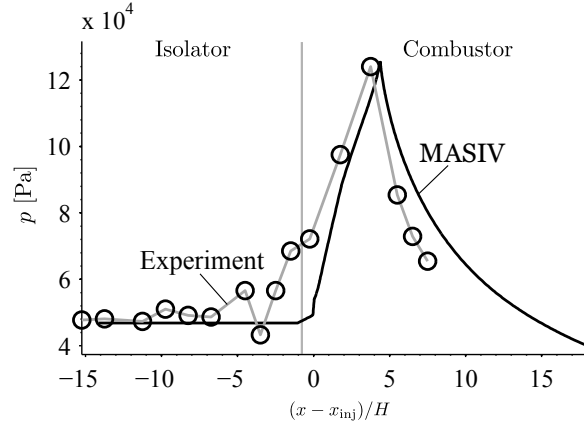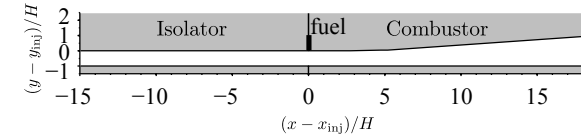
(a) $\phi = 0.215$
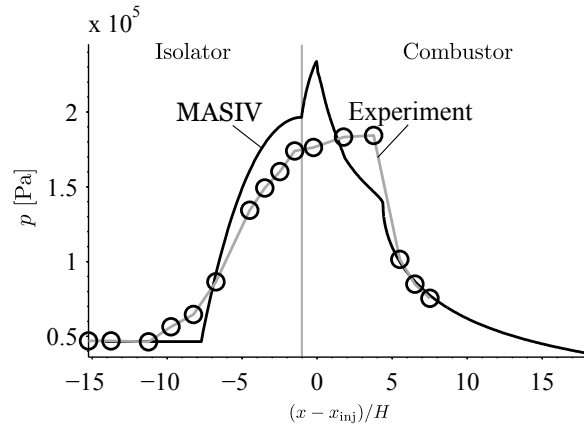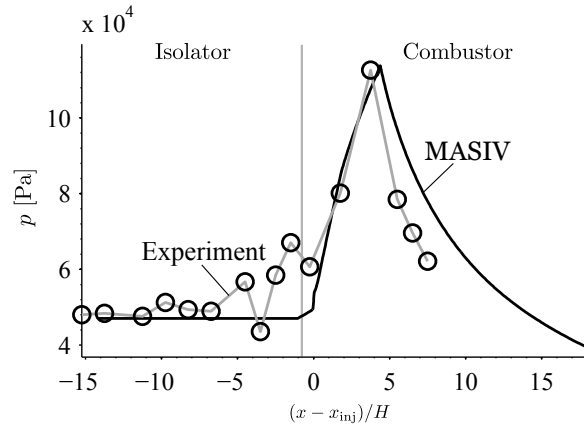

(b) $\phi = 0.198$

Figure 4.16: Pressure rise through the combustor for a range of equivalence ratios corresponding to scram-mode operation. Distance from the injector, $x - x_{\text{inj}}$ is normalized by the duct height, H.

of Mach numbers. The surrogate model was a rectangular table, created using 13 points in the Mach-number (M) direction and 5 points in the $\dot{\mathbf{v}}$ direction. At each point in the table, the vehicle is trimmed to the appropriate (M, h) for the constant dynamic pressure trajectory and given acceleration. The optimization is performed by interpolating on the table using 3rd-order splines, so that quasi-Newton optimization can be used. The trajectory was generated by placing 80 points equally spaced in

M, from $M = 7$ to $M = 13$, and allowing the $\dot{\mathbf{v}}$ of each of these points to vary. The result of this optimization is a trajectory through $M - \dot{\mathbf{v}}$ space, shown in Figure 4.17. This method is described in detail by Dalle et.al. [4].
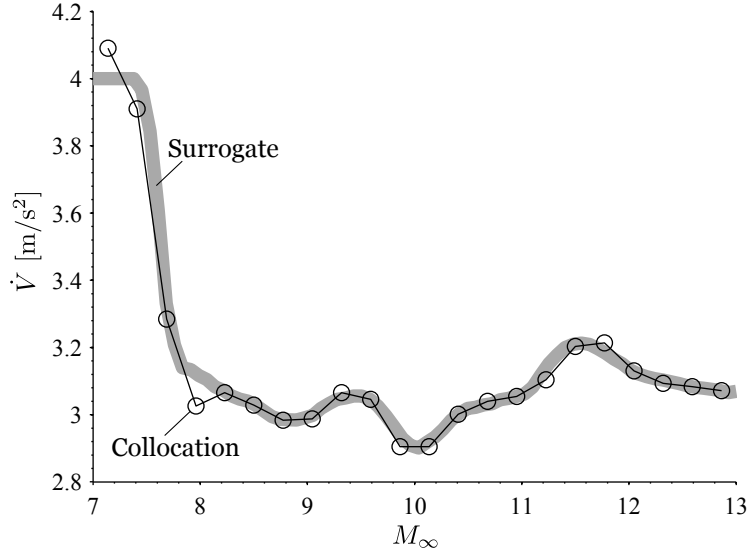
Figure 4.17: Optimization result based on a surrogate model, with intervals used to approximate the surrogate result for the trajectory-simulation case shown as circles.

As previously described, collocation method optimization shown here was performed with Δt_i as the decision variables, rather than directly solving for $\dot{\mathbf{v}}_i$. There were 12 nodes in the trajectory (nearly the same as the 13 used to generate the surrogate table), corresponding to 11 acceleration intervals. Accounting for the control nodes, there are 22 total acceleration intervals in each simulated trajectory. This is shown in Fig. 4.17, superimposed on the surrogate-based optimized trajectory. These two curves differ slightly because while the trajectory-based is trimmed at each point used in the simulation, the surrogate is only trimmed at each point in the table. Hence, the interpolated points are not necessarily trimmed. The cost of following this trajectory, based on the surrogate model, was estimated to be 6079 kg. The trajectory-based estimate of the cost was 6204 kg. This 2% difference is attributed to the difference in trim requirements between the models, as well as the coarseness of the surrogate. The trajectory-based cost of following this trajectory is accepted from this point on as the cost of following the minimum-fuel trajectory identified by the surrogate-based optimization. This is required to avoid conflicting cost estimates. Thus, the baseline cost of a "good" trajectory is established to be 6204 kg.

To verify these optimizations against each other, we attempted to optimize using the trajectory-based cost estimates, beginning from the baseline trajectory. If the two

Table 4.5: Two trajectory points in 11-space

i	Δt_i origin (s)	Δt_i destination (s)
1	50.8363	40.7979
2	50.9347	49.0353
3	51.4046	54.4477
4	51.5239	51.2712
5	51.2191	54.0153
6	51.2922	52.6558
7	51.6363	51.2361
8	51.6528	50.3708
9	51.6704	48.8422
10	51.6255	50.1246
11	51.6766	53.8664
	Δm origin (kg)	Δm destination (kg)
	6151	6138

models agree and the optimization schemes are compatible, it is expected that the trajectory-based optimization will return to the same (or a very similar) trajectory, starting from an initial condition created by perturbing the baseline trajectory. We found that perturbed initial conditions did not return to the baseline trajectory (or a better one), when the same optimization scheme was applied as was applied to the surrogate.
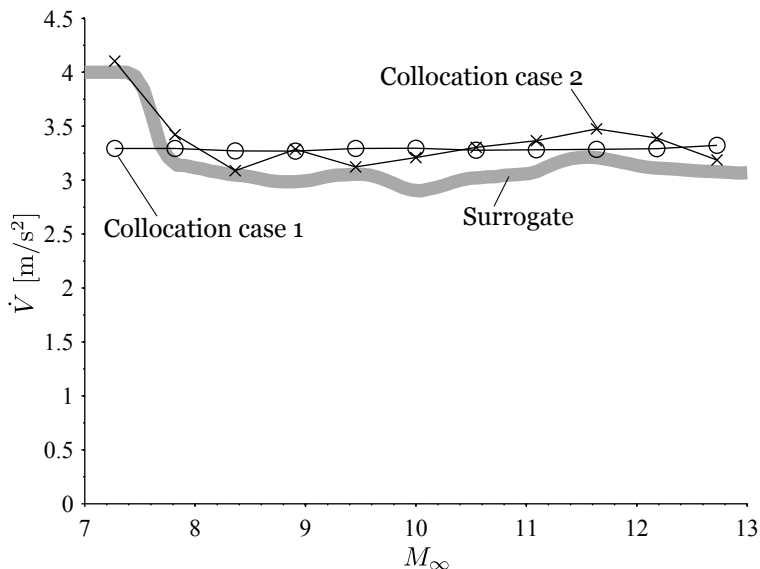
Figure 4.18: The two trajectories chosen to examine the properties of the cost function. Circle denotes the "origin" trajectory and x denotes the "destination" trajectory.

This prompted a study of the cost function ($\Delta m = \Delta m(\Delta t_i), i = 1 \ldots 11$) under-

lying the optimization. The fuel cost function (which is simply a scalar function of 11 variables) was analyzed by choosing a condition near to the established baseline, and drawing a straight line (in $\mathbb{R}^{11}$) between the point in question and the baseline. Note that each point in $\mathbb{R}^{11}$ describes a unique trajectory. The two trajectories described in Table 4.5 are shown in Fig. 4.18. These trajectories differ in fuel cost by about 0.22%, which is a small difference, but certainly significant if tolerances of 10^{-3} or smaller are used. In other words, the difference in cost between these trajectories should be detectable by the optimizer, which had a cost function tolerance of 10^{-6}. The Δt_i values given in Table 4.5 show significant variations in the lengths of the intervals.
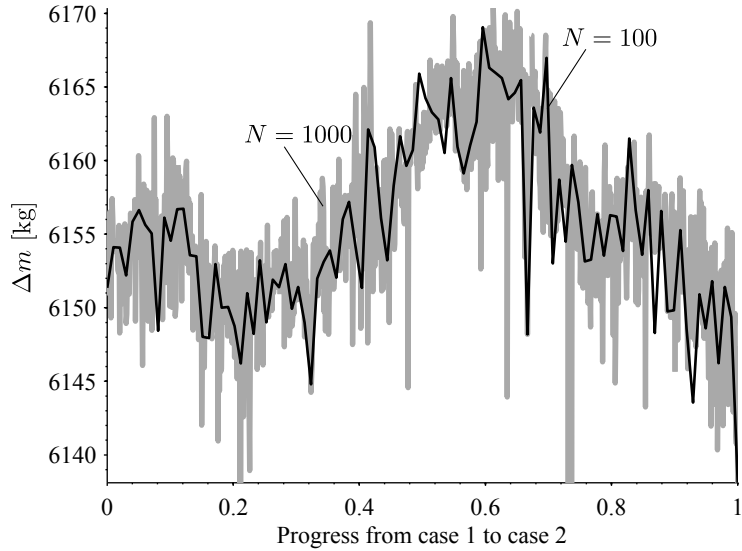
Figure 4.19: Truncation error between adjacent points traveling along a line between conditions shown in Table 4.5.

Figure 4.19 shows the problem with the cost function. The truncation error from all sources (performance estimation and trajectory simulation) is excessively large. This is shown with 100-point resolution in black, and 1000-point resolution in gray, which indicates that it is a truncation error problem, rather that a problem of step sizes that are too large. Although the general subject of truncation error is a frequent topic in numerical simulations, the subject of truncation error as it pertains to trajectory cost estimation does not seem to have been covered much in the literature. This is because most models either use fundamental models or tabular data [4, 16, 19, 20]. The use of tables and smooth basis functions obscures this problem with the underlying cost function, if it exists in a particular simulation. The "jitter" observed in Fig. 4.19 is a result of the truncation error, evident in deviations between successive

Table 4.6:   Trajectory optimization run details – cost order

Run #	IC	$\sum_i |\Delta t_i^{n+1} - \Delta t_i^n|$	Conv. Tol.	Cost (kg)
1	max. accel.	$> 0, < \infty$	10^{-6}	2843
2	baseline	$> 0, < \infty$	10^{-6}	2865
3	baseline	$> 0, < \infty$	10^{-3}	2865
4	max. accel.	$> 10^{-3}, < 0.1$	10^{-6}	2866
5	max. accel.	$> 10^{-5}, < 0.1$	10^{-6}	2870
6	max. accel.	$> 0, < \infty$	10^{-3}	2871
7	baseline	$> 10, < \infty$	10^{-3}	2872
8	max. accel.	$> 10, < \infty$	10^{-3}	2878
9	baseline	$> 1, < \infty$	10^{-3}	2893
10	baseline	$> 30, < \infty$	10^{-3}	2895
11	baseline	$> 0, < \infty$	10^{-6}	2907
12	baseline	$> 10^{-5}, < 0.1$	10^{-6}	2909
13	rand. accel.	$> 10, < \infty$	10^{-3}	2923
14	rand. accel.	$> 30, < \infty$	10^{-3}	3020
15	max. accel.	$> 30, < \infty$	10^{-3}	3135
16	mid. accel.	$> 0, < \infty$	10^{-6}	4879
17	min. accel.	$> 10, < \infty$	10^{-3}	4958
18	rand. accel.	$> 0, < \infty$	10^{-6}	7562
19	min. accel.	$> 0, < \infty$	10^{-3}	8296
20	rand. accel.	$> 10^{-2}, < 10$	10^{-3}	11060
21	rand. accel.	$> 1, < \infty$	10^{-3}	12000
22	rand. accel.	$> 10^{-3}, < 10$	10^{-3}	14420
23	min. accel.	$> 10^{-5}, < 0.1$	10^{-3}	18570

simulations that are too large for the optimizer to ignore them. The solution we implemented to deal with this problem was to reduce the function convergence tolerance in the optimization to 10^{-3} and to add the additional constraint that

$$\sum_i |\Delta t_i^{n+1} - \Delta t_i^n| >= 30\text{s} \tag{4.1}$$

where n represents the current iteration of the optimizer and $n + 1$ represents a candidate step toward the minimum. This constraint implies that the total time elapsed must change by at least 30s between trajectories for the trajectories to be considered significantly different by the optimizer. This value was chosen based on Fig. 4.19, since the change in time elapsed was 29.7s, and based on a study of different starting conditions for the optimization, presented in Table 4.6.

This series of tests indicates that by selection of appropriate step sizes and a reasonable initial condition, even the relatively "jittery" cost function shown here can

be used for optimization. Although reducing the truncation error of the simulation would allow for a more accurate optimization of the trajectory, it is important to note that any trajectory optimization of this type will be subject to this problem to some degree. Usually, however, the cost function can be computed to such high accuracy that the step sizes used in the optimization are large enough that it is not apparent. It is unclear whether other models will have the same type of truncation-error jitter, but it seems likely that any performance calculation that involves an iterative process with a termination tolerance will have a limiting effect on the final accuracy available to the optimizer. Any optimization that directly makes use of such simulations must have appropriate step sizes and convergence tolerances. Since the trajectory-based optimization was able to achieve results better than the surrogate-based optimization for a variety of starting conditions, and since the results are similar, the validation indicates two things: the surrogate-based optimization was successful at finding a coarse global minimum, and the trajectory-based optimization was successful at improving this result, both by ensuring a feasible trajectory due to the trim requirement and by finding a better minimum. "Hybrid" approaches of this type are advocated by Conway [87].

CHAPTER 5

Results

The purpose of developing and validating the MASIV/MASTrim model was to create a vehicle performance calculation tool that is "as simple as could possibly work" (in the words of one reviewer). Although it is perhaps difficult to say what constitutes the simplest thing that could possibly work, the above validation tests show that even a code as simple as the one presented here is capable of predicting much of the operational behavior of the dual-mode flowpath. It even predicts several behaviors, such as ram-scram transition, that are considered difficult to capture with CFD. In fact, some of the quality of the results seems to be due to the simplicity of the code. That is, cause-and-effect relationships and appropriate values for empirical constants (such as the 6 shown in Table 4.2) are much easier to establish here than is often the case with **CFD!** (**CFD!**). Also, since some of the behaviors of the dual-mode engine are "emergent," in that they arise from relatively simple interactions between several phenomena, rather than complex fluid flow, a simple model can enjoy some success.

The uses of such a code are to predict the behavior of a system that is more-or-less untestable on the ground (that of the HSV). Full-vehicle HSV system test, including the inlet and nozzle, are substantially more difficult than direct-connect combustor tests, even if the vehicle were to be scaled down. These results take two forms: performance estimates over a range of conditions and trajectory fuel cost minimizations. These results are briefly summarized, and then followed by the original conclusions they served to indicate, and the design methodologies they inspire.

5.1 Thrust

Thrust predictions were made for the Micka/Fotia [44, 45] combustor, with the inlet and nozzle from MAX-1 added to the front and back, in order to estimate the performance of this flowpath in flight. The flowpath geometry was the same as the

Table 5.1: Flight condition of the ram/scram thrust cases

Variable	Value
M_∞	4.18
h	25km
α	3.6°
ϕ_{scram}	0.215
ϕ_{ram}	0.267

geometry of the validation laboratory experiment shown in Figs. 4.2, 4.13, 4.14, 4.15, and 4.16. The full flowpath geometry is also shown at the top of Figs. 5.2 and 5.3. This configuration is only slightly different from the baseline combustor, in that it has different injector position, diameter, and spacing. The cases shown in Figures 5.2 and 5.3 represent two different cases having the same flight condition but different amounts of fueling. The flight condition used represents a case near the boundary of the ram/scram transition, and was selected to be equivalent to the conditions used in the laboratory experiment, given the inlet geometry shown in Fig. 3.1. In order to match the experimental pressure, temperature, and velocity conditions, the flight Mach number is $M_\infty = 4.18$, the altitude is $h = 25$km and the angle of attack is $\alpha = 3.6°$, which are a relatively low Mach number and a relatively high angle of attack for this flowpath. The equivalence ratio was 0.215 for the supersonic combustion case and 0.267 for the subsonic combustion case, a value that is large enough to cause choking in the combustor. These values correspond to the test conditions used in Fig. 4.16a and Fig. 4.15a, respectively, and these conditions are summarized in Table 5.1. The purpose of Fig. 5.1 is to show thrust conditions on both sides of ram-scram transition. The thrust was computed by stream tube momentum analysis from the front to back of the combustor,

$$F = I_e - I_i \tag{5.1}$$

where the impulse, I, is defined as in (2.50). Thrust of the combustor is computed accounting for all the air that flows through the combustor and not including the pressure losses in the isolator. Using this definition, thrust was 1.7kN in the ram case and -0.24kN in the scram case.

This example shows that vehicle thrust can be dramatically different on either side of a ram-scram transition. The negative scram mode thrust is not desirable and it indicates that the inlet geometry used for this example is not appropriate for the flight condition. Specifically, at the flight condition required to match the

experimental conditions, the angle of attack is too high (which creates too much drag) and the Mach number is too low (which does not cause enough compression in the inlet) to allow scram-mode operation with significant positive thrust.
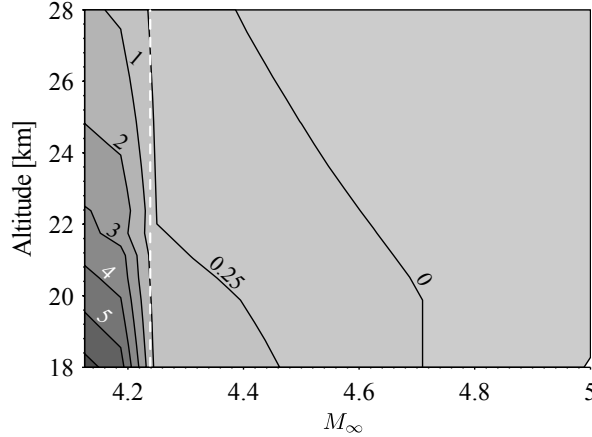
Figure 5.1: Uninstalled thrust in kN of the flowpath shown in Fig. 5.2 as a function of flight Mach number and altitude, with $\phi = 0.267$ everywhere. The white dashed line shows the approximate location of ram-scram transition, with ram-mode being on the left ($M_\infty < 4.22$).

Figure 5.2 shows the Mach number and velocity, and Fig. 5.3 shows static pressure and stagnation pressure in the duct at the two different equivalence ratios. These cases have identical inlet profiles ($x < 1.8\mathrm{m}$) since the flight condition is the same in both cases.

In Fig. 5.2 it can be seen that the ram case achieves a higher exit Mach number and velocity than the scram case, which explains why the ram condition generates more thrust. In Fig. 5.3 this behavior is explained by noting that in the ram mode, the combustion occurs at higher pressures throughout the combustor, giving greater thermal efficiency.

Figure 5.3b shows that the scram mode has a greater stagnation pressure loss than the ram mode. This result is unexpected because it is not predicted by more elementary analyses which do not take into account the effect of pressure on heat conversion to momentum. This greater stagnation pressure loss is attributed not to greater lost work in the scram mode, but instead to greater pressure rise in the ram mode due to combustion at higher pressures. In other words, the ram mode has greater p_0 losses across the isolator shocks, but the scram mode has larger p_0 loss in the heat addition region.

Extending the analysis to a range of flight conditions, Fig. 5.1 shows the thrust
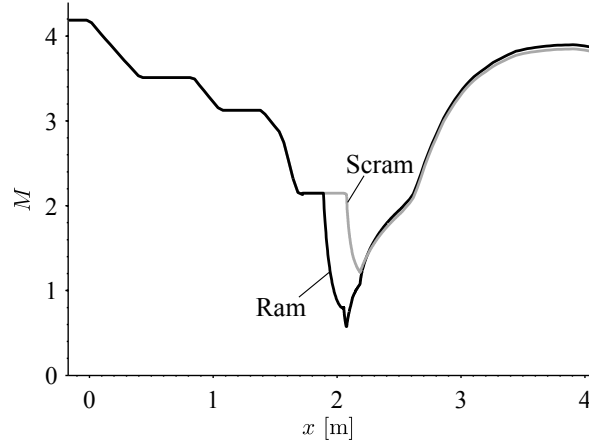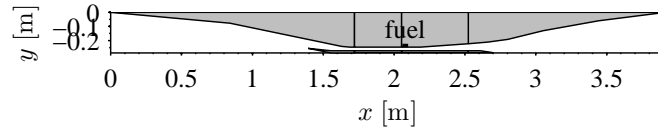
(a) Mach number
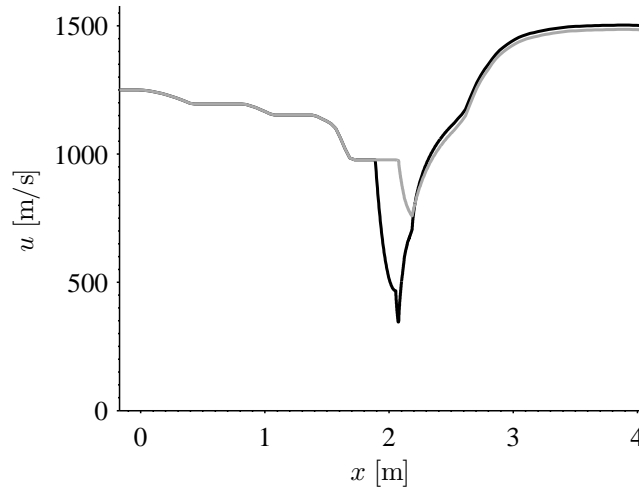
(b) Velocity

Figure 5.2: Computed ram-mode (black) and scram-mode (gray) flow properties at $M_\infty = 4.2$, altitude $h = 25$km, $\alpha = 3.6°$. For ram mode, the equivalence ratio is $\phi = 0.267$ and for scram mode, $\phi = 0.215$. Note that these equivalence ratios correspond to the equivalence ratios in Fig. 4.15a and 4.16a.

for a range of flight Mach numbers and altitudes. Results on the left side of the white dotted line represent ram mode, while those on the right represent scram mode. Figure 5.1 shows that thrust in ram mode is greater than the thrust in the scram mode for a range of conditions. Most significant on this plot is the difference in slope, $\mathrm{d}F/\mathrm{d}M_\infty$, between ram-mode and scram-mode operation. The discrete jump
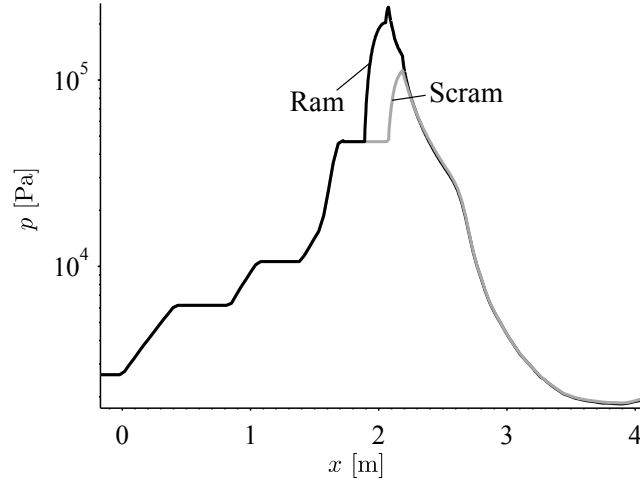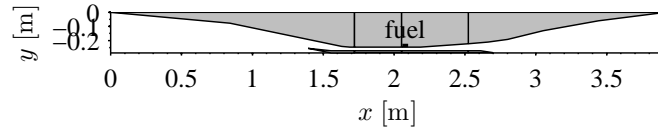
(a) Pressure
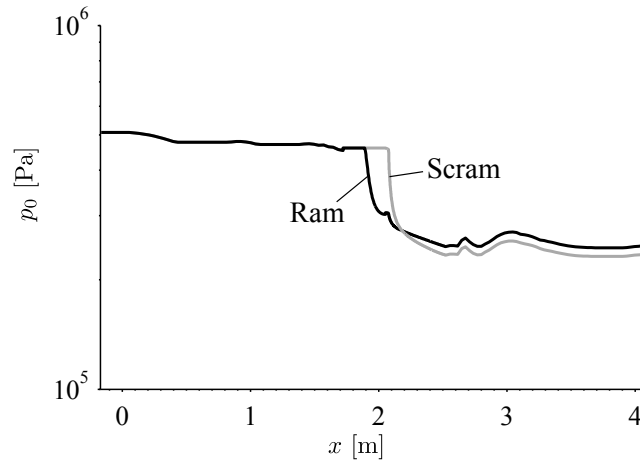
(b) Stagnation pressure

Figure 5.3: Computed ram-mode (black) and scram-mode (gray) flow properties at $M_\infty = 4.2$, altitude $h = 25$km, $\alpha = 3.6°$. For ram mode, the equivalence ratio is $\phi = 0.267$ and for scram mode, $\phi = 0.215$. Note that these equivalence ratios correspond to the equivalence ratios in Fig. 4.15a and 4.16a.

in thrust and the difference in slope of thrust with respect to flight Mach number on either side presents a serious control issue.

Finally, Fig. 5.4 shows the equivalence ratio at which thermal choking is predicted to occur for a range of Mach numbers, from the lowest Mach number at which ram
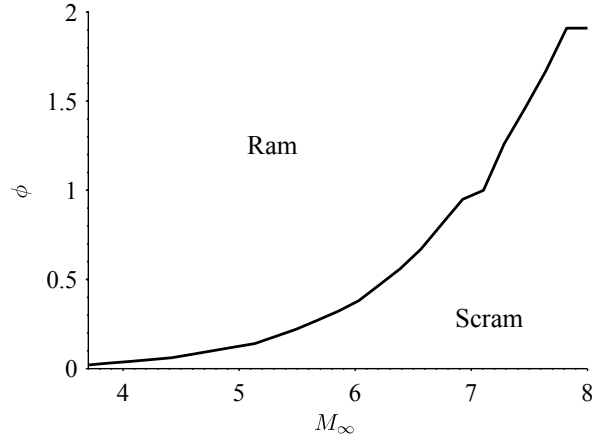
Figure 5.4: Equivalence ratio at which thermal choking occurs for a range of flight Mach numbers at an altitude of 18 km.

operation was possible to the highest Mach number at which enough heat could be added to choke the flow. This figure indicates that the allowed margin of ϕ before choking occurs is mostly a function of the Mach number at the entrance to the isolator, itself a function of the flight Mach number and the inlet geometry. It is impossible to compare Figs. 5.1 and 5.4 to experiment since, to the my knowledge, no data are available for dual-mode scramjets in flight.

5.2 Scram-mode combustor optimization

During an ascent the scram-mode-only portion of the trajectory uses very little fuel compared to the total amount ($\sim 12.2\%$), because it is relatively short in duration (just over 5 minutes). Beginning with the MAX-1 vehicle half full of fuel at such a high Mach number may not be realistic. However, the baseline vehicle was designed for $M = 8$ [22, 36] so this scram-only trajectory corresponds to the original design configuration.

Figure 5.5(a) shows the geometry of the combustor originally used by Micka et.al., [64], which was used to determine some of the constants used in the MASIV model (this is the same combustor shown in Fig. 5.5(a)). Another geometry of the same family is shown in Fig. 5.5(b), based on the description given in [82].

An optimization was conducted to determine the effect on fuel consumption in the scram mode when 3 basic parameters of common combustor designs are varied. This optimization used the same trajectory analysis method as shown in section 3.1.7, but since the goal of this optimization was simply to study some general principles
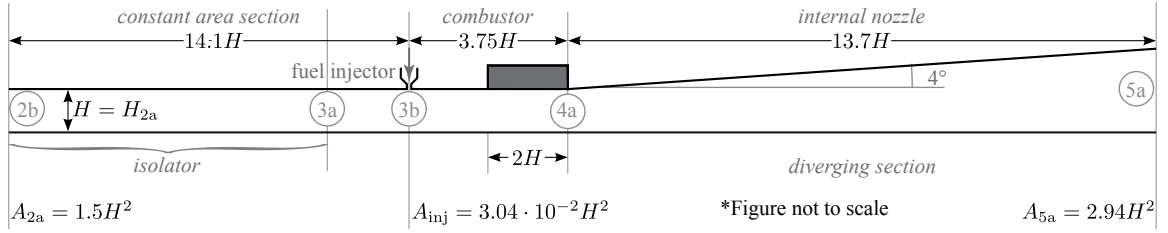
(a) The combustor configuration of Micka et al. [64]
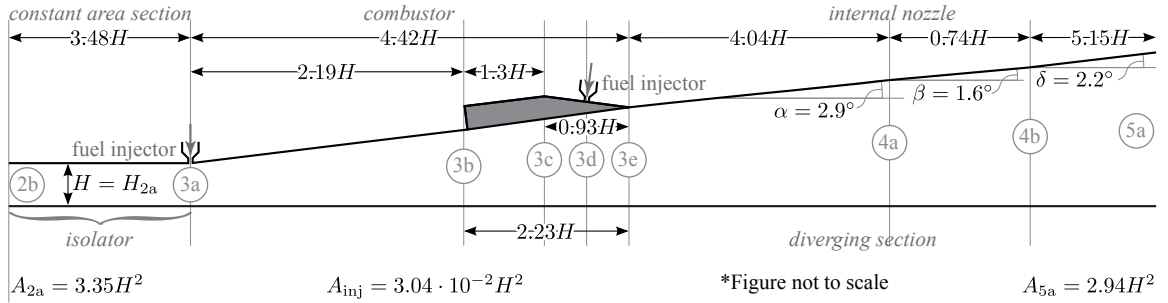
(b) The combustor configuration of Donde et al. [82], due originally to Donohue

Figure 5.5: The two combustors used as design inspiration for the present work.

of high-Mach-number scram operation, the trajectory chosen was fixed, and it goes from $M = 8$ to $M = 10$. The trajectory used is shown in 5.6
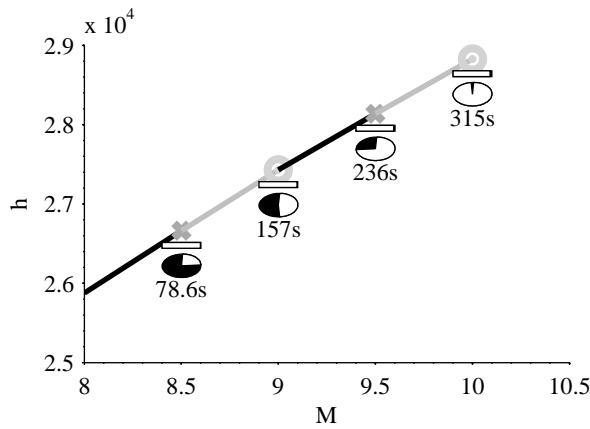
Figure 5.6: Scram-mode-only trajectory path through $M - h$ space, with h in m. The rectangular bars show fuel consumed compared to overall fuel ($22700\,\mathrm{kg}$ in this case) and the circles show time elapsed compared to total maneuver time, with elapsed time printed below. Points marked with circles are trajectory nodes, (i); points marked with x's are trajectory arc midpoints, $(i - \frac{1}{2})$.

In order to optimize the combustor geometry, three parameters were selected based on our earlier examination of existing combustors, [88]. The parameters selected are

as follows (Fig. 5.7):

- Location of fuel injectors with respect to the front of the combustor, x_{inj}

- Location of diverging panel with respect to the front of the combustor, x_{div}

- Angle of diverging panel, α_{div}

Some other important parameters which are not varied in this thesis are

- Number of fuel injectors. This was set to 9/m in the transverse direction.

- Angle of fuel injector centerline with respect to the wall. This was set to 90°.

- Number of panels in the combustor. This was set to 1.

- Diameter of fuel injectors. This was set to 54mm.

One reason why the number of injectors and number of panels were not varied is that they take only integer values and cannot vary continuously. Varying them would prevent the use of a continuous, gradient-based optimization scheme and would require an integer programming environment, which was undesirable.

The fixed-trajectory combustor geometry optimization problem is stated

$$\text{minimize} \quad \Delta m_{\text{fuel}} = \int_{t_0}^{t_f} \dot{m}_{\text{fuel}}(\tau, x)\, d\tau \tag{5.2}$$

$$\text{w.r.t.} \quad \begin{bmatrix} x_{\text{inj}} & \alpha_{\text{div}} & x_{\text{div}} \end{bmatrix}$$

$$\text{subject to} \quad 0 < x_{\text{inj}} < L_{\text{comb}}$$

$$0 < \alpha_{\text{div}} < \pi/4$$

$$0 < x_{\text{div}} < L_{\text{comb}} \tag{5.3}$$

Three optimizations were performed with this fixed trajectory and set of design parameters. First, only the axial position of the injector, x_{inj}, was allowed to vary, while α_{div}, x_{div}, and all other properties of the vehicle and combustor were kept constant. Second, only the axial position of the injector, x_{inj}, and the divergence angle of the panel α_{div}, were allowed to vary, while x_{div} and all other properties of the vehicle and combustor were kept constant. Third, all three of the optimization state variables (the axial position of the injector, x_{inj}, the divergence angle of the panel α_{div}, and the axial position of the front of the panel, x_{div}) were allowed to vary, while all other properties of the vehicle and combustor were kept constant.
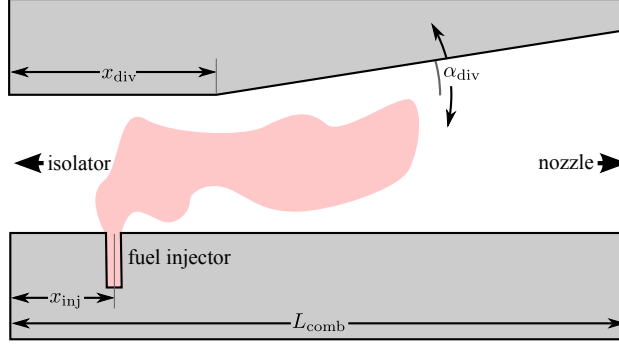
Figure 5.7: Parameters of interest for a generic 2-D combustor.

None of the constraints was active in any of the optimizations. However, the upstream limit of fuel injector location at 0 was invoked because placing the injector farther upstream would cause some of the fuel to diffuse upstream out of the combustor domain, where it is not accounted for in the simulation. In effect, this means that the preferred injector position for scram operation was as far upstream as allowed by the vehicle design, presumably because this gives greater compression due to confinement in the constant-area section of the combustor.

Finally, the operating map of the optimized combustor is shown alongside the previous two examples in Fig.5.8(b). Note that the performance of the combustor that was optimized using a single panel is better than the baseline (Fig. 5.5a) by 3%, while the performance of the combustor shown in Fig. 5.5b is 7% better than the baseline (percentage improvements were computed by the mean of the performance improvement at all points in the thrust maps). This indicates that combustor shape accounts for much of the thrust performance, which is the expected result. Thus, combustor shape, including number, location, and divergence angle of panels, as well as location of fuel injector, should be included in geometric optimizations of ramjet combustors.

5.3 Trajectory Optimization

Once the validation (discussed above in section 4.3) was complete, further runs were made to optimize the trajectory of the MAX-1 vehicle. These runs consisted of the variety of different run conditions shown in Table 4.6. The dynamic pressure, q was held constant at 101kPa, and the MAX-1 vehicle ascended and accelerated from $M = 7$ to $M = 13$. The optimizer in each case used the quasi-Newton method with line search. The Hessian update was done using the Broyden-Fletcher-Goldfarb-Shanno
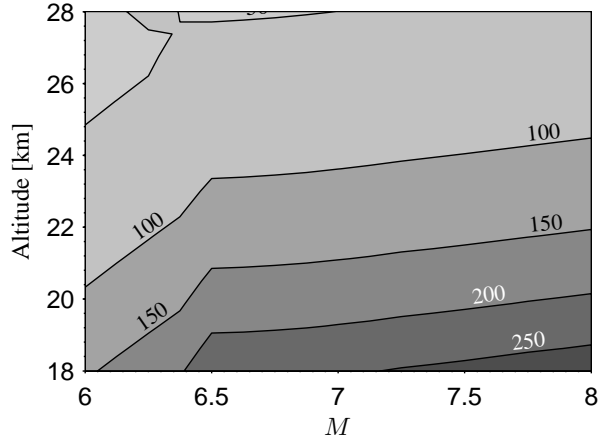
(a) Micka/Fotia combustor.
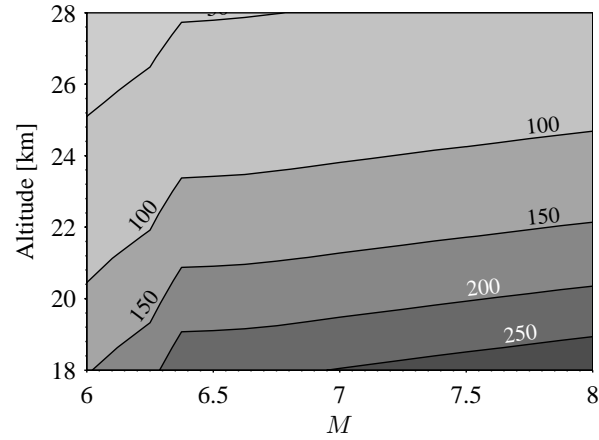
(b) Optimized combustor.

Figure 5.8: Performance maps of iso-thrust curves in kN, versus altitude and flight Mach number for the baseline combustor geometry (shown in Fig. 5.5(a)) and for the optimized combustor.

scheme (BFGS). Runtimes varied with the difficulty of the problem. In general, runtimes for cases with good initial guesses took $\sim$ 19-27hr. Cases that had initial conditions very far from their eventual optimized values took anywhere from $\sim$ 33-93hr. Each iteration of MASIV takes about 3s, so the trajectory simulation takes $\sim$ 3-5min for each trajectory considered, and the optimization cases required 74-343 evaluations of the trajectory fuel cost function.

Figure 5.9 shows the resulting accelerations of the collocation trajectories for all the cases that had less fuel consumed than the baseline optimization (defined as the result of the surrogate optimization). Note that only cases that had initial guesses derived from perturbations of the baseline trajectory, or from the maximum acceler-
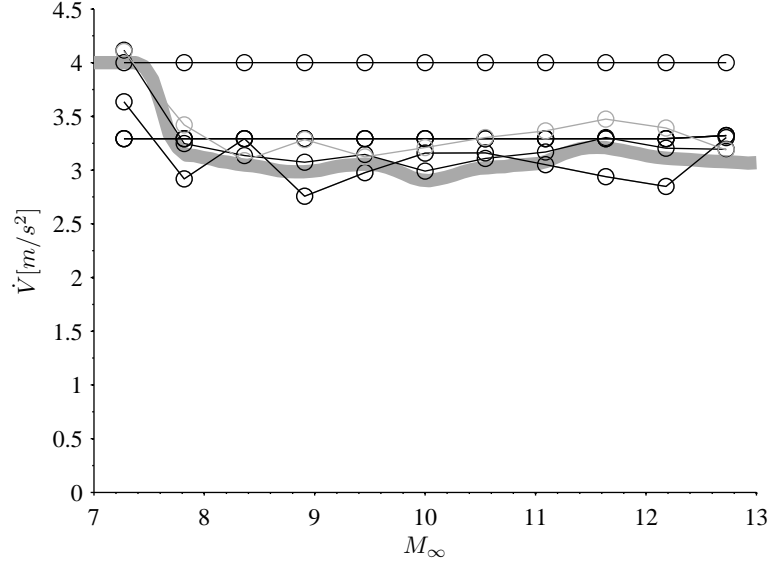
(a) Initial guesses.
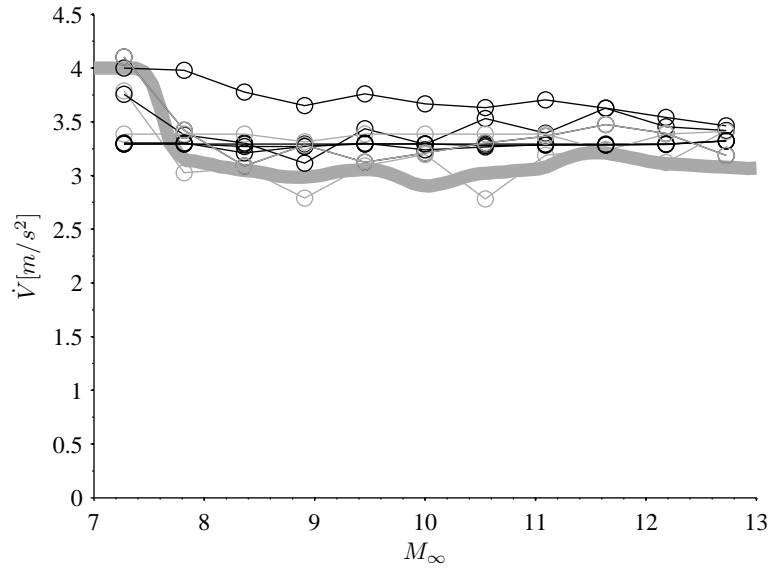
(b) Optimized accelerations.

Figure 5.9: Initial guesses (5.9(a)) and final optimized results (5.9(b)) for cases 1-10 for the collocation optimization method. The thick line represents the trajectory as optimized by the surrogate method. For each of the cases, the fuel required (cost) is listed in Table 4.6

ation (as shown in Fig. 5.9(a)) were able to achieve results superior to the baseline result. Also, note that due to the large truncation error mentioned in section 4.3, trajectories with differing accelerations are reported to have the same cost. This optimization serves to indicate the range of trajectories that result in low fuel con-

97

sumption from $M = 7$ to $M = 13$, rather than a precisely defined single trajectory that represents an absolute minimum. Note that although the surrogate prediction was only a few percent worse in fuel consumption than the trajectory-based optimization, the trajectory-based optimizations arrive at slightly higher accelerations overall.
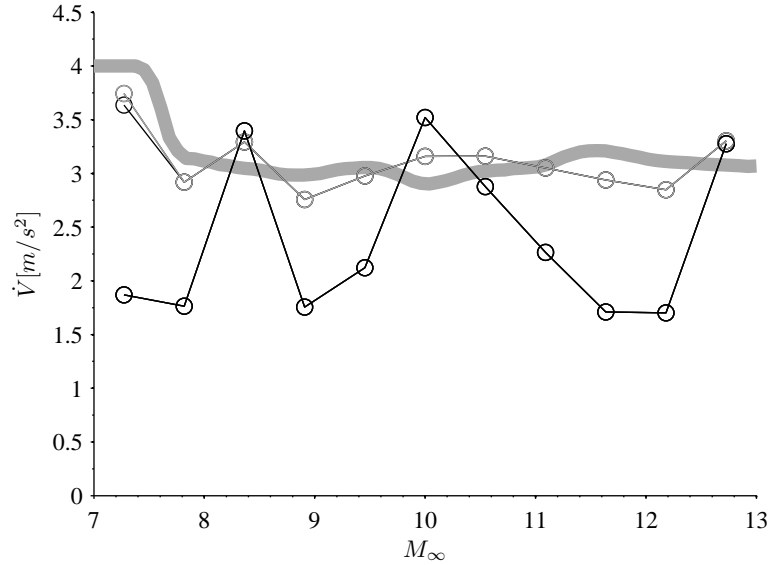
(a) Initial guesses.
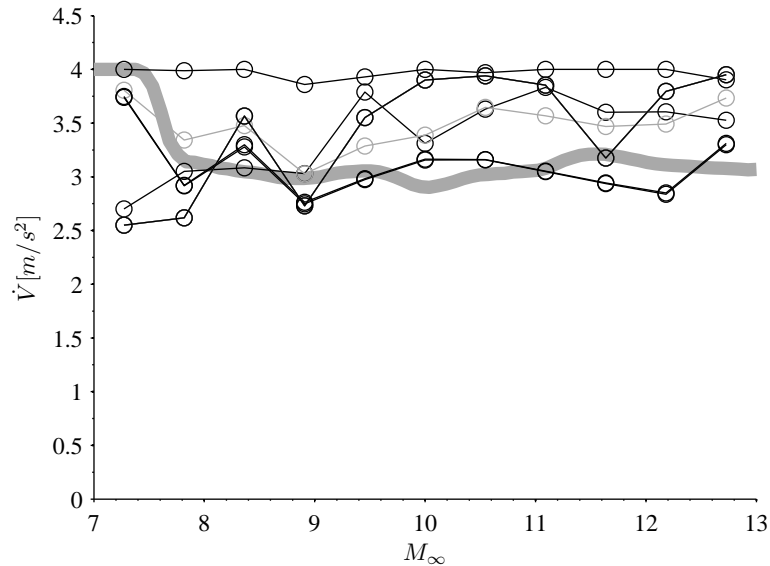
(b) Optimized accelerations.

Figure 5.10: Initial guesses (5.10(a)) and final optimized results (5.10(b)) for cases 11-15 for the collocation optimization method. The thick line represents the trajectory as optimized by the surrogate method. For each of the cases, the fuel required (cost) is listed in Table 4.6

Figure 5.10 shows the resulting accelerations of the collocation trajectory cases that had more fuel consumed than the baseline (surrogate) optimization. Note that some of these cases began at a randomized initial condition that differs appreciably from the baseline. However, the optimizer was able to reduce the fuel cost significantly by increasing the average acceleration in all cases. The drawback to beginning with a poor initial condition is clearly evident; the resulting minimum is not as small as the fuel consumption in the other cases, and the trajectories vary more between cases, as well as the acceleration between adjacent nodes.

As can be seen from Table 4.6, some of the conditions resulted in trajectories with astronomical costs (because they had legs with very small acceleration adjacent to legs with very large acceleration). These would only obscure the good results plotted in Fig. 5.9 and 5.10, and are omitted.

Figs. 5.9 and 5.10 show the differences between the collocation and the surrogate method of optimization. The main result indicated in Fig. 5.9 is that the collocation method can arrive at a result that is as good as or better than the result from the surrogate method if a reasonable initial guess and good step size limits are provided. These cases all have small differences in acceleration between adjacent trajectory legs (a desirable quality), and almost all legs have acceleration greater than the surrogate computes for the same Mach numbers. Although the variability between runs makes it difficult to select a single trajectory for minimum cost, it would perhaps be reasonable to throw out the top and bottom outliers and define a range of acceptable accelerations for each Mach number based on the remaining results. In general, an acceleration near that predicted by the surrogate, but about 10% larger, is preferred. Note that 4m/s^2 was the upper bound in both the surrogate and the collocation optimization methods.

Fig. 5.10 indicates that with good limits on step sizes it is collocation optimization to reach a reasonable solution, but that if the initial guess is poor, it is unlikely to be as good as the surrogate optimization. This is shown by the fact that although runs 13 and 14 began with a randomized set of initial accelerations, they were able to achieve results within 1% and 4% (respectively) of the surrogate. Beginning from the lower limit on acceleration (0.1m/s^2) with proper step size limits, as in run 15 gives a result only 8% worse than the baseline. Although these differences from the baseline result are substantial, the initial conditions result in costs in the range of those from runs 16 to 23 (3500 kg to 18570 kg), so the final condition for these runs still represents a very substantial improvement, in spite of the poor initial guesses.

The final result of the trajectory optimization study was that the collocation

method was successful in optimizing a trajectory with a realistic vehicle analysis code that has accuracy limitations. The drawback to using the collocation approach without a surrogate model is that it is difficult not to have the optimizer get "stuck" in a local minimum. This drawback is mitigated by initializing the collocation optimization with the final result from the surrogate optimization, and by selecting appropriate step sizes in the optimization to ignore the truncation error of the model.

CHAPTER 6

Summary and Conclusions

In this dissertation research, the goal of achieving successful hypersonic vehicle design inspires two basic contributions. First, I created the MASIV propulsion code and combined with the inlet, nozzle, and vehicle trim codes from MASTrim (developed principally by my teammate Dalle). The MASIV/**MASTrim!** (**MASTrim!**) code analyzes the performance of generic hypersonic airplanes to a level of accuracy that is acceptable for initial design, optimization, and control studies. This code has many applications, including some that I have shown here: fundamental examinations of high-speed combustion and choking phenomena in dual-mode ramjet/scramjet engines, and prediction of vehicle performance at a variety of different conditions, which facilitates trajectory-based design.

The MASIV model employs 6 empirical constants that were taken directly from jet in crossflow mixing experiments. It also assumes 1-D heat addition to a flow from 3-D jet in crossflow combustion. It includes an empirical skin friction coefficient. The flameout is modeled by modern turbulent combustion scalar dissipation theory. It contains a quasi 1-D model of the shock train in the isolator, with 1 experimental constant taken from shock train experiments.

While MASIV requires only a few seconds of run time on a modern personal computer to compute values of thrust and moments that agree with high-fidelity CFD results, it has several limitations. Currently it is limited to 2-D steady (i.e., time-averaged) conditions. Fuel must be injected as a jet that is perpendicular to a cross flow of air. Our current implementation is limited to H_2 fuel at one pressure and temperature for flamelet chemistry and ethylene (C_2H_4) or methane (CH_4) chemistry for premixed finite-rate chemistry. These limitations can easily be avoided in the future by creating additional flamelet lookup tables for different fuels, and different reaction pressures and temperatures. To consider different injection angles, we would need experimentally verified scaling relations for jets injected at arbitrary angles into crossflows. Previously we have computed the sensitivity of the thrust to the vehicle

angle of attack, as well as the poles and zeros of the transfer functions that relate control inputs of fuel setting, elevator and canard to 2-D airplane stability [29, 31].

A method has also been presented for solving steady-state reacting internal flow problems through a singularity in Mach number without time-stepping. The principal advantage of this method is that it converges in about 5 to 30 steps, whereas time-stepping an unsteady set of partial differential equations to steady state can require many more iterations. Validation was performed by comparing computations to results from an experimental, laboratory-scale combustor. Agreement was good, in general. We conclude that most of the behavior of the device can be captured using a one-dimensional approximation and that engineering performance metrics, such as pressure evolution and location of thermal choking point, can be predicted by such a model. Effects which are two- or three-dimensional in nature cannot be predicted by this model, as some of the comparisons indicated. However, agreement in pressure evolution suggests that the model can be used to predict thrust, and agreement in choking location suggests that the model can be used to predict whether the engine will operate in ram mode or in scram mode.

The second major contribution of this thesis is to show how trajectory-based collocation optimization can be applied to a vehicle whose performance is not yet well-understood due to lack of functioning prototypes. This method worked well enough to derive basic principles about the trajectories hypersonic airplanes may fly, but its accuracy was limited due to the many approximations made in the development of the vehicle models, including trajectory simulation.

6.1   Conclusions

The MASIV control-oriented propulsion code was found to agree with experimental heat release distribution measurements with an accuracy comparable to that of the Fluent CFD code. Based on pressure values (the only variable that can be quantitatively compared for all 3 results) Fluent gives a Root-Mean-Square deviation of 25% from the experimentally measured pressures. MASIV gives an RMS deviation of 18% from the experimentally measured pressures although it should be noted that the good agreement between MASIV and experiment in the diverging section is probably due to fortuitous choice of conditions and the effects of a simplified mixing model and heat loss to walls, which tend to cancel each other out. The MASIV code overpredicts the amount of reaction near injectors. This result is acceptable for control evaluation and MDO-type applications because the overall behavior of the code is correct, even

though there are some errors due to the simplified mixing model. A typical MASIV run requires ~ 1s of run time on a dual-core 32-bit computer.

The model was shown to provide a method that predicts whether the vehicle operates in ram mode or scram mode. Comparisons cannot be made between predicted and measured thrust because the test section of the experiment is not installed on a thrust stand. Other experiments have thrust information, but lack detailed pressure profiles as a function of equivalence ratio.

It was shown that the model can be used to predict vehicle performance for conditions which cannot at present be tested experimentally. The model predicts that ram-mode operation will generate more thrust than scram mode under certain conditions (low M, high angle-of-attack), although this is not necessarily a general result. It also predicts that the thrust produced will undergo a discrete change when a mode change occurs, which agrees with the discrete change in pressure profile observed experimentally. The derivative of thrust with respect to Mach number, dF/dM is also different on different sides of the transition point. This combination of factors indicates a potential problem area for vehicle control, as successful control strategies must either avoid mode transition at an inconvenient flight condition or handle the discrete change in thrust and derivatives of thrust that occur across a transition event.

Two optimizations were performed using the MASIV and MASTrim low-order models [22, 37]. First the design of a dual-mode ramjet/scramjet engine flowpath was optimized for a short, fixed trajectory at constant dynamic pressure, to determine which parameters of the combustor are significant for overall thrust and fuel consumption. Second, the trajectory the vehicle was intended to follow was optimized, again at constant dynamic pressure, for a fixed vehicle. By modifying the combustor geoemetry, a flowpath was found that was able to generate sufficient thrust to trim a vehicle along a scram-mode-only, constant-dynamic-pressure trajectory from $M = 7$ to $M = 13$. Minimum fuel optimal trajectories for the given vehicle were shown.

The mode prediction capabilities and trajectory-based optimization including trim make MASIV/MASTrim a significant improvement over the codes mentioned previously in section 1.2. These approaches either used very simple analysis to find optimal trajectories, or used simple trajectory analysis (or single point analysis) to examine optimal vehicle performance. The method introduced here uses analysis that shows favorable comparison to real experimental data, but is sufficiently fast (in computation time) to be used in a contemporary optimal control method. Overall, this means that MASIV/MASTrim is a candidate for initial vehicle design studies, because the results it provides are likely to be compatible with high-fidelity studies that

are typically done only once design decisions have already been made.

6.2   Design principles

This section lists some useful design principles that were learned in the effort to select a flowpath geometry and a trajectory that would allow the MAX-1 vehicle to be trimmed and to fly with minimum fuel consumption. These methods can be described as design space exploration methods, since it is very difficult in practice to claim that a given result is truly optimal in a discrete simulation based on nonlinear equations. This is a direct consequence of the discussion of truncation error in section 4.

6.2.1   Dual-mode combustor stability

The combustor must operate in steady state in both ram and scram modes to have reasonable performance. The performance of the combustor can only realistically be guaranteed if a choking/transition point is preselected and carefully designed into the geometry. I conclude that successful ramjet combustor designs should focus on 3 metrics:

1. Adequate stability margin must be achieved over the operating range. Stability margin being calculated for varying operating conditions, inlet performance and thrust requirements (hence, equivalence ratio). This must be verified by trajectory analysis, but it is clear that stability is a function of nearness to the choking boundary, which can be detected using the methods presented here. This is a critical operating limit whether in ram mode or in scram mode.

2. Adequate unstart margin must be achieved over the range of conditions. Similarly, this can be determined by the methods presented here. Unstart margin is proportional to the distance between the front of the isolator and the front of the pre-combustion shock train.

3. Proper fuel injector positioning is important. The earlier analysis (section 5.2) shows that there is an optimal injector position in the combustor such that the flame is mostly contained within the confined (constant-area) section for scram-mode operation. For ram mode, there must be large enough heat release in the diverging section to achieve stability of the location of the thermal choking point. The largest heat release must overlap with the beginning of the divergence or it will be difficult to add enough fuel to produce sufficient thrust to trim the

vehicle. This also suggests 2 injector locations. If it is deemed impossible to have 2 sets of injectors, trajectory-based optimization should be used to place the injectors properly to have adequate performance in both ram-mode and scram-mode operation.

6.2.2   Operating point smoothness

The operating maps (such as Fig. 5.8) must be sufficiently smooth. It is useful to consider the design space of the vehicle with a tool that can profile performance across a wide range of conditions. In this way, rapid losses of performance at off-design conditions, which have been responsible for crashes of the X-43 and X-51 experimental vehicles, can potentially be mitigated.

6.2.3   Trajectory generation

1. The model and trajectory simulation scheme were capable of simulating trajectories within about 3-5 minutes of run time per trajectory. This is basically dependent on the longest (worst case) simulation times for each of the trim conditions. There are 2 sets of trim conditions that need to be run for each trajectory. Since all the trim cases are run in parallel, this part only takes as long as the longest trim [77]. Trim might typically take 15-25 function evaluations, at 3-5 seconds apiece on a $2 - 3.4\,\mathrm{GHz}$ processor. This gives $25 \times 5 \times 2 = 250\mathrm{s}$ as a worst-case time estimate for each trajectory.

2. This method can be extended to trajectories comprising arbitrarily many nodes without taking any longer, as long as 1 processor per trim problem is allotted.

3. The collocation method was satisfactory for trajectory optimization. However, the truncation error from all sources limited the accuracy of the optimization. Reasonable initial conditions and step size limits for finite differencing are required for good performance in the optimization.

4. Results showed that high acceleration trajectories lead to minimum fuel consumption for this type of scramjet. This is because time spent in the air can be kept to a minimum for accelerating trajectories by accelerating as fast as possible. The scramjet has similarities to a rocket except that the scramjet can be oxidizer-limited. Once all the oxygen in the air is used, no larger acceleration is possible, which sets an upper bound on the acceleration. Unlike other airplanes

in which increasing drag sets the upper limit on speed, with this vehicle and mission we found that to minimize fuel consumption flight duration should be kept short.

5. A gradient-based optimizer was chosen and was found to work adequately for this problem in general. The hybrid approach was found to be the most robust method. It uses the surrogate method to generate an improved initial guess for the collocation method. This finding has been previously remarked upon by Conway [87].

6.3   Future Work

There are several ways in which this research could be expanded upon in the future. The most obvious extension would be to include the design of the ram-mode portion of the trajectory in the analysis, and then to incorporate the transition between ram-mode and scram mode. This can be done using the approach used above, but simulation times will necessarily be on the order of $10\times$ longer than the scram-only trajectories considered so far. I expect that the simulations may take even longer than that, since we have already discovered that the vehicle (as designed right now) has more difficulty coming to trim in the ram mode than in the scram mode. A ram trajectory could indeed be designed, but computation times will probably be about $20\times$ that of the scram-only trajectory.

One possible way to improve the simulation time is to increase the fidelity with which the trajectories are simulated. The easiest way to do this is to implement the Runge-Kutta based method of Enright and Conway [75]. If the trajectory simulation itself is responsible for the jitter observed in the trajectory optimization, it is possible that this increase in accuracy will make those results much better as well. This method also has the advantage of being extensible to even more processors than the Hermite-Simpson method used here, and it may require fewer decision variables to define the trajectory.

Finally, I propose a research task, which is to define a metric for design quality that improves upon trajectory-based design, which is already a major improvement over multi-point or single-point design methods. My initial work in this area leads me to believe that path-planning methods can be used to find initial guesses for trajectories, and that nonlinear control theory can be used to predict the size of deviations the overall system can tolerate before it fails. Thus, I see the work presented here as

potentially being a major part of an automatic design method that would first define initial guesses (a function here served by Dalle's work the a surrogate model), optimize the initial guess until a reasonable trajectory is achieved (using the method I present here), and then determine the range over which that vehicle and trajectory are likely to be valid (using nonlinear control methods). I believe this early-stage systems level approach to design of highly-integrated vehicles, including the hypersonic airplane presented here, has a good chance of reducing the risk of vehicle loss that has been demonstrated in 2 out of 5 total hypersonic airplane tests so far.

APPENDIX A

Derivation of 1-D conservation equations

The conservation equations for a 1-D flow in a variable area duct have been derived many times in the literature.[15, 34] We present here some points which require attention in order to calculate the effect of heat release and wall friction, as well as compute the Mach number of a reacting flow.

Figure A.1 shows the canonical geometry of a duct control volume differential element. Φ in the figure represents a state vartable of interest. The possible modes for addition of mass, momentum and energy are represented by arrows entering and leaving the control volume.

A.1   Speed of Sound

The two limits on sound speed are frozen and equilibrium. Beginning from Law's result[63] we obtain the following frozen sound speed equation:

$$a^2 = RT \frac{\sum_i Y_i c_{p,i}}{\sum_i Y_i c_{p,i} - R} \tag{A.1}$$

This is identical to the sound speed that can be found using the mass-weighted average c_p and the mixture R. These in turn are found by the NASA CEA coefficients method as described above.

Here, the definition of c_p corresponds to the frozen flow case. We have found that using the frozen flow c_p gives good results for prediction of the sonic point due to thermal choking, although it is unclear how much error is incurred by neglecting the effect of reaction at points other than the sonic point. The sonic point predicted using this method corresponds to within computer precision to the point at which the equations become extremely stiff, so it is useful for this purpose. Most likely this is because any reaction rate effects due to finite-rate reactions will have derivatives

108
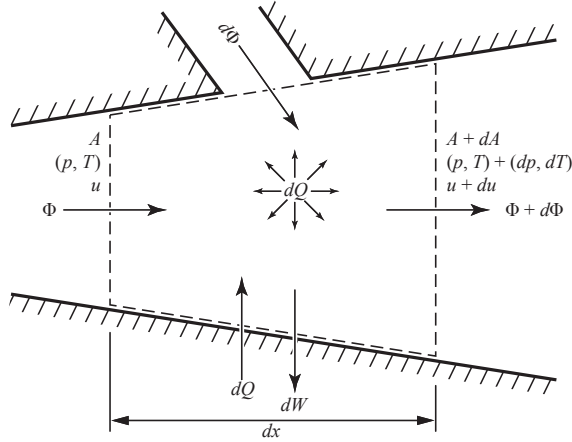
Figure A.1: Differential Element for 1-dimensional Fluid Flow. Φ is the flux of any quantity across the open system boundaries.

that are small compared to the large derivatives of the state quantities near the sonic point. The specific heat c_p of the mixture is not required for any other purpose, so the frozen flow approximation is sufficient for the needs of the proposed algorithm.

A.2   Molecular Weight

$$\frac{1}{W} = \sum_i \frac{Y_i}{W_i} \tag{A.2}$$

$$\frac{dW}{dx} = -W^2 \sum_i \left(\frac{1}{W_i} \frac{dY_i}{dx} \right) \tag{A.3}$$

A.3   Evolution of Species

We write a general form equation for the evolution of species allowing both creation of species in the volume due to reaction and addition of species through walls. This equation must be consistent with conservation of atoms, but Eq. A.5 does not guarantee this so the reaction rates ($\dot{\omega}_i$) must themselves conserve atoms. Equation A.5 is consistent with conservation of mass and indeed the mass of each species is conserved when reactions which generate or consume species are considered.

$$\frac{\partial}{\partial t} \iiint_V Y_i \rho dV + \iint_S Y_i \rho \mathbf{u} \cdot \mathbf{n} dS = \int_{\delta x} \dot{\omega} A dx + \dot{m}_i \tag{A.4}$$

$$\frac{dY_i}{dx} = \frac{\dot{\omega}}{\rho u} + \frac{1}{\dot{m}}\frac{d\dot{m}_i}{dx} - \frac{Y_i}{\dot{m}}\frac{d\dot{m}}{dx} \tag{A.5}$$

A.4 Conservation of Momentum

We begin with the control volume form of the momentum conservation equation. Considering only steady solutions and neglecting body forces, and allowing momentum addition through the walls (assuming the added mass brings some momentum along with it). This results in the momentum equation, equation A.7.

With the assumption that the wall friction is based on a constant coefficient of friction C_f, the wall shear stress can be represented as

$$\tau_w \equiv C_f \rho u^2 / 2 \tag{A.6}$$

The final momentum equation is then

$$\frac{1}{u}\frac{du}{dx} = -\frac{1}{\rho u^2}\frac{dp}{dx} - \frac{C_f}{2A}\frac{dS_w}{dx} - \frac{(1-\varepsilon)}{\dot{m}}\frac{d\dot{m}}{dx} \tag{A.7}$$

Here, ε is the ratio of the axial velocity of the added mass to the axial velocity of the free stream.

One basic approximation for the wetted area (S_w) is to consider square cross sections

$$dS_w = \sqrt{16A + \left(\frac{dA}{dx}\right)^2} \tag{A.8}$$

For anything more complex than that, it is best to simply record the wetted area at each point and to use it as a parameter, as with cross-sectional area or mass addition.

A.5 Conservation of Energy

Total enthalpy of a gas mixture is the sum of the component enthalpies and the square of the velocity, assuming that all species have the same velocity:

$$h_0 = \sum_i \left[h_i^0 + \int_{T_{ref}}^T c_{p,i}(\tau)d\tau \right] Y_i + \frac{u^2}{2} \tag{A.9}$$

$$\frac{dh_0}{dx} = u\frac{du}{dx} + \sum_i \left[c_{p,i}Y_i\frac{dT}{dx} + h_i\frac{dY_i}{dx} \right] \tag{A.10}$$

$$\frac{1}{h_0}\frac{dh_0}{dx} = -\frac{1}{\dot{m}}\frac{d\dot{m}}{dx} + \frac{1}{h_0\dot{m}}\frac{d\dot{Q}}{dx} + \frac{1}{h_0\dot{m}}\frac{d\dot{W}}{dx} + \frac{1}{h_0\dot{m}}\sum_i h_i\frac{d\dot{m}_i}{dx} \tag{A.11}$$

$$\frac{1}{h_0}\left[u\frac{du}{dx} + \frac{dT}{dx}\sum_i c_{p,i}Y_i + \sum_i h_i\frac{dY_i}{dx} \right]$$
$$= -\frac{1}{\dot{m}}\frac{d\dot{m}}{dx} + \frac{1}{h_0\dot{m}}\frac{d\dot{Q}}{dx} + \frac{1}{h_0\dot{m}}\frac{d\dot{W}}{dx} + \frac{1}{h_0\dot{m}}\sum_i h_i\frac{d\dot{m}_i}{dx} \tag{A.12}$$

We assume that heat addition per unit area is uniform and constant in the duct.

$$\dot{Q} = \dot{Q}'' P_w dx \tag{A.13}$$

$$\dot{Q} = \dot{Q}'' S_w \tag{A.14}$$

$$d\dot{Q} = \dot{Q}'' dS_w \tag{A.15}$$

And if we suppose that the heat transfer is uniform and make use of the Reynolds Analogy, assuming that c_p of the gas mixture is uniform in each cross section,

$$C_H = \frac{\dot{Q}''}{\rho u(h_{aw} - h_w)} \tag{A.16}$$

$$C_H = \frac{C_f}{2Pr^{2/3}} \tag{A.17}$$

$$\frac{d\dot{Q}}{dx} = \frac{\rho u C_f(h_{aw} - h_w)}{2Pr^{2/3}}\frac{dS_w}{dx} \tag{A.18}$$

The required enthalpies can be computed by the approximations

$$h_{aw} = h + Pr\frac{u^2}{2} \tag{A.19}$$

$$h_w = h(T_w) \tag{A.20}$$

$$\tag{A.21}$$

After some rearrangement to solve for the derivative of temperature, we obtain

$$
\begin{aligned}
\frac{1}{h_0}\frac{dT}{dx}\sum_i c_{p,i}Y_i = &-\frac{u}{h_0}\frac{du}{dx} - \frac{1}{\dot{m}}\frac{d\dot{m}}{dx} \\
&+ \frac{1}{h_0\dot{m}}\frac{\rho u C_f(h_{aw}-h_w)}{2Pr^{2/3}}\frac{dS_w}{dx} \\
&+ \frac{1}{h_0\dot{m}}\frac{\rho u^3 C_f}{2}\frac{dS_w}{dx} \\
&- \frac{1}{h_0}\sum_i h_i\frac{dY_i}{dx} + \frac{1}{h_0\dot{m}}\sum_i h_i\frac{d\dot{m}_i}{dx}
\end{aligned}
\tag{A.22}
$$

Note that the rate of change of wall area, $\frac{dS_w}{dx}$ can be computed using equation A.8 or some other method.

A.6 Ratio of Specific Heats

Although it does not appear in the above equations, sometimes the ratio of specific heats is desired. Since R and $\hat{c}_p$ can be computed using quantities known at the time of solution via Eq. A.2, this results in a value of γ that can be computed after the simulation is complete. Or, defining $\hat{c}_p = \sum_i Y_i c_{p,i}$, we can make an approximation for γ.

$$\gamma = \frac{c_p}{c_p - R} \tag{A.23}$$

This is notable simply because it allows the ratio of specific heats to be computed as a function of the local state of the gas. A simpler approach will not give an accurate number because of the variation of c_p with x.

APPENDIX B

List of Parameters for the MAX1

Table B.1: Parameters used to define the MAX-1 vehicle

Name	Code name	Design value
Design Mach number range	M_inf	$\begin{bmatrix} 7 & 9 \end{bmatrix}$
Angle of attack	aoa	0
Number of external inlet ramps	n_ext	2
Number of cowl ramps	n_int	2
Inlet scaling length	L_scale	12m
Overall pressure ratio	r_p	40
Max. forward cowl deflection	u1_max	0
Max. downward cowl deflection	u2_max	0
Max. downward cowl rotation	u3_max	0
Isolator length to height ratio	AR_isolator	6
Isolator front height	H_isolator_fore	0.219
Flowpath design width	width	1
Combustor front height	H_combustor_fore	0.219
Number of fuel injectors per width	n_inj	9

---

*Relative to bottom front edge of combustor
†Relative to center of volume

Table B.2: Parameters used to define the MAX-1 vehicle (continued)

Name	Code name	Design value
Fuel injector axial position*	injector_locations	0.219m
Fuel injector vertical location*	injector_locations	0.219m
Fuel injector diameter	injector_diameter	0.0539m
Altitude	altitude	26km
Equivalence ratio	ER	0.5
Combustor wall divergence locations*	divergence_locations	1.393m
Combustor wall divergence angles	divergence_angles	0.0537
Combustor wall temperature	T_w	1350K
Combustor friction coefficient	C_f	0.003
Combustor wall heating switch	heating	true
Combustor wall friction switch	friction	true
Combustor rear height	H_combustor_aft	0.270m
Combustor length	L_combustor	2.348m
Inlet forebody shape	scaled_body	[7x2 double]
Inlet cowl shape	scaled_cowl	[4x2 double]
Nozzle front height	H_nozzle_fore	0.270m
Nozzle length	L_nozzle_body	12m
Nozzle rear height	H_nozzle_aft	2.348m
Cowl height	H_cowl	0.12m
Cowl length after combustor	L_nozzle_cowl	1.5m
Vehicle width at nose	nose_width	4.286m
Width of engine cowl	cowl_width	2.143m
Width of vehicle at middle	waist_width	6m
x-position of waist	waist_x	14.823m
Angle of top vehicle panel	upper_body_angle	0.05
Width of vehicle at tail	tail_width	4.714m
Height of tail above nose	tail_height	0.429m
Length of middle of vehicle	mid_length	6.097m
Ext. panel maximum side length	triangle_resolution	0.915m

114

Table B.3: Parameters used to define the MAX-1 vehicle (continued)

Elevator centerline (CL) axial location	elevator_x_root	0.85×vehicle length
Elevator CL spanwise location	elevator_z_root	0.7×vehicle width
Elevator chord length	elevator_chord	0.2×vehicle length
Elevator sweep angle	elevator_sweep	0.6
Elevator taper ratio	elevator_taper_ratio	0.6
Elevator thickness to chord ratio	elevator_thickness	0.08
Elevator fraction that moves	elevator_fraction	1
Elevator span to chord ratio	elevator_aspect_ratio	1.5
Elevator dihedral angle	elevator_dihedral	0.05
Elevator span length	elevator_span	0.24×vehicle length
Rudder CL axial location	rudder_x_root	0.85×vehicle length
Rudder vertical location	rudder_y_root	0.9×vehicle height
Rudder chord length	rudder_chord	0.2×vehicle length
Rudder sweep angle	rudder_sweep	0.6
Rudder taper ratio	rudder_taper_ratio	0.7
Rudder thickness to chord ratio	rudder_thickness	0.08
Rudder fraction that moves	rudder_fraction	0.3
Rudder span to chord ratio	rudder_aspect_ratio	1.1
Rudder dihedral angle	rudder_dihedral	0.15
Rudder span length	rudder_span	0.187×vehicle length
Empty mass	mass_empty	1.594×10^4 kg
Fuel mass (maximum)	mass_fuel	2.386×10^4 kg
Payload mass	mass_payload	3.984×10^3 kg
Fraction of fuel mass filled	fuel_fraction	0.5
Center of mass axial location[†]	cg_shift_x	−0.1×vehicle length
Center of mass vertical location[†]	cg_shift_z	0
Center of volume location	center_of_mass	[3x1 double]

BIBLIOGRAPHY

[1] USAF, (public domain).

[2] NASA, NASA Photo ED99-43243-01.

[3] Boeing.

[4] Dalle, D. J., Torrez, S. M., Driscoll, J. F., Bolender, M. A., and Bowcutt, K. G., "Minimum-Fuel Hypersonic Ascent along a Constant-Dynamic Pressure Trajectory," *Journal of Spacecraft and Rockets*, 2012, To be submitted.

[5] Heiser, W. H. and Pratt, D. T., *Hypersonic Airbreathing Propulsion*, AIAA Pub., Washington, DC, 1994.

[6] Waldman, B. and Harsha, P., "NASP: Focus on Technology," *AIAA Fourth International Aerospace Planes Conference*, Vol. December, 1992.

[7] Romankov, O. N. and Starostin, F. I., "Design and Investigation of the Stand and Flying Scramjet Models Conceptions and Results of Experiments," June 1993, AIAA Paper 93-2447.

[8] Kuczera, H. and Sacher, P., "The German Hypersonics Programme - Status Report 1991," *AIAA Third International Aerospace Planes Conference*, December 1991, AIAA 1991-5001.

[9] Ferlemann, P. G., "Comparison of Hyper-X Mach 10 Scramjet Preflight Predictions and Flight Data," *AIAA/CIRA 13th International Space Planes and Hypersonics Systems and Technologies*, 2005, AIAA 2005-3352.

[10] Hank, J. M., Murphy, J. S., and Mutzman, R. C., "The X-51A Scramjet Engine Flight Demonstration Program," *15th AIAA International Space Planes and Hypersonic Systems and Technologies Conference*, 2008, AIAA Paper 2008-2540.

[11] Jackson, K. R., Gruber, M. R., and Barhorst, T. F., "The HIFiRE Flight 2 Experiment: An Overview and Status Update," *45th AIAA/ASME/SAE/ASEE Joint Propulsion Conference & Exhibit*, August 2009, AIAA 2009-5029.

[12] Richmond L. Miller, J., "Flight Testing the F-12 Series Aircraft," *Journal of Aircraft*, Vol. 12, No. 9, September 1975, pp. 695–698.

[13] Bowcutt, K., "Hypersonic Aircraft Optimization Including Aerodynamic, Propulsion, and Trim Effects," *AIAA Fourth International Aerospace Planes Conference*, December 1992.

[14] O'Neill, M. K. L. and Lewis, M. J., "Design Tradeoffs on Scramjet Engine Integrated Hypersonic Waverider Vehicles," *Journal of Aircraft*, Vol. 30, 1993, AIAA 46438-956.

[15] Shapiro, A. H., *Dynamics and Thermodynamics of Compressible Fluid Flow*, Ronald Press, NY, 1953.

[16] Bowcutt, K. G., "Multidisciplinary Optimization of Airbreathing Hypersonic Vehicles," *Journal of Propulsion and Power*, Vol. 17, 2001, pp. 1184–1190.

[17] Nelder, J. A. and Mead, R., "A Simplex Method for Function Minimization," *The Computer Journal*, Vol. 7, No. 4, 1965, pp. 308–313.

[18] Hargraves, C. R. and Paris, S. W., "Direct Trajectory Optimization Using Nonlinear Programming and Collocation," *Journal of Guidance*, Vol. 10, No. 4, July-August 1987, pp. 338–342, AIAA-20223-706.

[19] Koko, F., *Aerostructural and Trajectory Optimization of Morphing Wingtip Devices*, Master's thesis, Delft University of Technology, October 2011.

[20] Kim, B., Fleming, G., Balasubramanian, S., Malwitz, A., Lee, J., Ruggiero, J., Waitz, I., Klima, K., Stouffer, V., Long, D., Kostiuk, P., Locke, M., Holsclaw, C., Morales, A., McQueen, E., and Gillette, W., "System for assessing Aviation's Global Emissions (SAGE), Version 1.5, Technical Manual," Tech. Rep. DOT-VNTSC-FAA-05-14, FAA-EE-2005-01, U. S. Department of Transportation, Massachusetts Institute of Technology, Logistics Management Institute, Federal Aviation Administration, Office of Environment and Energy, 800 Independence Ave., S. W., Washington, DC 20591, September 2005.

[21] Peters, D. L., *Coupling and Controllability in Optimal Design and Control*, Ph.D. thesis, University of Michigan, 2010.

[22] Torrez, S. M., Driscoll, J. F., Ihme, M., and Fotia, M. L., "Reduced Order Modeling of Turbulent Reacting Flows With Application to Scramjets," *Journal of Propulsion and Power*, Vol. 27, No. 2, March-April 2011, pp. 371–382.

[23] Torrez, S. M., Dalle, D. J., and Driscoll, J. F., "A New Method for Computing Performance of Choked Reacting Flows and Ram-to-Scram Transition," *Journal of Propulsion and Power*, 2011.

[24] Bolender, M. A. and Doman, D. B., "Nonlinear Longitudinal Dynamical Model of an Air-Breathing Hypersonic Vehicle," *Journal of Spacecraft and Rockets*, Vol. 44, No. 2, 2007, pp. 374–387.

[25] Chavez, F. R. and Schmidt, D. K., "Analytical Aeropropulsive/Aeroelastic Hypersonic-Vehicle Model with Dynamic Analysis," *Journal of Guidance, Control, and Dynamics*, Vol. 17, No. 6, 1994, pp. 1308–1319.

[26] Tarpley, C. and Lewis, M. J., "Stability Derivatives for a Hypersonic Caret-Wing Waverider," *Journal of Aircraft*, Vol. 32, No. 4, 1995, pp. 795–803.

[27] Dalle, D. J., Fotia, M. L., and Driscoll, J. F., "Reduced-Order Modeling of Two-Dimensional Supersonic Flows with Applications to Scramjet Inlets," *Journal of Propulsion and Power*, Vol. 26, No. 3, 2010, pp. 545–555.

[28] Torrez, S. M., Scholten, N. A., Micka, D. J., Driscoll, J. F., Bolender, M. A., Doman, D. B., and Oppenheimer, M. W., "A Scramjet Engine Model Including Effects of Precombustion Shocks and Dissociation," *44th AIAA/ASME/SAE/ASEE Joint Propulsion Conference & Exhibit*, 2008, AIAA Paper 2008-4619.

[29] Torrez, S. M., Driscoll, J. F., Bolender, M. A., Oppenheimer, M. W., and Doman, D. B., "Effects of Improved Propulsion Modelling on the Flight Dynamics of Hypersonic Vehicles," *AIAA Atmospheric Flight Mechanics Conference and Exhibit*, 2008, AIAA Paper 2008-6386.

[30] Torrez, S. M., Driscoll, J. F., Dalle, D. J., and Micka, D. J., "Scramjet Engine Model MASIV: Role of Mixing, Chemistry and Wave Interaction," *45th AIAA/ASME/SAE/ASEE Joint Propulsion Conference and Exhibit*, 2009, AIAA Paper 2009-4939.

[31] Torrez, S. M., Driscoll, J. F., Dalle, D. J., Bolender, M. A., and Doman, D. B., "Hypersonic Vehicle Thrust Sensitivity to Angle of Attack and Mach Number," *AIAA Atmospheric Flight Mechanics Conference*, 2009, AIAA Paper 2009-6152.

[32] Torrez, S. M., Driscoll, J. F., Dalle, D. J., and Fotia, M. L., "Preliminary Design Methodology for Hypersonic Engine Flowpaths," *16th AIAA/DLR/DGLR International Space Planes and Hypersonic Systems and Technologies Conference*, 2009, AIAA Paper 2009-7289.

[33] Hall, K. C., Thomas, J. P., and Dowell, E. H., "Proper Orthogonal Decomposition Technique for Transonic Unsteady Aerodynamic Flows," *AIAA Journal*, Vol. 38, No. 10, 2000, pp. 1853–1862.

[34] O'Brien, T. F., Starkey, R. P., and Lewis, M. J., "Quasi-One-Dimensional High-Speed Engine Model with Finite-Rate Chemistry," *Journal of Propulsion and Power*, Vol. 17, No. 6, 2001, pp. 1366–1374.

[35] Kuo, K. K., *Principles of Combustion*, John Wiley & Sons, 2nd ed., 2005.

[36] Dalle, D. J., Torrez, S. M., Driscoll, J. F., and Bolender, M. A., "Flight Envelope Calculation of a Hypersonic Vehicle Usinga First Principles-Derived Model,"

17th AIAA International Space Planes and Hypersonic Systems and Technologies Conference, 2011.

[37] Dalle, D. J., Torrez, S. M., and Driscoll, J. F., "A Rapid Analysis Technique for Scramjet and Linear Plug Nozzles," *Journal of Propulsion and Power*, 2012, Submitted.

[38] *U.S. Standard Atmosphere, 1976*, U.S. Government Printing Office, October 1976, NOAA-S/T 76-1562.

[39] Van Driest, E. R., "The Problem of Aerodynamic Heating," *Aeronautical Engineering Review*, Vol. 15, No. 10, 1956, pp. 26–41.

[40] E. F. Hasselbrink, J. and Mungal, M. G., "Transverse jets and jet flames. Part 1. Scaling laws for strong transverse jets," *Journal of Fluid Mechanics*, Vol. 443, 2001, pp. 1–25.

[41] Peters, N., "Laminar Diffusion Flamelet Models in Non-Premixed Turbulent Combustion," *Progress in Energy Combustion Science*, Vol. 10, 1984, pp. 319–339.

[42] Merker, G. P., *Simulating combustion: simulation of combustion and pollutant formation for engine-development*, Springer-Verlag, 2006.

[43] Fluent, "FLUENT 6.3 User's Guide," Tech. rep., Ansys, Inc., 09 2006.

[44] Micka, D. J., Torrez, S. M., and Driscoll, J. F., "Measurements and Modeling of the Heat Release Distribution in a Dual-mode Scramjet Combustor with Wall Fuel Injection," *Proceedings of the 6th U.S. National Combustion Meeting*, 2009.

[45] Fotia, M. L. and Driscoll, J. F., "Isolator-Combustor Interactions in a Direct-Connect Ramjet-Scramjet Experiment," *Journal of Propulsion and Power*, 2011, Submitted.

[46] Fotia, M. L., *Experimental Study of Shock-Train/Combustion Coupling and Flame Dynamics in a Heated Supersonic Flow*, Ph.D. thesis, University of Michigan, 2012.

[47] Ihme, M. and See, Y. C., "LES Flamelet Modeling of a Three-Stream MILD Combustor: Analysis of Flame Sensitivity to Scalar Inflow Conditions," *Proceedings of the Combustion Institute*, Vol. 33, 2010.

[48] Ihme, M. and Pitsch, H., "Modeling of Radiation and NO Formation in Turbulent Non-premixed Flames Using a Flamelet/Progress Variable Formulation," *Modeling of Radiation and NO Formation in Turbulent Non-premixed Flames Using a Flamelet/Progress Variable Formulation*, Vol. 20, 2008, pp. 055110.

[49] Tetlow, M. R. and Doolan, C., "Comparison of Hydrogen and Hydrocarbon-Fueled Scramjet Engines for Orbital Insertion," *Journal of Spacecraft and Rockets*, Vol. 44, No. 2, 2007, pp. 365–372.

[50] E. F. Hasselbrink, J. and Mungal, M. G., "Transverse jets and jet flames. Part 2. Velocity and OH field Imaging." *Journal of Fluid Mechanics*, Vol. 443, 2001, pp. 27–68.

[51] Lin, K.-C., Ryan, M., Carter, C., Gruber, M., and Raffoul, C., "Raman Scattering Measurements of Gaseous Ethylene Jets in Mach 2 Supersonic Crossflow," *Journal of Propulsion and Power*, Vol. 26, No. 3, 2010, pp. 503–513.

[52] Billig, F. S., Corda, S., and Pandolfini, P. P., "Design Techniques for Dual Mode Ram-Scramjet Combustors," *7th National Aero-Space Plane Technology Symposium*, October 1989.

[53] Pope, S. B., *Turbulent Flows*, Cambridge University Press, 2000.

[54] Smith, S. H. and Mungal, M. G., "Mixing, structure and scaling of the jet in crossflow," *Journal of Fluid Mechanics*, Vol. 357, 1998, pp. 83–122.

[55] Peters, N., "Die Struktur turbulenter Freistrahl-Diffusionsflammen," *Chemie Ingenieur Technik*, Vol. 55, No. 10, 1983, pp. 743–751.

[56] Schlichting, H. and Gersten, K., *Boundary Layer Theory*, Springer-Verlag, 2004.

[57] Williams, F. A., "Descriptions of Nonpremixed Turbulent Combustion," 2006, AIAA Paper 2006-1505.

[58] Peters, N., *Turbulent Combustion*, Cambridge University Press, Cambridge, 2000.

[59] Ihme, M. and See, Y. C., "Prediction of Autoignition in a Lifted Methane/Air Flame Using an Unsteady Flamelet/Progress Variable Model," Vol. 157, 2010, pp. 1850–1862.

[60] Effelsberg, E. and Peters, N., "Scalar dissipation rates in turbulent jets and jet diffusion flames," Vol. 22, 1989, pp. 693–700.

[61] McBride, B. J. and Gordon, S., "Computer program for calculation of complex chemical equilibrium compositions and applications. Part 1: Analysis," Tech. Rep. RP-1311, NASA, 1994.

[62] McBride, B. J. and Gordon, S., "Computer program for calculation of complex chemical equilibrium compositions and applications," Tech. Rep. RP-1311, NASA, 1996.

[63] Law, C. K., *Combustion Physics*, Cambridge University Press, 2006.

[64] Micka, D. J. and Driscoll, J. F., "Combustion characteristics of a dual-mode scramjet combustor with cavity flameholder," *Proceedings of the Combustion Institute*, Vol. 32, 2009, pp. 2397–2404.

[65] Mathur, T., Gruber, M., Jackson, K., Donbar, J., Donaldson, W., Jackson, T., and Billig, F., "Supersonic Combustion Experiments with a Cavity-Based Fuel Injector," *Journal of Propulsion and Power*, Vol. 17, No. 6, November-December 2001.

[66] Ikui, T., Matsuo, K., and Nagai, M., "The Mechanism of Pseudo-Shock Waves," *Bulletin of the JSME*, Vol. 17, No. 108, June 1974, pp. 731–739.

[67] Le, D. B., Goyne, C. P., Krauss, R. H., and McDaniel, J. C., "Experimental Study of a Dual-Mode Scramjet Isolator," *Journal of Propulsion and Power*, Vol. 24, 2008, pp. 1050–1057.

[68] Goyne, C. P., Rodriguez, C. G., Krauss, R. H., McDaniel, J. C., and McClinton, C. R., "Experimental and Numerical Study of a Dual-Mode Scramjet Combustor," *Journal of Propulsion and Power*, Vol. 22, No. 3, May-June 2006, pp. 481–489.

[69] Goyne, C. P., McDaniel, J. C., Quagliaroli, T. M., Krauss, R. H., and Day, S. W., "Dual-Mode Combustion of Hydrogen in a Mach 5, Continuous-Flow Facility," *Journal of Propulsion and Power*, Vol. 17, No. 6, November-December 2001, pp. 1313–1318.

[70] Hedrick, J. K. and Bryson, A. E. J., "Three-Dimensional, Minimum Fuel Turns for a Supersonic Aircraft," *Journal of Aircraft*, Vol. 9, No. 3, 1972, pp. 223–229, AIAA-58961-202.

[71] Bolender, M. A., Oppenheimer, M. W., and Doman, D. B., "Effects of Unsteady and Viscous Aerodynamics on the Dynamics of a Flexible Air-breathing Hypersonic Vehicle," *AIAA Atmospheric Flight Mechanics Conference and Exhibit*, 2007, AIAA Paper 2007-6397.

[72] Bouchez, M., Perillat, V., Avrashkov, V., and Kopchenov, V., "Numerical and experimental scientific investigation of combustion in a translating cowl dual-mode ramjet," 2011, AIAA Paper 2011-2313.

[73] Mathur, T., Streby, G., Gruber, M., Jackson, K., Donbar, J., Donaldson, W., and Jackson, T., "Supersonic Combustion Experiments with a Cavity Based Fuel Injector," 1999, AIAA 99-2102.

[74] Betts, J. T., "Survey of Numerical Methods for Trajectory Optimization," *Journal of Guidance, Control, and Dynamics*, Vol. 21, 1998, pp. 193–207.

[75] Enright, P. J. and Conway, B. A., "Discrete Approximations to Optimal Trajectories Using Direct Transcription and Nonlinear Programming," *Journal of Guidance, Control, and Dynamics*, Vol. 15, No. 4, July-August 1992, pp. 994–1002.

[76] Hirsch, C., *Numerical Computation of Internal and External Flows*, Vol. 1, John Wiley & Sons, 1988.

[77] Betts, J. T. and Huffman, W. P., "Trajectory Optimization on a Parallel Processor," *Journal of Guidance*, Vol. 14, No. 2, March-April 1991, pp. 431–439, AIAA-20656-932.

[78] Dickmanns, E. D. and Well, K. H., "Parametrization of Optimal Control Problems Using Piecewise Polynomial Approximation," *AIAA Mechanics and Control of Flight Conference*, August 1974, AIAA 74-822.

[79] Russell, R. D. and Shampine, L. F., "A Collocation Method for Boundary Value Problems," *Numerical Mathematics*, Vol. 19, 1972, pp. 1–28.

[80] Micka, D. J., *Combustion Stabilization, Structure, and Spreading in a Laboratory Dual-Mode Scramjet Combustor*, Ph.D. thesis, University of Michigan, 2010.

[81] Mitani, T., Tomioka, S., Kanda, T., Chinzei, N., and Kouchi, T., "Scramjet Performance Achieved in Engine Tests From M4 to M8 Flight Conditions," December 2003, AIAA 2003-7009.

[82] Donde, P., Koo, H., and Raman, V., "A Multivariate Quadrature Based Moment Method for Supersonic Combustion Modeling," *49th AIAA Aerospace Sciences Meeting including the New Horizons Forum and Aerospace Exposition*, January 2011, AIAA 2011-322.

[83] Oberkampf, W. L. and Trucano, T. G., "Verification and validation benchmarks," *Nuclear Engineering and Design*, Vol. 238, 2008, pp. 716–743.

[84] "FLUENT Revision 12.0.16 for ANSYS Release Version 12.0.1," 2009.

[85] Hardalupas, Y. and Orain, M., "Local measurements of the time-dependent heat release rate and equivalence ratio using chemiluminescent emmission from a flame," *Combust. Flame*, Vol. 139, 2004, pp. 188–2007.

[86] Kee, R. J., Rupley, F. M., Miller, J. A., Coltrin, M. E., Grcar, J. F., Meeks, E., Moffat, H. K., Lutz, A. E., Dixon-Lewis, G., Smooke, M. D., Warnatz, J., Evans, G. H., Larson, R. S., Mitchell, R. E., Petzold, L. R., Reynolds, W. C., Caracotsios, M., Stewart, W. E., Glarborg, P., Wang, C., McLellan, C. L., Adigun, O., Houf, W. G., Chou, C. P., Miller, S. F., Ho, P., Young, P. D., Young, D. J., Hodgson, D. W., Petrova, M. V., and Puduppakkam, K. V., *CHEMKIN Release 4.1*, Reaction Design, San Diego, CA, 2006.

[87] Conway, B. A., "A Survey of Methods Available for the Numerical Optimization of Continuous Dynamic Systems," *Journal of Optimization Theory and Applications*, Vol. 152, September 2012, pp. 271–306.

[88] Torrez, S. M., Dalle, D. J., and Driscoll, J. F., "Design of Dual-Mode Hypersonic Vehicle Flow Paths Using a Reduced-Order Model," *17th AIAA International Space Planes and Hypersonic Systems and Technologies Conference*, April 2011.